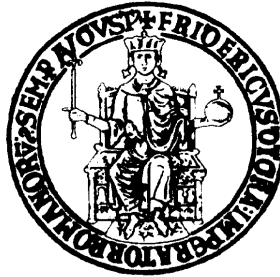


UNIVERSITY OF NAPLES “FEDERICO II”



FACULTY OF ENGINEERING

AEROSPACE ENGINEERING DEPARTMENT

MASTER DEGREE THESIS IN

AEROSPACE AND ASTRONAUTIC ENGINEERING

(CLASS OF THE MASTER DEGREES IN INDUSTRIAL ENGINEERING N.25/S)

**A VORTON WAKE MODEL
FOR PANEL METHODS**

Relators: Ch.mi Prof.

Carlo de NICOLA

Paolo CACCAVALE

Candidate:

Nicola NOLA

Matr. 335/89

ACADEMIC YEAR 2008-2009

alla mia famiglia e a Laura

Contents

Introduction	1
1 PANEL METHODS: A BRIEF HISTORY	3
1.1 Vorton methods: background	8
2 INCOMPRESSIBLE AND INVISCID FLOWS	10
2.1 The domain	11
2.2 The Helmholtz theorem	15
2.2.1 The velocity definition	17
2.3 The scalar potential relationship: Laplace's equation	18
2.4 The vector potential relationship: Poisson's equation	20
2.5 The velocity induced by vorticity: the Biot-Savart law	20
2.5.1 The velocity induced by a straight vortex segment	22
2.6 The vorticity evolution equation	24
2.7 The boundary conditions	26
2.7.1 Infinity boundary conditions	26
2.7.2 Wall boundary conditions	27
2.8 The wing trailing edge Kutta condition	28
2.9 The Unsteady Bernoulli equation	30
2.10 Computation of forces and moments	31
2.10.1 Pressure, force and moment coefficients	33

3	PANEL METHODS	34
3.1	Basic solutions of Laplace equation	34
3.1.1	Quadrilateral source	35
3.1.2	Quadrilateral doublet	38
3.1.3	Constant doublet panel equivalence to vortex ring	41
3.2	Panel method formulation	43
3.2.1	Boundary conditions	47
3.2.2	Singularity model	48
3.2.3	Computation of velocities and forces	51
3.3	Panel method numerical procedure	53
3.3.1	Unsteady panel methods	59
3.3.2	Unsteady panel wake model	60
3.3.3	Computation of velocities and forces	65
 4	 THE VORTON METHOD FOR WAKE	 68
4.1	The vorton method	69
4.2	Conversion of the wake panels to vortons	76
4.3	Summary	80
 5	 PaMS CODE WITH VORTON WAKES	 82
5.1	PaMS code description	82
5.2	Changes in the PaMS code for the introduction of a vorton wake model	84
5.3	Test cases	86
5.3.1	NACA 0012 airfoil	86
5.3.2	NACA 63 mean line	93
5.3.3	Elliptic wing	96
5.3.4	Unsteady pitching airfoil	100
5.4	Vertical-axis wind turbine	103
5.4.1	A single-bladed turbine	103

5.4.2	A three-bladed turbine	109
5.5	Intersection of the wake of a pitching and heaving wing with a down-stream fixed wing	112
5.6	Helicopter rotor in hover	116
	Conclusions	119
	A The solution of Poisson's equation	122
A.1	Derivation of the solution of Poisson's equation	122
	Bibliography	124

List of Figures

1.1	B747 with Space Shuttle Orbiter - lift coefficient [32].	5
2.1	the fluid domain.	11
2.2	the velocity at point P induced by a vortex distribution.	21
2.3	the flow field at the wing trailing edge without (left) and with (right) the imposition of the Kutta condition.	29
3.1	quadrilateral constant-strength source element.	36
3.2	quadrilateral source - uniform velocity vector and isopotential contour.	38
3.3	quadrilateral doublet element.	39
3.4	quadrilateral doublet - uniform velocity vector and isopotential con- tour.	40
3.5	quadrilateral doublet element and its vortex ring equivalent.	42
3.6	the fluid domain considered in the derivation of the Green's Theo- rem BIE.	43
3.7	panel local reference frame for evaluating the normal and tangential velocity components.	52
3.8	examples of discretized (thick and thin) body and wake geometries.	54
3.9	schematization for the influence coefficients.	56
3.10	reference frame for the Kutta condition.	58
3.11	inertial frame and body frame used to describe the motion of the body.	60

3.12 examples of generation of rigid and flexible unsteady wake.	62
3.13 references for the indices of the wake panels.	64
3.14 schematization of the computation of the velocity perturbation components.	66
4.1 vortex tube and its corresponding vorton.	70
4.2 flow field induced by a vorton.	71
4.3 flow field induced by a two-dimensional vortex.	72
4.4 wake model with vortons.	77
4.5 examples of models for the conversion of the near wake panels into vortons.	78
4.6 DIAS vorton wake model - the mechanism of vortex particles generation.	79
4.7 examples of panel wake and vorton wake.	81
5.1 NACA 0012 airfoil - geometry.	87
5.2 wake models.	89
5.3 NACA 0012 airfoil at zero degrees angle of attack - comparison between the vorton wake model to the analytical results and the doublet wake model in terms of pressure distribution.	90
5.4 NACA 0012 airfoil at four degrees angle of attack - comparison between the vorton wake model to the analytical results and the doublet wake model in terms of pressure distribution.	90
5.5 NACA 0012 airfoil at eight degrees angle of attack - comparison between the vorton wake model to the analytical results and the doublet wake model in terms of pressure distribution.	91
5.6 NACA 0012 airfoil at twelve degrees angle of attack - comparison between the vorton wake model to the analytical results and the doublet wake model in terms of pressure distribution.	91

5.7	NACA 0012 airfoil - comparison between the vorton wake model to the analytical results and the doublet wake model in terms of lift characteristics.	92
5.8	NACA 0012 airfoil - the time evolution of the lift coefficient for the DIAS vorton wake.	93
5.9	NACA 63 mean line - geometry.	94
5.10	NACA 63 mean line at 1.6° ideal angle of attack - comparison between the vorton wake model to the doublet model and the analytical results in terms of pressure distribution.	95
5.11	NACA 63 mean line - the time evolution of the lift coefficient.	95
5.12	elliptic wing lift characteristics - comparison between doublet model and vorton wake model with the technique of the Trefftz plane.	99
5.13	elliptic wing drag characteristics - comparison between doublet wake model and vorton wake model with the technique of the Trefftz plane.	99
5.14	NACA 0012 airfoil - pitching.	101
5.15	NACA 0012 airfoil - comparison between the numerical analysis to the Theodorsen theory and the experimental data in terms of lifting coefficient resulting from pitching motion.	101
5.16	example of pitching motion for a NACA 0012 airfoil.	102
5.17	single-bladed vertical-axis turbine - rigid panel wake.	104
5.18	single-bladed vertical-axis turbine - Numerical instability of panel methods with flexible panel wakes.	105
5.19	single-bladed vertical-axis turbine - DIAS vorton wake.	106
5.20	single-bladed vertical-axis turbine - solution stability of panel methods with vorton wakes during the intersection of the wake with the body.	107
5.21	single-bladed vertical-axis turbine - radial forces on blade during a revolution. Numerical result compared to experimental data.	108

5.22	single-bladed vertical-axis turbine - tangential forces on blade during a revolution. Numerical result compared to experimental data.	109
5.23	three bladed turbine - vorotn wakes.	110
5.24	three bladed turbine - radial force.	111
5.25	three bladed turbine - tangential force.	111
5.26	three bladed turbine - power.	112
5.27	3D view of the intersection of the wake of an upstream pitching and heaving wing with downstream wing for both the doublet wake (on upper side) and vorton wake model (on the lower side).	114
5.28	the lift coefficients of a pitching and heaving wing and a downstream fixed wing obtained using the doublet wake model.	115
5.29	the lift coefficients of a pitching and heaving wing and a downstream fixed wing obtained using the DIAS vorton wake model.	115
5.30	a model helicopter in hover - the evolution of the wake modeled with vortons.	117
5.31	a model helicopter in hover - the evolution of the thrust coefficient.	118
5.32	a model helicopter in hover - the lift coefficient distribution in several revolutions.	118

List of Tables

5.1	three wake models used for the simulations.	88
5.2	NACA63 mean line - analytical and numerical lift coefficients. . . .	94
5.3	three wake models used for the simulations.	97
5.4	elliptic wing at several degrees angles of attack - comparison between numerical and theoretical results.	98

Introduction

Panel Method Technology is commonly used in industrial applications for aeronautical and naval fluid dynamic time-dependent calculations. Some critical points of the classical panel methods have been overcome by a new BEM open-source method, called PaMS (**P**anel **M**ethod **S**olver), developed by using unstructured panel discretization, and by introduction of a wide variety of boundary and closure conditions. However, the impossibility to analyse the phenomena of intersection of wakes with body surfaces is the most significant drawback preventing the even more widespread use of these codes for some applications like, for example, vertical-axis turbines, rotors, intersection of the wing wake with the downstream horizontal plane. In panel methods, this drawback is overcome by introducing vorton wakes.

It is well-known that vortex methods are based on the discretization of the vorticity field in which the evolution of the computational elements is determined, in the Lagrangian description, by the governing equations. The automatic adaptivity of the computational elements and the rigorous treatment of boundary conditions at infinity makes classical vortex methods attractive. In this thesis, a new vortex method, called vorton method, will be analyzed to model wakes in panel methods. As it will be shown, the vorticity is replaced by a set of vortons which will be defined and analyzed in terms of potential and velocity fields, and the equations governing the vorton

evolution will be presented.

In order to discretize the wake into vortons, we will describe a vorton wake model in which the vortons are generated by the classical wake panels. Particularly, several models of conversion of wake panels to vortons will be analyzed in order to choose one that gives the higher accuracy.

Once the vorton wake model will be chosen, the panel method solver PaMS with vorton wakes will be validated by means of several test cases. In the end, different simulation examples will be made.

Chapter 1

PANEL METHODS: A BRIEF HISTORY

The panel methods are boundary element methods for solving the potential flow around aerodynamic bodies, and they were first studied in 1958, when Smith and Pierce, while working at Douglas Aircraft Company, used a discrete form of the boundary integral equations in order to solve the potential flow around bodies of revolution. The early panel methods were almost exclusively of Neumann type, using either source or vorticity distributions over the surface. The finite element and finite difference methods were often substituted by the panel methods in computations characterized by complex geometric configurations, especially for external flows.

Though the versatility includes three-dimensional arbitrary body configurations, these constant-strength source panel methods can solve only non-lifting problems. In 1967, a work presented by Hess and Smith showed that the computation of forces on lifting bodies by using panel methods is possible for both two-dimensional and three-dimensional bodies.

A wide variety of practical problems in aerodynamics has been solved

using the panel methods, with the velocity potential constructed from distributions of sources and normal dipoles on each panel of the discretized boundary surface. In fact, the predictions of such methods have been in a good agreement with experiment over a surprisingly large range of flow conditions. Hess and Smith used constant-strength distributions on quadrilateral panels and derived closed-form expressions from the matrix elements by analytical evaluation of the surface integrals over each panel: the surface integrals of the source and doublet distributions are reduced to line integrals around the perimeter of every single panel [45].

By 1973, 3D subsonic panel methods began to affect the design and analysis of aircraft configurations at Boeing. Particularly, the Boeing TA230 program was one of the first computer programs for attacking arbitrary potential flow problems with Neumann boundary conditions which combined the source panel scheme of the Douglas Neumann program with variations of the vortex lattice technology. The TA230 program was characterized by its ability to handle any well-posed Neumann boundary value problems. In the same year, Boeing acquired a CDC 6600 for scientific computing, which consented to solve problems involving hundreds of panels, and so to model full configurations with the fidelity necessary to understand component interactions.

The TA230 panel code was used in the initial design phase of the B747 Space Shuttle Carrier Aircraft (see figure 1.1). In order to minimize the cost of the program, this panel method was extensively used for several purposes. At the conclusion of the design phase, the final selected configurations were tested in the wind tunnel to verify predictions with an excellent agreement resulting between the analyses and wind tunnel data.

The success of the TA230 code caused the strong demand among Boeing

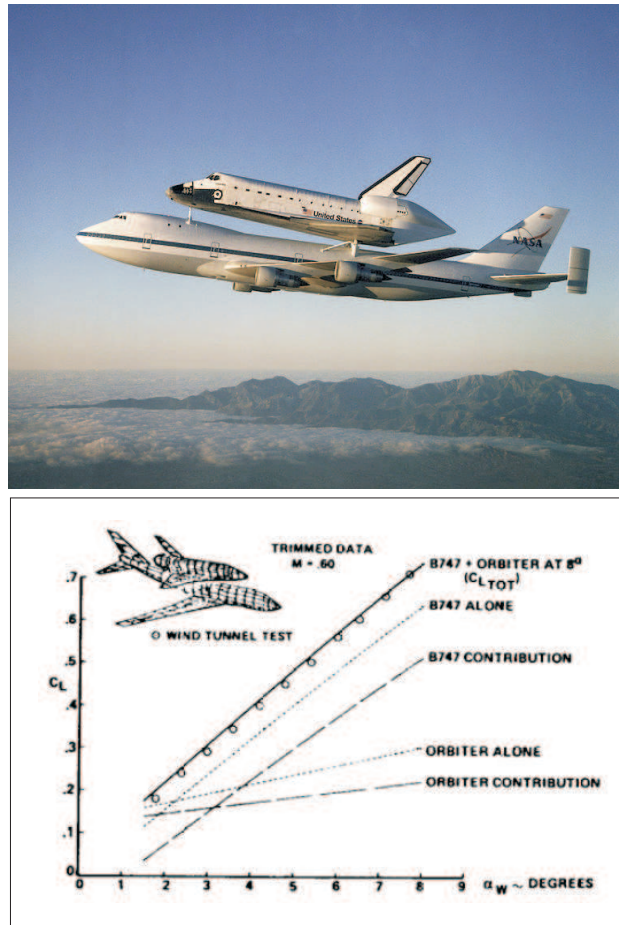


Figure 1.1: B747 with Space Shuttle Orbiter - lift coefficient [32].

aerodynamicists and the beginning of the paradigm shift toward acceptance of CFD as an equal partner of the wind tunnel and flight test in the analysis and design of commercial aircraft. However, this code presented some disadvantages. First, to model correctly a complex flow for which no previous user experience was available, the engineer had to understand the mathematical properties and limitations of potential flow. In addition, numerical problems arose when panel shapes and sizes varied, and fine paneling in regions of rapid flow variations often forced fine paneling in otherwise. Furthermore, since numerical accuracy was strongly affected by local curvature and singularity

strength gradient, excessive numbers of panels were required. Consequently to these limitations of the TA230 code, Boeing developed a panel method under contract to NASA resulted in PAN AIR / A502, on quadratic basis, flat-sub-element high order panel method [32].

During the 1980s, several variations of different complexity of the surface singularity boundary element method were introduced for potential transonic and supersonic flows. Particularly, high order methods were developed for the benefits of increasing solution accuracy as well as for satisfying the solution continuity requirements imposed by supersonic flow applications. In fact, linear distributions have been used on triangular panels to provide a more continuous description of the solution. Moreover, steady surface panel methods were also extensively applied to the calculation of wake simulations.

Large-scale panel method solutions were obstructed by limitations on computational time and memory although the great advances in computational power in the 1980s. Moreover, limitations on the practical use of panel methods existed due to the coarseness of surface discretizations though solutions of several thousand panels became a routine performed on large computers. Development in three dimensional solvers was followed by two dimensional panel methods which were being developed and used heavily for inverse airfoil design for a long time: XFOIL is an example. Furthermore, the panel methods were coupled with the use of boundary layer for incorporating viscous effects.

Applications of unsteady three-dimensional panel methods to aerodynamic problems became extensive in the late 1980s with solutions including both time domain and frequency domain methods. The studies by Katz [33][8] are examples of three-dimensional time domain panel methods, extended also to the calculation of multiple bodies.

In the late 1980s PMARC (Panel Method Ames Research Center) [7][6] was created within NASA Ames Research Center to predict numerically flow fields around complex three-dimensional geometries and was later released as a controlled access computer program. PMARC was derived from a code named VSAERO (at the present time, one of the most used panel method softwares) that was developed for Ames Research Center by Analytical Methods, Inc. The first objective in the development of this code was a fast code with an open source to facilitate making modifications or adding new features. The second objective was to create an adjustable-size panel code. PMARC (at the present time, there exists also the modern version CMARC, written in C++) included several advanced features such as internal flow modeling for ducts and wind tunnel test sections and a time-stepping wake model which allows the study of time-dependent motions, including problems involving relative motion.

Although by the 1990s panel methods had largely given way to higher fidelity Navier-Stokes and Euler solvers, several Lagrangian based approaches were developed. Particularly, the vorton method, also referred to as vortex particle method, was refined and further studied for the simulation of largely vortical flow [53][65][2] and some history and development of vortex particle methods will be described in the following section.

Today, the panel methods continue to be widely used, in particular, for initial design studies due to their ease of use (result of the surface discretization only).

1.1 Vorton methods: background

Vorton methods were first studied in the 1930s when Rosenhead performed a dynamical vortex calculation using singular point vortices in order to solve the problem of potential flow around bodies and so to compute the loads around the aerodynamic configurations [52], later repeated by several authors. Rosenhead wrote an expression for a desingularized vorton and Leonard discussed vorton core functions for two-dimensional particle methods (observe that desingularization the Biot-Savart equation is different in using finite-core vortons, though both make the vortex sheet well-posed) [55]. Moreover, Rosenhead was the first to consider the evolution of the vorticity discretized into element vortices.

The early studies on vorton methods in three-dimensions used vortex filament approximations to account for the domain vorticity: Chorin presented three-dimensional vortex blob calculations, though stretch was computed using a local segment approximation, making essential a vortex filament method. The classical vortex filament methods were constructed for modeling vortex filament evolution in inviscid flows. In this sense, the use of a vorton represents another possibility to investigate perfect ideal flows where the computational elements in this case are spherical blobs of vorticity given by approximating thick vortex structures [38].

While the vortex filament method and the sheet method need to store the connectivity information, the first vorton method proposed by Beale and Majda [10] was characterized by the fact that the vortex blob positions and strengths were updated in a Lagrangian manner with no connection between the blobs. They first proposed using spherical particles for three-dimensional calculations, using Lagrangian update to compute stretch, and forgoing all element connection information.

Winckelmans and Leonard [65] presented a comparison of singular and regularized particle methods and their vorticity update equations.

Vorticity representation in panel methods has been traditionally limited to vorticity sheet and vortex filament approaches: vortons are used commonly for representing vorticity in unsteady two-dimensional problems.

At the present state of development, the combined three-dimensional panel method and vortex particle approach represents an important tool in many different applications: body surfaces, container boundaries, free-surfaces, plumes, jets, and wakes in unsteady three-dimensional flow fields [57][45][62][18][43][2][39]. Moreover, many current vorton methods are used for the simulation of turbulent flows.

The most important advantage of vorton methods is that they are the answer to a common problem characterizing the panel methods: intersection of the wake with downstream body surfaces. The use of vorton wakes permits to model the unsteady aerodynamics of aircraft in close proximity, which is important for quantifying the wake-vortex hazard on following aircraft, such as the method presented by Ramsey and Milgram [51], based on extensions of unsteady vortex lattice able to reduce numerical instabilities associated with discretized vortex sheets. In addition, these methods do not require a sufficiently high density of vortex particles to model practically and accurately the vortex sheet, even though some authors support the opposite [63]. Moreover, these approaches do not suffer from large computational times and low accuracy but ever cause the reduction of the computational times and the increase in accuracy which depends on many things, most notably the choice of cutoff function and core radius, and the initialization of the vorticity distribution.

Chapter 2

INCOMPRESSIBLE AND INVISCID FLOWS

In this chapter, the emphasis is on the incompressible and inviscid flows on which classical panel methods are based. In order to model the wake by means of the vorticity method, the velocity field will be defined by the well-known Helmholtz decomposition. For inviscid flows, the velocity field may be described by means of the decomposition into two velocity components that have a kinematic significance: a rotational component counts for the velocity field due to the vorticity in the flow whereas a potential component is used in order to enforce the boundary conditions and to ensure the compatibility of the velocity and the vorticity field in the presence of boundary. In order to consider the inviscid evolution of the vorticity field generated by the aerodynamic configurations, the mechanism of generation and shedding of the vorticity from the surface of the body into the wake is expressed in terms of the Kutta condition.

2.1 The domain

Consider the external flow field surrounding a three dimensional lifting body. The domain of interest includes all fluid external to the body surfaces (see figure 2.1). In general, the lifting configuration (e.g.: aircraft) consists of the wing, the vertical tail and the horizontal stabilizer. Each lifting part has a sharp trailing edge from which trailing vortex wakes sheds.

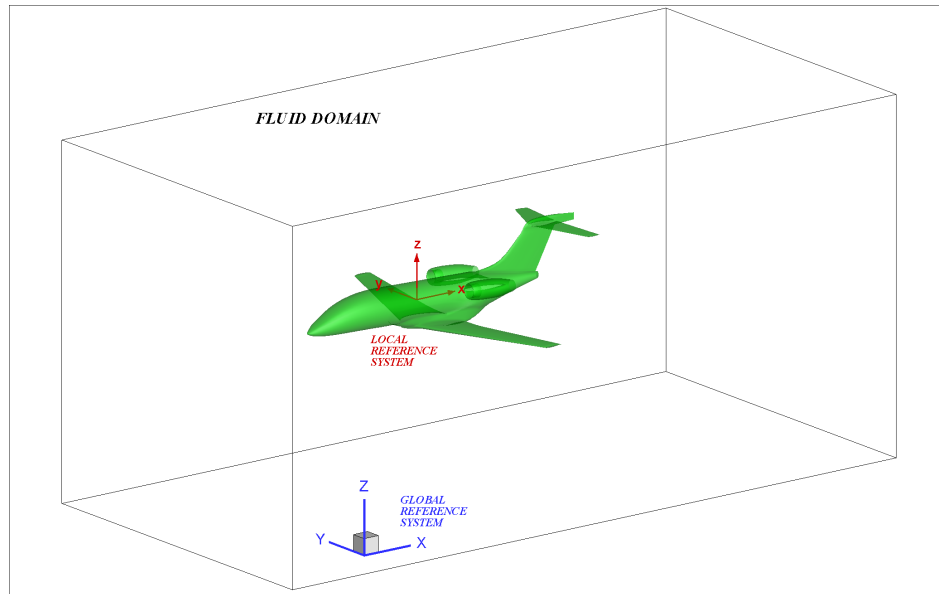


Figure 2.1: the fluid domain.

Prescribe a three-dimensional coordinate system to describe mathematically the flow of fluid through three-dimensional space. Consider the most common orthogonal coordinate system: the cartesian coordinate system. The x , y , and z are mutually perpendicular, and \mathbf{i} , \mathbf{j} , and \mathbf{k} are unit vector in the x , y , and z directions, respectively. A arbitrary point P in the domain at a given time is located by the position vector \underline{r} , where

$$\underline{r} = \underline{r}(x, y, z, t) = x(t)\mathbf{i} + y(t)\mathbf{j} + z(t)\mathbf{k} \quad (2.1)$$

If the fluid velocity is denoted by \underline{U} , it can be expressed as

$$\underline{U} = \underline{U}(x, y, z, t) = U_x(t)\mathbf{i} + U_y(t)\mathbf{j} + U_z(t)\mathbf{k} \quad (2.2)$$

where $U_x(t)$, $U_y(t)$ and $U_z(t)$ represent the scalar component of \underline{U} , at a given time, along the x , y , and z directions, respectively.

The flow around the body is assumed to be inviscid and incompressible, any vorticity in the domain is localized on the thin wake regions trailing the lifting surfaces; these assumptions greatly simplify the form of the Navier-Stokes equations, commonly used to solve fluid-dynamic problems.

First, consider the hypothesis of inviscid flow. A flow that is assumed to involve no friction, thermal conduction, or diffusion is called inviscid flow. This kind of flow do not exist in nature but there are many practical flows where the influence of mass diffusion, viscosity, and thermal conduction is small. In these cases, it is possible to model the inviscid flows.

Theoretically, the flow is assumed to be inviscid in the limit as the Reynolds number Re goes to infinity where the Reynolds number is physically a measure of the ratio of inertia forces to viscous forces in a flow. For many practical problems, even though this high but finite parameter, the influence of the diffusive effects is limited to a very thin region adjacent to the body surface. This limited region is defined as the boundary layer and the flow is essentially inviscid outside this thin region. Therefore, the considered external domain is the region outside the boundary layer. For such Re , the flow is assumed to be inviscid.

It is well-known that inviscid theory by itself cannot give satisfactory results for the prediction of the total drag.

Now, consider the hypothesis of incompressible flow. Denote the density by ρ . A flow in which the density ρ is constant is called incompressible. All flows are compressible where a flow is called compressible where the density

is variable. Really incompressible flow does not occur in nature. Similarly to the discussion of inviscid flow, there are many aerodynamic problems that can be modeled as being incompressible. Theoretically, the flow of gases is assumed to be incompressible for $M < 0.3$ where the Mach number M is the ratio of the flow velocity to the speed of sound and like the Reynolds number, it is a powerful parameter in the study of gas dynamics. Practically, the flow of gases at low Mach number is essentially incompressible.

The equations of motion for a homogeneous fluid in the absence of reactions or mass diffusion are based on three physical conservation laws¹ [31]. Since the average measurable values of the flow properties are desired for aerodynamic applications, the assumption of continuous distribution of matter is imposed: this assumption is known as continuum. So the governing equations of fluid motion are derived from conservation of mass, momentum and energy equations. The resulting system of equations is known as the Navier-Stokes equations.

Since the flow is assumed to be isothermal, this leads generally to a decoupling of the energy equation from the other conservation laws. Therefore, the velocity and pressure fields are computed initially, and subsequently the energy equation may be solved for the temperature field. For flows involving temperature variations, the coupling between the temperature field and the fluid motion can occur through various effects, such as variations of viscosity or heat conductivity with temperature, influence of external forces function of temperature.

Moreover, this system of equations for incompressible flow presents a particular situation in which the unknown pressure does not appear under a time dependence form due to the non-evolutionary character of the continuity

¹When a fluid is a composition of several chemical species with mass diffusion and/or chemical reaction, additional conservation laws may be required.

equation.

At this point, the vorticity will be briefly examined in order to introduce the role played by the vortex wake in the following chapters. This quantity is simply twice the angular velocity and is denoted by the vector $\underline{\omega}$. We know the following important result for the vorticity:

$$\underline{\omega} = \nabla \times \underline{U} \quad (2.3)$$

In a velocity field, the curl of the velocity is equal to the vorticity. Since the flow is rotational only on the thin wake region whereas it is assumed to be irrotational otherwise, $\nabla \times \underline{U} \neq 0$ at every point in the wake and $\nabla \times \underline{U} = 0$ at every point in the remaining domain.

An important result is the relation existing between vorticity and circulation. Assume that the surface is in a flow field and consider any point P on this surface. From Stokes' theorem²

$$\Gamma = - \oint_C \underline{U} \cdot d\underline{s} = - \int \int_S (\nabla \times \underline{U}) \cdot d\underline{S} \quad (2.4)$$

Therefore, the circulation about a curve C is equal to the vorticity integrated over any open surface bounded by C . Hence, if the flow is irrotational everywhere within the contour of integration, then $\Gamma = 0$, otherwise circulation results different from zero.

The importance to make a distinction between rotational and irrotational flows lies in the fact that irrotational flows are much easier to analyze than rotational flows even though the applications of irrotational flow are limited.

²Consider an open area S bounded by the closed curve C and let A be a vector field, the line integral of A over C is related to the surface integral of A over S by Stokes' theorem:

$$\oint_C \underline{A} \cdot d\underline{s} = \int \int_S (\nabla \times \underline{A}) \cdot d\underline{S}$$

Once the fluid domain have been described, see how to analyze the flow field. In the following section, it will be shown how the velocity vector can be expressed by means of a scalar potential component and a vector potential component by the Helmholtz decomposition.

2.2 The Helmholtz theorem

In a hydrodynamic context, Helmholtz showed in 1858 that any vector field that vanishes at infinity can be decomposed into two parts: one is an irrotational component which can be expressed by the gradient of a scalar function and the other is a rotational part which can be expressed by the curl of the vector function. This is the Helmholtz theorem which has very important applications in many physical problems, like the simulation of incompressible fluids (Navier-Stokes equations), or in electromagnetism (Maxwells equations).

As shown by Gui and Dou [28], the Helmholtz theorem states that if \underline{F} is an arbitrary continuous vector function with all the second order partial derivatives in free space, and its surface integration or its any partial derivative is zero at infinity, then this vector function can be defined as the sum of the gradient of a scalar function and the curl of a vector function, that is

$$\underline{F} = \underline{\nabla}\phi + \underline{\nabla} \times \underline{\Psi} \quad (2.5)$$

with

$$\phi = \int_V \frac{\underline{\nabla} \cdot \underline{U}(\underline{r})}{4\pi|\underline{r}|} dV \quad (2.6)$$

$$\underline{\Psi} = \int_V \frac{\underline{\nabla} \times \underline{U}(\underline{r})}{4\pi|\underline{r}|} dV \quad (2.7)$$

where $1/(4\pi|\underline{r}|)$ is the Green's function. Equations (2.6) and (2.7) will be derived by means of the Green's Identities in the continuation.

If the field function is any first order continuously differentiable vector function with all the second order partial derivatives bounded at infinity, then this vector function can be completely and uniquely decomposed into the sum of the gradient of a scalar function and the curl of a vector function as shown in formula (2.5).

Note that the applicable range of above proposition is restricted to simply connected domain with single boundary surface. Since the fluid domain defined in the previous section, is a simply connected domain therefore the above proposition is applicable in the case of interest.

Observe that, for the vector function \underline{F} , the following vector identities result to be valid

$$\underline{\nabla} \cdot (\underline{\nabla}\phi + \underline{\nabla} \times \underline{\Psi}) \rightarrow \nabla^2\phi = \underline{\nabla} \cdot \underline{F} \quad (2.8)$$

$$\underline{\nabla} \times (\underline{\nabla}\phi + \underline{\nabla} \times \underline{\Psi}) \rightarrow \underline{\nabla}(\underline{\nabla} \cdot \underline{\Psi}) - \nabla^2\underline{\Psi} = \underline{\nabla} \times \underline{F} \quad (2.9)$$

where, by definition

$$\underline{\nabla} \cdot (\underline{\nabla} \times \underline{\Psi}) = 0 \quad (2.10)$$

$$\underline{\nabla} \times (\underline{\nabla}\phi) = \underline{0} \quad (2.11)$$

Note that, for the Helmholtz decomposition, the chose of $\underline{\Psi}$ can be arbitrary, therefore $\underline{\Psi}$ may be solenoidal or not divergence-free. Instead, as it is shown in further on, the characteristics of the vector \underline{F} depends on another considerations.

Now, if the vector potential $\underline{\Psi}$ and the vector function \underline{F} are solenoidal, equations (2.8) and (2.9) become

$$\nabla^2\phi = 0 \quad (2.12)$$

$$- \nabla^2\underline{\Psi} = \underline{\nabla} \times \underline{F} \quad (2.13)$$

Equations (2.12) and (2.13) are Laplace's equation and Poisson's equation, respectively. Therefore, the problem can be worked out by solving one Laplace's equation for the irrotational component and one Poisson's equation for the solenoidal component. Equations (2.6) and (2.7) are the solutions of Laplace's equation and Poisson's equation, respectively.

2.2.1 The velocity definition

By means of the Helmholtz decomposition, the velocity vector can be expressed by means of a scalar potential component and vector potential component.

Regarding the rotationality of the flow field due to thin vortex wake, it's possible to introduce a stream function such that

$$\underline{U}_\Psi = \underline{\nabla} \times \underline{\Psi} \quad (2.14)$$

where $\underline{\Psi}(x, y, z, t)$ is the vector potential for the velocity in the flow domain. Observe that the the definition of $\underline{\Psi}$ is statement of the mass conservation. In fact, $\underline{\Psi}$ automatically satisfies the continuity equation, since the gradient of the curl of any vector is identically zero. From a physical point of view, the lines of a constant $\underline{\Psi}$ represent stream lines, and the difference in the values of $\underline{\Psi}$ between two streamlines gives the volumetric flow rate between the two.

One important consequence of irrotationality is the existence of a velocity potential. Indeed, the equation $\underline{\xi} = \underline{\nabla} \times \underline{U} = \underline{0}$ is a necessary and sufficient condition for the existence of a potential ϕ such that

$$\underline{U}_\phi = \underline{\nabla}\phi \quad (2.15)$$

where $\phi(x, y, z, t)$ is the scalar potential for the velocity in the flow domain.

This scalar potential consents the substitution of a three-component vector by a single scalar as the principle unknown in theoretical investigation.

The velocity potential is analogous to stream function in the sense that derivatives of ϕ yield the velocity but there are distinct differences between ϕ and $\underline{\Psi}$. First, the velocity is obtained by differentiating ϕ in the velocity direction, whereas $\underline{\Psi}$ in the direction normal to the velocity direction. Second, the velocity potential is defined only for irrotational flow, whereas the stream function can be defined for rotational or irrotational flows.

Finally, the fluid velocity, $\underline{U}(\underline{r}, t)$ at a given point in the domain is defined as the superposition of a scalar potential component, $\underline{U}_\phi(\underline{r}, t)$, and a solenoidal vector potential component, $\underline{U}_\Psi(\underline{r}, t)$, by a Helmholtz decomposition:

$$\underline{U}(\underline{r}, t) = \underline{U}_\phi(\underline{r}, t) + \underline{U}_\Psi(\underline{r}, t) = \nabla\phi + \nabla \times \underline{\Psi} \quad (2.16)$$

In the inviscid and incompressible flows, the Helmholtz decomposition is not usually considered. However, as the traditional scalar potential boundary element method formulation, so the vector potential boundary element method formulation will be described in the following chapters.

2.3 The scalar potential relationship: Laplace's equation

Consider the conservation equation:

$$\frac{\partial \rho}{\partial t} + \nabla \cdot (\rho \underline{U}) = 0 \quad (2.17)$$

For incompressible flow, $\rho(x, y, z, t)$ is constant. Therefore,

$$\partial \rho / \partial t = 0 \quad (2.18)$$

and

$$\underline{\nabla} \cdot (\rho \underline{U}) = \rho \underline{\nabla} \cdot \underline{U} \quad (2.19)$$

Then, the governing continuity equation for a fluid with a constant density is expressed in differential form as:

$$\underline{\nabla} \cdot \underline{U} = 0, \quad (2.20)$$

where $\underline{\nabla} \cdot \underline{U}$ is physically the time rate of change of the volume of a moving fluid element per unit volume. Substituting the velocity potential relationship into the above relationship, the resulting equation simplifies to:

$$\underline{\nabla} \cdot (\underline{\nabla}\phi + \underline{\nabla} \times \underline{\Psi}) = \underline{\nabla} \cdot (\underline{\nabla}\phi) = \nabla^2\phi = 0 \quad (2.21)$$

This is Laplace's equation for the velocity scalar potential. Note that Laplace's equation is a linear differential equation and solutions of Laplace's equation are called harmonic functions: this is an elliptic differential equation that results in a boundary-value problem. Since the fluid's viscosity has been neglected, the no-slip boundary condition on a solid-fluid boundary cannot be enforced.

Moreover, the fact that Laplace's equation is linear is very important, because the superposition of any solution of a linear differential equation is also a solution of Laplace's equation. This fact implies that the solution of a complicated flow pattern for an incompressible flow can be obtained as the sum of a number of elementary incompressible flow solutions.

2.4 The vector potential relationship: Poisson's equation

Remember that the vorticity field $\underline{\omega}(\underline{r}, t)$ is defined as the curl of the velocity:

$$\underline{\nabla} \times \underline{U} = \underline{\omega} \quad (2.22)$$

Thus, by using Helmholtz decomposition in above equation, this becomes:

$$\underline{\nabla} \times (\underline{\nabla}\phi + \underline{\nabla} \times \underline{\Psi}) = \underline{\omega} \quad (2.23)$$

Since the curl of a gradient of a scalar is zero, the vorticity field is:

$$\underline{\nabla} \times (\underline{\nabla} \times \underline{\Psi}) = \underline{\omega} \quad (2.24)$$

By using the vector Laplacian relation, equation (2.24) becomes:

$$\underline{\nabla} \times (\underline{\nabla} \times \underline{\Psi}) = \underline{\nabla}(\underline{\nabla} \cdot \underline{\Psi}) - \nabla^2 \underline{\Psi} = \underline{\omega} \quad (2.25)$$

Since the vector potential is solenoidal, the vorticity field is simply:

$$\nabla^2 \underline{\Psi} = -\underline{\omega} \quad (2.26)$$

which is Poisson's equation relating the vector potential to the vorticity.

2.5 The velocity induced by vorticity: the Biot-Savart law

Determine, now, the velocity induced by a vorticity distribution (see figure 2.2). Consider Poisson's equation $\underline{\omega} = -\nabla^2 \underline{\Psi}$. The solution of this equation, using Green's theorem, is

$$\underline{\Psi} = \frac{1}{4\pi} \int_V \frac{\underline{\omega}}{|\underline{r}_0 - \underline{r}_1|} dV \quad (2.27)$$

where $\underline{\Psi}$ is evaluated at point P which is a distance r_0 from the origin and is obtained by integration of the vorticity at point r_1 within the volume V . Equation above and equation (2.7) are the same relationship. Clearly, the velocity is the curl of $\underline{\Psi}$

$$\underline{U}_{\Psi} = \frac{1}{4\pi} \int_V \underline{\nabla} \times \frac{\underline{\omega}}{|\underline{r}_0 - \underline{r}_1|} dV \quad (2.28)$$

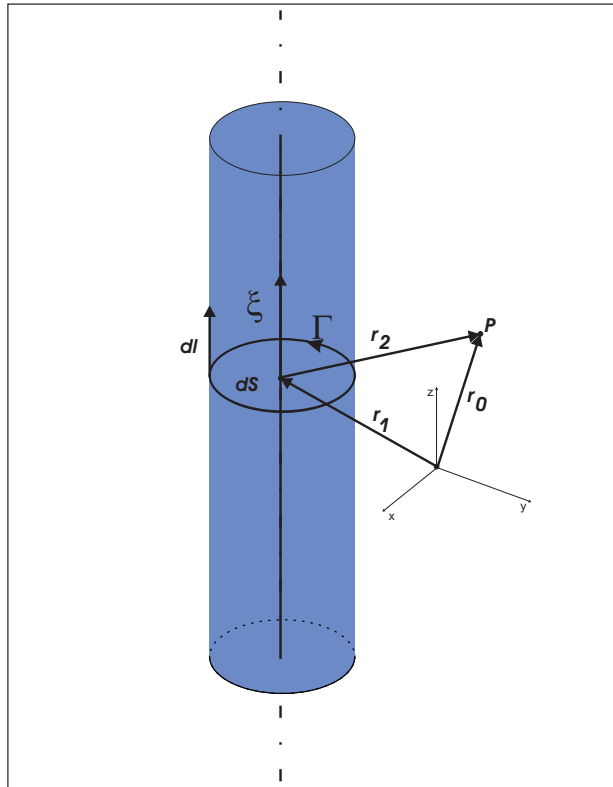


Figure 2.2: the velocity at point P induced by a vortex distribution.

Consider, then, an infinitesimal piece of the vorticity filament $\underline{\omega}$. Select the cross section area dS so that it is normal to $\underline{\omega}$ and the direction $d\ell$ on the filament is

$$d\ell = \frac{d\ell}{\omega} \underline{\omega} \quad (2.29)$$

Since the circulation Γ and dV are, respectively

$$\Gamma = \omega dS \quad (2.30)$$

$$dV = dS dl \quad (2.31)$$

then the integral term becomes

$$\nabla \times \frac{\omega}{|\underline{r}_0 - \underline{r}_1|} = \nabla \times \Gamma \frac{d\underline{\ell}}{|\underline{r}_0 - \underline{r}_1|} = \Gamma \frac{d\underline{\ell} \times (\underline{r}_0 - \underline{r}_1)}{|\underline{r}_0 - \underline{r}_1|^3} \quad (2.32)$$

By substituting the above result in equation (2.28), resulting equation is the Biot-Savart law, which states

$$\underline{U}_\Psi = \frac{1}{4\pi} \int_V \Gamma \frac{d\underline{\ell} \times (\underline{r}_0 - \underline{r}_1)}{|\underline{r}_0 - \underline{r}_1|^3} dV \quad (2.33)$$

or in differential form

$$\Delta \underline{U}_\Psi = \frac{\Gamma}{4\pi} \frac{d\underline{\ell} \times (\underline{r}_0 - \underline{r}_1)}{|\underline{r}_0 - \underline{r}_1|^3} \quad (2.34)$$

In case of a volume distribution of vorticity, a similar manipulation of equation (2.28) leads to the following result

$$\underline{U}_\Psi = \frac{1}{4\pi} \int_V \frac{\omega \times (\underline{r}_0 - \underline{r}_1)}{|\underline{r}_0 - \underline{r}_1|^3} dV \quad (2.35)$$

2.5.1 The velocity induced by a straight vortex segment

The first to make use of a vortex filament concept in the analysis of inviscid, incompressible flow was Helmholtz which established several basic principles known as Helmholtz theorems. First, the strength of a vortex filament is constant along its length. Second, a vortex filament cannot end

in a fluid: it must extend to the boundaries of the fluid which may be $\pm\infty$ or form a closed path.

The derivation of the velocity induced by a straight vortex segment $d\ell$ is based on the the Biot-Savart law. As a vortex line cannot start or end in a fluid, the contribution of a segment is one of a section of a continuous vortex line. Moreover, the components of the velocity induced by this vortex segment will be only tangential components.

Let \underline{r}_1 and \underline{r}_2 be the positions of the two edges of the vortex segment. The vector connecting the edges is

$$\underline{r}_0 = \underline{r}_2 - \underline{r}_1 \quad (2.36)$$

Then, the distance d and the cosines of the angles β_1 and β_2 are

$$d = \frac{|\underline{r}_1 \times \underline{r}_2|}{|\underline{r}_0|} \quad (2.37)$$

$$\cos \beta_1 = \frac{\underline{r}_0 \cdot \underline{r}_1}{|\underline{r}_0| |\underline{r}_1|} \quad (2.38)$$

$$\cos \beta_2 = \frac{\underline{r}_0 \cdot \underline{r}_2}{|\underline{r}_0| |\underline{r}_2|} \quad (2.39)$$

The velocity $\underline{U}_{\Psi_{1,2}}$ has the direction normal to the plane defined by the point P and the vortex edges 1,2 and the directional vector is given by

$$\frac{\underline{r}_1 \times \underline{r}_2}{|\underline{r}_1 \times \underline{r}_2|} \quad (2.40)$$

By substituting these quantities, the induced velocity is

$$\underline{U}_{\Psi_{1,2}} = \frac{\Gamma}{4\pi} \frac{\underline{r}_1 \times \underline{r}_2}{|\underline{r}_1 \times \underline{r}_2|} \underline{r}_0 \cdot \left(\frac{\underline{r}_1}{r_1} - \frac{\underline{r}_2}{r_2} \right) \quad (2.41)$$

Constant-strength vortex line segments can be used to model the wing or the wake for lifting flows, as provided in chapters 2 and 3.

2.6 The vorticity evolution equation

The vorticity evolution equation is derived from the Euler equations,

$$\frac{\partial \underline{U}}{\partial t} + \underline{U} \cdot \underline{\nabla} \underline{U} = -\frac{\underline{\nabla} p}{\rho} + \nu \nabla^2 \underline{U} \quad (2.42)$$

where ρ is the fluid density, p is the pressure and ν is the cinematic viscosity. Taking the curl of above equation, the resulting equation for the vorticity evolution in the domain is

$$\underline{\nabla} \times \frac{\partial \underline{U}}{\partial t} + \underline{\nabla} \times (\underline{U} \cdot \underline{\nabla} \underline{U}) = -\underline{\nabla} \times \left(\frac{\underline{\nabla} p}{\rho} \right) + \underline{\nabla} \times (\nu \nabla^2 \underline{U}) \quad (2.43)$$

For fixed reference frames, the first term on the left side becomes

$$\underline{\nabla} \times \frac{\partial \underline{U}}{\partial t} = \frac{\partial (\underline{\nabla} \times \underline{U})}{\partial t} = \frac{\partial \underline{\omega}}{\partial t} \quad (2.44)$$

Similarly, the last term on the right side becomes

$$\underline{\nabla} \times (\nu \nabla^2 \underline{U}) = \nu \nabla^2 \underline{\omega} \quad (2.45)$$

Now, since there exists the identity $\underline{\nabla} \times \underline{\nabla} \cdot = 0$, the pressure term vanishes, provided that the density is uniform

$$\underline{\nabla} \times \left(\frac{\underline{\nabla} p}{\rho} \right) = \underline{0} \quad (2.46)$$

The inertial term $\underline{U} \cdot \underline{\nabla} \underline{U}$ can be rewritten as

$$\underline{\nabla} \times (\underline{U} \cdot \underline{\nabla} \underline{U}) = \underline{\nabla} \times \left(\frac{U^2}{2} \right) - \underline{U} \times \underline{\omega} \quad (2.47)$$

and then the term $\underline{\nabla} \times (\underline{U} \cdot \underline{\nabla} \underline{U})$ can be written

$$\underline{\nabla} \times (\underline{U} \cdot \underline{\nabla} \underline{U}) = \underline{\nabla} \times \underline{\nabla} \times \left(\frac{U^2}{2} \right) - \underline{\nabla} \times (\underline{U} \times \underline{\omega}) \quad (2.48)$$

$$= \underline{U} \cdot \underline{\nabla} \underline{\omega} - \underline{\omega} \cdot \underline{\nabla} \underline{U} + \underline{\omega} (\underline{\nabla} \cdot \underline{U}) + \underline{U} (\underline{\nabla} \cdot \underline{\omega}) \quad (2.49)$$

$$= \underline{U} \cdot \underline{\nabla} \underline{\omega} - \underline{\omega} \cdot \underline{\nabla} \underline{U} \quad (2.50)$$

Putting everything together, the vorticity equation results

$$\frac{\partial \underline{\omega}}{\partial t} + \underline{U} \cdot \nabla \underline{\omega} = \underline{\omega} \cdot \nabla \underline{U} + \nu \nabla^2 \underline{\omega} \quad (2.51)$$

where the first term $\underline{\omega} \cdot \nabla \underline{U}$ on the right hand side represents the vorticity stretching (or how the strength and magnitude of the vorticity changes as it is exposed to velocity gradients in the fluid field). In chapter 2 it will be discussed that the stretching term may be neglected in certain applications.

Since the flow is assumed to be inviscid ($Re \rightarrow \infty$), then the vorticity can be rewritten as

$$\frac{\partial \underline{\omega}}{\partial t} + \underline{U} \cdot \nabla \underline{\omega} = \underline{\omega} \cdot \nabla \underline{U} \quad (2.52)$$

Observe that, for vary high values of the Reynolds, the vorticity that is created at the body surface is convected along with the flow much faster than it can be diffused out across the flow. So the vorticity remains in the confines of the thin region that includes the boundary layer and the trailing wake. The fluid in the outer part of the fluid domain is effectively irrotational. However, since the fluid has been assumed to be ideal in this thesis, the vorticity is only confined in the wake: the boundary layer does not exist in ideal fluids.

Recall, now, that the evolution equation for a material line element $\underline{\delta \ell}$ can be written as follow:

$$\frac{D \underline{\delta \ell}}{Dt} = \underline{\delta \ell} \cdot \nabla \underline{U} \quad (2.53)$$

It is clear that vortex lines move as material lines for inviscid flows.

Recalling, moreover, that a vortex tube is defined as the set of vortex lines that perforate a given surface part S and the circulation of a vortex tube is the same for all oriented surface patches that define the vortex tube due to free divergence of $\underline{\omega}$, the circulation of a vortex tube is conserved for inviscid flows. Vortex tubes move as material volumes and they conserve

their circulation. All these facts represent the basis for the method of vortex filaments.

2.7 The boundary conditions

Consider the incompressible flow fields over different aerodynamic bodies. It is clear that each flow is going to be distinctly different because of the different geometry. But these different flows are all governed by the same equations: $\nabla^2\phi = 0$ and $\nabla^2\Psi = -\underline{\omega}$. How, then, can the exact solution be found? The answer to these questions lies in the fact that, as known, in every single mathematic model, the boundary conditions must be considered like integral part of the same model. Moreover, in this unsteady flow problem, the unsteady nature of the boundary conditions must be considered for the solution uniqueness for all times. This unsteady nature can be due to changes in time of the velocity vector of the uniform flow that collides the body, or changes in time of the position and the form of the body surface, or changes in times of the form of possible flexible surfaces like the wake and the surfaces of separation between different flows. These changes in time require the time updating of the boundary conditions.

Therefore, the boundary conditions need to be specified on all solid surface and at infinity, and updated in time. Moreover, to analyze aerodynamic bodies, a wing trailing edge condition (Kutta condition) that imposes a condition of smoothness on the flow field at the trailing edge is necessary .

2.7.1 Infinity boundary conditions

Since the boundary is located far away so that the flow properties on the boundary are not influenced by the body, then it is at infinity where

the disturbances due the body moving through a fluid that initially at rest decays to zero in all directions. Hence, at infinity,

$$\underline{U}(r, t) = \underline{\nabla}\phi + \underline{\nabla} \times \underline{\Psi} = \underline{U}_\infty \quad (2.54)$$

These are the boundary conditions on velocity at infinity.

2.7.2 Wall boundary conditions

Regarding the wall boundary condition, since the body has a solid surface, then the flow can not penetrate the surface. For viscid flows, the velocity is zero at the surface due to the friction between the fluid and the solid surface. However, since the flow is assumed to be inviscid, the velocity at the surface can be finite and tangent to the surface because the flow cannot penetrate the surface or not tangent to the surface for the case of a solid boundary with transpiration. For this work, it is assumed the case of solid surfaces with not transpiration. Clearly, this wall tangency condition implies a zero component of velocity normal to the surface.

Let \underline{n} be a unit vector normal to the surface. In terms of the vector and scalar potentials, the flow tangency conditions can be written as:

$$\underline{U} \cdot \underline{n} = (\underline{\nabla}\phi + \underline{\nabla} \times \underline{\Psi}) \cdot \underline{n} = 0 \quad (2.55)$$

Observe that only the normal velocity boundary condition is applied at the wall, because of the inviscid flow assumption. For the viscid flows, the conditions to apply to the body surface are two: one is the normal velocity boundary condition, other is the tangent velocity condition.

2.8 The wing trailing edge Kutta condition

The net force produced by surfaces with sharp geometric cusps when the body moves relative to a fluid, is due to the pressure distribution over the body surface. Flows from moving around these cusps are impeded by the fact that these requires infinite pressure stresses and therefore the flows tend to leave smoothly the sharp corner and shed a trailing shear wake. Since the flow is assumed to be inviscid and irrotational, a Kutta condition must be applied to all wing trailing edges for the physicalness of the solution. In fact, the Kutta condition states that the flow leaves the sharp trailing edge of an airfoil smoothly and the velocity there is finite.

In the case of aerodynamic bodies, the capacity to manage the following Kutta wake, if necessary, its fluctuations cover an important role, so the wing trailing edge Kutta condition must be applied in time.

Moreover, since the trailing edge angle is finite, the normal component of the velocity, from both sides of the airfoil, must vanish. For a continuous velocity, this is possible if the pressure difference is zero:

$$\Delta p_{T.E.} = 0 \tag{2.56}$$

this is the Kutta condition which requires that there is no pressure jump across the trailing edge.

Additionally, this can be obtained by requiring that the flow above the wing be vorticity free. The Kutta condition along the trailing edge, so that the vorticity component parallel to the trailing edge ($\gamma_{T.E.}$) is zero, results:

$$\gamma_{T.E.} = 0 \tag{2.57}$$

In order to prescribe the streamwise vorticity release at the trailing edge,

a linearized version of the pressure continuity at the trailing edge is used

$$\phi_{upper} - \phi_{lower} = \Delta\phi_{wake} \quad (2.58)$$

Here, the subscripts *upper* and *lower* refer to points on the upper and lower surfaces of the trailing edge of the wing. The flow field without and with the imposition of the Kutta condition is presented in figure 2.3.

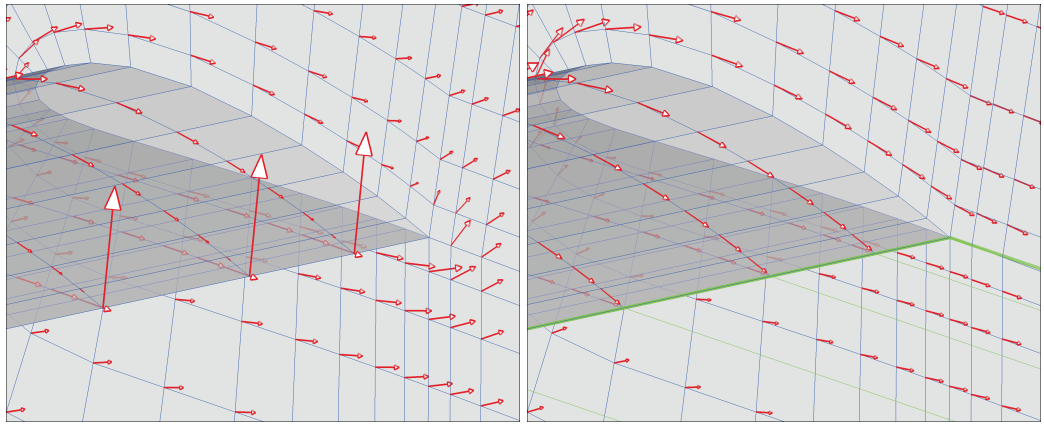


Figure 2.3: the flow field at the wing trailing edge without (left) and with (right) the imposition of the Kutta condition.

For unsteady flows, a time dependent component of the Kutta condition is also enforced. This additional condition requires that any increase in bound vorticity on the wing must be balanced by an equivalent increase in vorticity in the wake. This increased vorticity is oriented in the direction parallel to the trailing edge. The formal statement of the condition is the combined change with respect to time of the wing bound circulation and the wake circulation add to zero:

$$\left[\frac{d\Gamma_{span}}{dt} \right]_{wing} = - \left[\frac{d\Gamma_{span}}{dt} \right]_{wake} \quad (2.59)$$

where Γ represents the circulation strength of the wing and wake. Hence, the rate at which body vorticity increases must be equal and opposite to the rate of vorticity shed into the wake.

2.9 The Unsteady Bernoulli equation

The pressure field can be computed by Bernoulli equation, once the flow field is determinate. The Bernoulli equation is the most widely used equation in fluid mechanics, and assumes frictionless flow with no work or heat transfer.

Since this thesis presents a potential-vorticity approach, the applicable unsteady Bernoulli equation will be briefly derived, starting from the incompressible Euler equations:

$$\frac{\partial \underline{U}}{\partial t} + \underline{U} \cdot \nabla \underline{U} = -\frac{\nabla p}{\rho} \quad (2.60)$$

All space excluding the trailing vortex wake region have zero vorticity, therefore the resulting equation is:

$$\frac{\partial \underline{U}}{\partial t} + \frac{1}{2} \nabla |\underline{U}|^2 = -\frac{\nabla p}{\rho} \quad (2.61)$$

By using the Helmholtz decomposition, the above equation becomes:

$$\frac{\partial(\nabla\phi) + \partial(\nabla \times \underline{\Psi})}{\partial t} + \frac{1}{2} \nabla |\nabla\phi + \nabla \times \underline{\Psi}|^2 = -\frac{\nabla p}{\rho} \quad (2.62)$$

Collecting similar terms, and re-arranging, the above equation results

$$\frac{\partial(\nabla\phi)}{\partial t} + \frac{\partial(\nabla \times \underline{\Psi})}{\partial t} + \frac{1}{2} \nabla |\nabla\phi + \nabla \times \underline{\Psi}|^2 + \frac{\nabla p}{\rho} = 0 \quad (2.63)$$

Now, integrating the Bernoulli equation along the streamline from surface point x_1 , to a farfield reference point at ∞ where the velocity is zero since the body moves in the domain, and $p = p_\infty$ result in:

$$\int_\infty^{p_{x_1}} \frac{\partial(\nabla \times \underline{\Psi})}{\partial t} dC + \left(\frac{\partial\phi}{\partial t}_{x_1} + \frac{1}{2} |\nabla\phi + \nabla \times \underline{\Psi}|_{x_1}^2 \right) = \frac{p_\infty - p_{x_1}}{\rho} \quad (2.64)$$

Therefore, the term $\frac{\partial\phi}{\partial t}$, defined in an Eulerian reference frame, can be computed by converting of a body Lagrangian reference frame:

$$\frac{\partial\phi}{\partial t}|_{eulerian} = \frac{\partial\phi}{\partial t}|_{body} - \underline{U} \cdot \nabla\phi \quad (2.65)$$

The overall unsteady Bernoulli equation, used to determine the forces and pressures on the body, results:

$$\int_{\infty}^{p_{x_1}} \frac{\partial(\underline{\nabla} \times \underline{\Psi})}{\partial t} d\underline{C} + \frac{\partial\phi}{\partial t}|_{body} - \underline{U} \cdot \underline{\nabla}\phi + \frac{1}{2} |\underline{\nabla}\phi + \underline{\nabla} \times \underline{\Psi}|_{x_1}^2 = \frac{p_{\infty} - p_{x_1}}{\rho} \quad (2.66)$$

The importance of the unsteady term due to domain vorticity in the computation of the pressure will be discussed below. Now, note that this unsteady term is difficult to handle in the form:

$$\int_{\infty}^{p_{x_1}} \frac{\partial(\underline{\nabla} \times \underline{\Psi})}{\partial t} \cdot d\underline{C} \quad (2.67)$$

So, by considering the contribution of the vortex wake as an analogous contribution due to a doublet sheet, one can obtain:

$$\int_{\infty}^{p_{x_1}} \frac{\partial(\underline{\nabla} \times \underline{\Psi})}{\partial t} \cdot d\underline{C} = \int_{\infty}^{p_{x_1}} \frac{\partial\varphi}{\partial t}|_{wake} \cdot d\underline{C} \quad (2.68)$$

Integrating the expression for the wake potential φ is no more difficult to handle:

$$\int_{\infty}^{p_{x_1}} \frac{\partial\varphi}{\partial t}|_{wake} \cdot d\underline{C} = \frac{\partial\varphi}{\partial t} = \frac{\partial\varphi}{\partial t}|_{body} - \underline{U} \cdot \underline{\nabla}\varphi \quad (2.69)$$

where, $\underline{\nabla}\varphi$ is the velocity due to the wake. Therefore, the overall unsteady Bernoulli equation is:

$$\frac{\partial\varphi}{\partial t}|_{body} + \frac{\partial\phi}{\partial t}|_{body} - \underline{U} \cdot \underline{\nabla}(\phi + \varphi) + \frac{1}{2} |\underline{\nabla}\phi + \underline{\nabla} \times \underline{\Psi}|_{x_1}^2 = \frac{p_{\infty} - p_{x_1}}{\rho} \quad (2.70)$$

2.10 Computation of forces and moments

Once the pressure field has been determined by Bernoulli equation, the aerodynamic forces and moments on the lifting body can be computed. These quantities can seem complex but, in all cases, they are due to only two basic sources over the body surface:

- pressure distribution;

- shear stress distribution.

It's well-known that the only way nature has to communicate an aerodynamic force to a solid body moving through a fluid, is through the pressure and shear stress distributions which exist on the surface. Pressure and shear stress have the same dimension (force per unit area) and they vary along the surface. The first source acts normally to the body surface. The second source acts tangentially and it is due to the frictional effect of the flow “rubbing” against the surface as it moves around the body. The shear stress τ_w is defined as the force per unit area acting tangentially on the body surface due to friction.

The net effect of the pressure and shear stress distributions integrated over the complete body surface is a resultant aerodynamic force \underline{F} and moment \underline{M} on the body. Therefore, from the unsteady Bernoulli equation, the resultant force and moment can be computed as below:

$$\underline{F}(t) = \int_{S(t)} (p_\infty - p_{p_{x'}}(t)) \underline{n} \, dS(t) \quad (2.71)$$

$$\underline{M}(t) = \int_{S(t)} \underline{r}_{Gp} \times [(p_\infty - p_{p_{x'}}(t)) \underline{n}] \, dS(t) \quad (2.72)$$

where \underline{r}_{Gp} is the position of the point relative the the local body frame.

The resultant force can be split in two component: lift \underline{L} and drag \underline{D} . The first is defined as the component of \underline{F} perpendicular to the relative wind. The second is defined as the component of \underline{F} parallel to the relative wind.

Consider, now, viscous effects on drag. The presence of friction in a flow produces two sources of drag:

- skin friction drag D_f due to the shear stress at the wall;
- pressure drag due to flow separation D_p , called form drag.

Since the viscosity has been neglected in this work, the total drag cannot be satisfactory determined. In fact, it is possible to compute only the pressure

force with inviscid theory. However, there exists a source of drag induced by lift D_i that can be computed in inviscid theory too.

2.10.1 Pressure, force and moment coefficients

In fluid dynamics, it is common to use the pressure coefficient rather than pressure. The pressure coefficient C_p is a dimensionless pressure and its usefulness is known in aerodynamics, from subsonic to hypersonic flow. The pressure coefficient is defined as

$$C_p = \frac{p - p_\infty}{q_\infty} = \frac{p - p_\infty}{\frac{1}{2}\rho_\infty U_\infty^2} \quad (2.73)$$

The pressure coefficient is an important quantity because the distribution of C_p over the body surface leads directly to the value of the lift coefficient C_L (that will be defined later) and the calculation of the effect of Mach number M_∞ on C_L by the Prandtl-Glauert rule.

Similarly, the dimensional lift, drag, and moment coefficients can be defined from dimensional analysis, as

$$C_L = \frac{L}{q_\infty S} \quad (2.74)$$

$$C_D = \frac{D}{q_\infty S} \quad (2.75)$$

$$C_M = \frac{M}{q_\infty S c} \quad (2.76)$$

where S and c are the lifting body area and chord of reference, respectively.

Chapter 3

PANEL METHODS

In the previous chapter, the fundamental fluid dynamic equations and the conditions leading to the simplified ideal flow problem were formulated and discussed. Now, the emphasis is placed on the theory and the numerical procedure used to solve regions of the flow field assumed to be inviscid, incompressible and also irrotational. Therefore, the elementary solutions of Laplace equation and the basic methodology for obtaining the solutions of the more complex potential flow problems will be described in this chapter.

3.1 Basic solutions of Laplace equation

Laplace equation over bodies may be solved by the distribution of elementary solutions whose strengths are obtained by enforcing the impermeability flow or a fixed normal flow condition on the solid boundaries. But, when the complexity of the method increases, the calculation becomes more complicated. Therefore, some typical numerical elements upon which some numerical solutions are based, will be presented in this section. Particularly, attention is addressed to some three-dimensional constant-strength singularity elements

[12][33][23].

In the general case, the potential may be integrated over a curve, surface or volume, in order to generate the corresponding singularity elements. In these cases, it must not be addressed to strength (like in the case of point elements), but strength density per unit of length, area or volume, respectively.

Particularly, it is possible to imagine elementary solutions of Laplace equation that are distributed over plane geometric elements oriented in space: these elements may be quadrilateral or triangular. Therefore, let σ be the strength per unit of area for the distributed source, and analogously let μ for the distributed doublet. The validity of the equations which will be derived will be related to the plane quadrilaterals, but these may be applied also to triangular elements which are plane by definition.

Before to describe the three-dimensional constant-strength singularity elements, the free stream solution of Laplace equation will be briefly discussed.

The most simple solution of Laplace equation regards a uniform free stream. In fact, equation (2.21) is certainly fulfilled by the follow potential

$$\phi(x, y, z) = u_{\infty}x + v_{\infty}y + w_{\infty}z \quad (3.1)$$

which represents a uniform flow field

$$\underline{U} = \left(\frac{\partial\phi}{\partial x}, \frac{\partial\phi}{\partial y}, \frac{\partial\phi}{\partial z} \right) = (u_{\infty}, v_{\infty}, w_{\infty}) \quad (3.2)$$

3.1.1 Quadrilateral source

Begin to consider a surface element bounded by four straight lines, with a constant-strength source distribution σ (see figure 3.1). Consider a reference frame with origin in the quadrilateral center e with z axis directed along the

normal to the quadrilateral. Thus, the potential in any point P is given by:

$$\phi(x, y, z) = -\frac{\sigma}{4\pi} \iint_S \frac{dS}{\sqrt{(x-x_0)^2 + (y-y_0)^2 + z^2}} \quad (3.3)$$

Equation (3.3) may be rewritten by means of the Hess and Smith [30] pro-

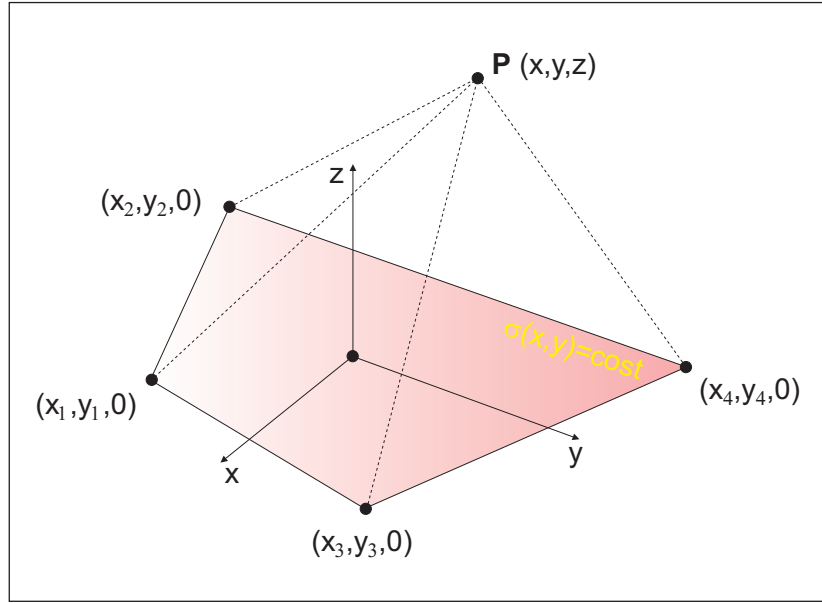


Figure 3.1: quadrilateral constant-strength source element.

cedure in function of the coordinates of the four quadrilateral vertexes:

$$\begin{aligned} \phi(x, y, z) = & -\frac{\sigma}{4\pi} \sum_{\binom{i}{j} = \binom{1,2,3,4}{2,3,4,1}} \frac{\hat{x}_i \hat{y}_{ij} - \hat{y}_i \hat{x}_{ij}}{d_{ij}} \ln \frac{r_i + r_j + d_{ij}}{r_i + r_j - d_{ij}} + \\ & -|z| \frac{\sigma}{4\pi} \sum_{\binom{i}{j} = \binom{1,2,3,4}{2,3,4,1}} \left[\tan^{-1} \left(\frac{m_{ij} e_i - h_i}{z r_i} \right) - \tan^{-1} \left(\frac{m_{ij} e_j - h_j}{z r_j} \right) \right] \end{aligned} \quad (3.4)$$

from which the velocity components derives:

$$u(x, y, z) = \frac{\sigma}{4\pi} \sum_{\binom{i}{j} = \binom{1,2,3,4}{2,3,4,1}} \frac{\hat{y}_{ij}}{d_{ij}} \ln \frac{r_i + r_j - d_{ij}}{r_i + r_j + d_{ij}} \quad (3.5)$$

$$v(x, y, z) = \frac{\sigma}{4\pi} \sum_{\binom{i}{j} = \binom{1, 2, 3, 4}{2, 3, 4, 1}} \frac{-\widehat{x}_{ij}}{d_{ij}} \ln \frac{r_i + r_j - d_{ij}}{r_i + r_j + d_{ij}} \quad (3.6)$$

$$w(x, y, z) = \frac{\sigma}{4\pi} \sum_{\binom{i}{j} = \binom{1, 2, 3, 4}{2, 3, 4, 1}} \tan^{-1} \left(\frac{m_{ij} e_i - h_i}{z r_i} \right) + \\ - \frac{\sigma}{4\pi} \sum_{\binom{i}{j} = \binom{1, 2, 3, 4}{2, 3, 4, 1}} \tan^{-1} \left(\frac{m_{ij} e_j - h_j}{z r_j} \right) \quad (3.7)$$

where

$$\begin{aligned} \widehat{x}_i &= x - x_i & i = 1, 2, 3, 4 \\ \widehat{y}_i &= y - y_i & i = 1, 2, 3, 4 \\ \widehat{x}_j &= x - x_j & j = 2, 3, 4, 1 \\ \widehat{y}_j &= y - y_j & j = 2, 3, 4, 1 \\ \widehat{x}_{ij} &= x_j - x_i & \binom{i}{j} = \binom{1, 2, 3, 4}{2, 3, 4, 1} \\ \widehat{y}_{ij} &= y_j - y_i & \binom{i}{j} = \binom{1, 2, 3, 4}{2, 3, 4, 1} \\ d_{ij} &= \sqrt{(x_j - x_i)^2 + (y_j - y_i)^2} & \binom{i}{j} = \binom{1, 2, 3, 4}{2, 3, 4, 1} \\ m_{ij} &= (y_j - y_i)/(x_j - x_i) & \binom{i}{j} = \binom{1, 2, 3, 4}{2, 3, 4, 1} \\ r_i &= \sqrt{(x - x_i)^2 + (y - y_i)^2 + z^2} & i = 1, 2, 3, 4 \\ e_i &= (x - x_i)^2 + z^2 & i = 1, 2, 3, 4 \\ h_i &= (x - x_i)(y - y_i) & i = 1, 2, 3, 4 \end{aligned} \quad (3.8)$$

Equations (3.5) and (3.6) show how the velocity components u and v are defined everywhere except on the quadrilateral boundary. For the component w , equation (3.7) shows that two limit cases exist when $z = 0$: one discontinuity when the point P lies on the quadrilateral

$$w(z = \pm 0) = \frac{\pm \sigma}{2} \quad (3.9)$$

and a null value when P is outside of the quadrilateral

$$w(z = \pm 0) = 0 \quad (3.10)$$

Figure 3.2 is based on the implementation of the equations 3.3, 3.5, 3.6, 3.7 and it shows the flow field induced by a quadrilateral source.

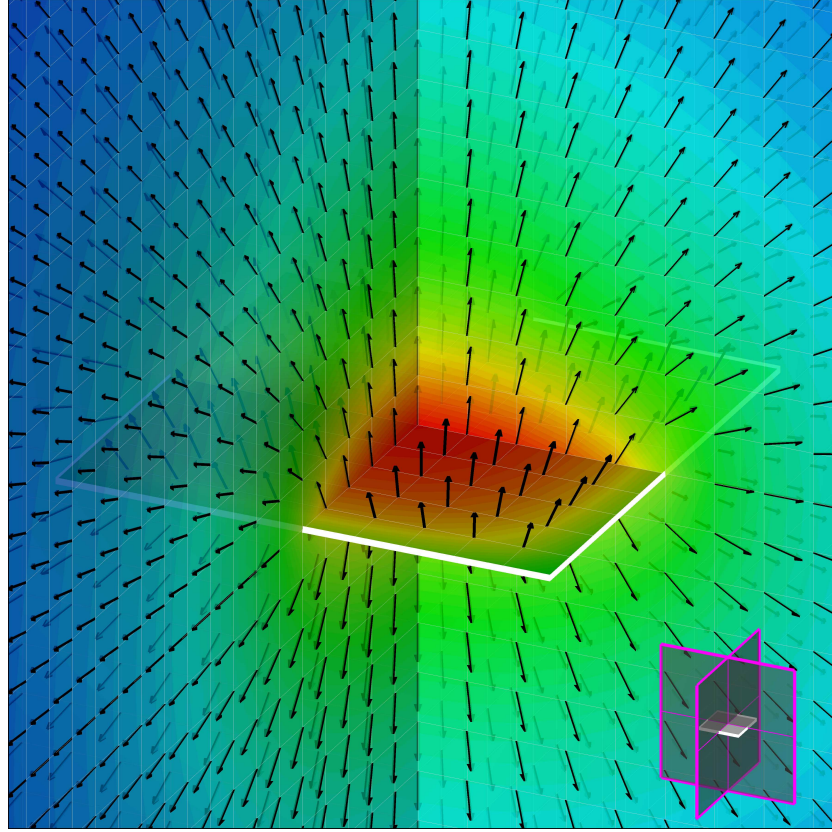


Figure 3.2: quadrilateral source - uniform velocity vector and isopotential contour.

3.1.2 Quadrilateral doublet

Consider a quadrilateral element with a constant-strength doublet distribution which points in the z direction, as showed in figure 3.3. Similar to the source element, the velocity potential may be obtained by integrating the point elements:

$$\phi(x, y, z) = -\frac{\mu}{4\pi} \int_S \frac{z \, dS}{[(x - x_0)^2 + (y - y_0)^2 + (z - z_0)^2]^{3/2}} \quad (3.11)$$

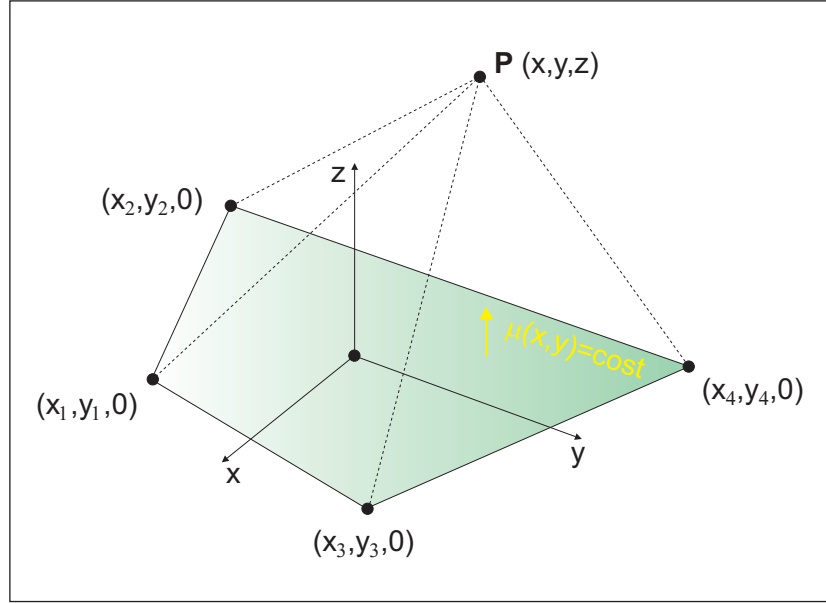


Figure 3.3: quadrilateral doublet element.

Following again the Hess and Smith procedure, one may obtain also this potential in function of the quadrilateral vertex coordinates:

$$\begin{aligned} \phi(x, y, z) = & \frac{\mu}{4\pi} \sum_{\substack{(i) \\ (j) = (1, 2, 3, 4) \\ (2, 3, 4, 1)}} \tan^{-1} \left(\frac{m_{ij}e_i - h_i}{zr_i} \right) + \\ & - \frac{\mu}{4\pi} \sum_{\substack{(i) \\ (j) = (1, 2, 3, 4) \\ (2, 3, 4, 1)}} \tan^{-1} \left(\frac{m_{ij}e_j - h_j}{zr_j} \right) \end{aligned} \quad (3.12)$$

and the corresponding velocity components:

$$u(x, y, z) = \frac{\mu}{4\pi} \sum_{\substack{(i) \\ (j) = (1, 2, 3, 4) \\ (2, 3, 4, 1)}} \frac{-z\hat{y}_{ij}(r_i + r_j)}{r_i r_j \{r_i r_j - [\hat{x}_i \hat{x}_j + \hat{y}_i \hat{y}_j + z^2]\}} \quad (3.13)$$

$$v(x, y, z) = \frac{\mu}{4\pi} \sum_{\substack{(i) \\ (j) = \begin{pmatrix} 1, 2, 3, 4 \\ 2, 3, 4, 1 \end{pmatrix}}} \frac{z\widehat{x}_{ij}(r_i + r_j)}{r_i r_j \{r_i r_j - [\widehat{x}_i \widehat{x}_j + \widehat{y}_i \widehat{y}_j + z^2]\}} \quad (3.14)$$

$$w(x, y, z) = \frac{\mu}{4\pi} \sum_{\substack{(i) \\ (j) = \begin{pmatrix} 1, 2, 3, 4 \\ 2, 3, 4, 1 \end{pmatrix}}} \frac{[\widehat{x}_j \widehat{y}_i - \widehat{x}_i \widehat{y}_j](r_i + r_j)}{r_i r_j \{r_i r_j - [\widehat{x}_i \widehat{x}_j + \widehat{y}_i \widehat{y}_j + z^2]\}} \quad (3.15)$$

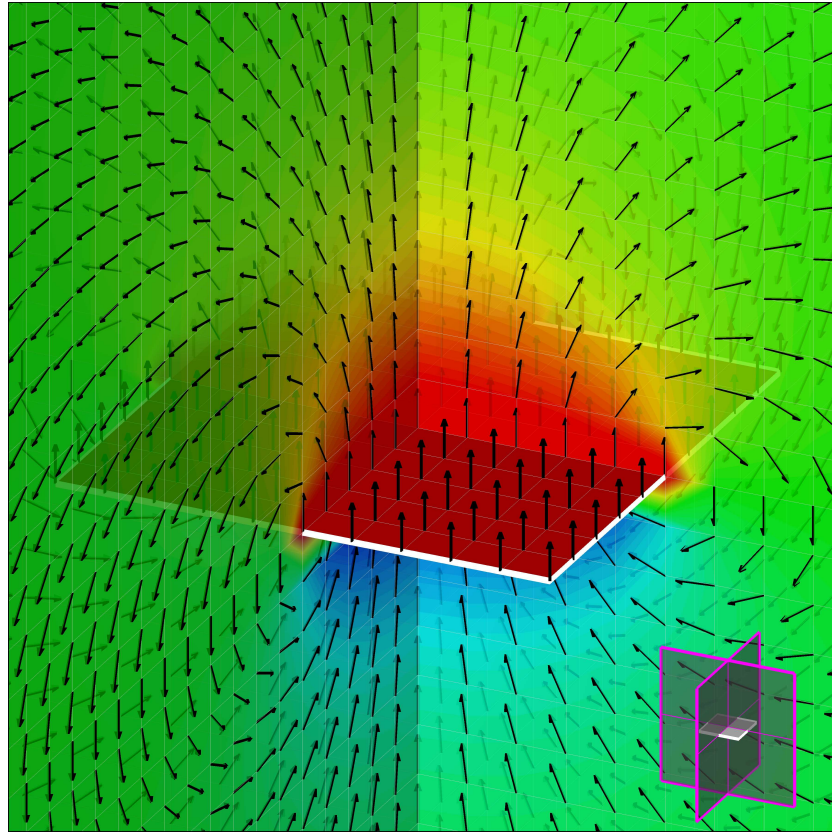


Figure 3.4: quadrilateral doublet - uniform velocity vector and isopotential contour.

Observe that the doublet potential may be developed from the source way because

$$\phi_{doublet} = -\frac{\partial}{\partial n} \phi_{source} \quad (3.16)$$

As the source element, equation (3.12) shows that there exists a discontinuity when $z = 0$:

$$\phi(z = \pm 0) = \frac{\pm\mu}{2} \quad (3.17)$$

Similar to the previous case, the potential and velocity fields illustrated in figure 3.4 are based on the implementation of the obtained equations.

3.1.3 Constant doublet panel equivalence to vortex ring

Continue to consider the quadrilateral doublet with constant strength μ with its potential which may be written as

$$\phi = -\frac{\mu}{4\pi} \int_S \frac{z}{r^3} dS \quad (3.18)$$

where $r = \sqrt{(x - x_0)^2 + (y - y_0)^2 + z^2}$.

The velocity is

$$\begin{aligned} \underline{U} &= \nabla\phi = -\frac{\mu}{4\pi} \int_S \nabla \frac{z}{r^3} dS = \\ &= \frac{\mu}{4\pi} \int_S \left[\mathbf{i} \frac{\partial}{\partial x_0} \frac{z}{r^3} + \mathbf{j} \frac{\partial}{\partial y_0} \frac{z}{r^3} + \mathbf{k} \left(\frac{1}{r^3} - \frac{3z}{r^5} \right) \right] dS \end{aligned} \quad (3.19)$$

where

$$\frac{\partial}{\partial x} \frac{1}{r^3} = -\frac{\partial}{\partial x_0} \frac{1}{r^3} \quad (3.20)$$

$$\frac{\partial}{\partial y} \frac{1}{r^3} = -\frac{\partial}{\partial y_0} \frac{1}{r^3} \quad (3.21)$$

Now, consider a vortex filament of circulation Γ along the curve bounding the quadrilateral, labeled as C (figure 3.5). Clearly, the velocity field induced by this filament is given by the Biot-Savart law (see chapter 1) as

$$\underline{U} = \frac{\Gamma}{4\pi} \int_C \frac{d\ell \times \underline{r}}{|\underline{r}|^3} \quad (3.22)$$

Thus, for $d\ell = (dx_0, dy_0)$ and $\underline{r} = (x - x_0, y - y_0, z)$, the velocity results expressed as following

$$\underline{U} = \int_C \left\{ \mathbf{i} \frac{z}{r^3} dy_0 - \mathbf{j} \frac{z}{r^3} dx_0 + \mathbf{k} [(y - y_0) dx_0 - (x - x_0) dy_0] \right\} \quad (3.23)$$

At this point, recall Stokes theorem for a vector \underline{A}

$$\int_C \underline{A} \cdot d\ell = \int_S \underline{n} \cdot \nabla \times \underline{A} dS \quad (3.24)$$

With $\underline{n} = \underline{k}$ above equation becomes

$$\int_C \underline{A} \cdot d\ell = \int_S \left(\frac{\partial A_y}{\partial x_0} - \frac{\partial A_x}{\partial y_0} \right) dS \quad (3.25)$$

Applying Stokes theorem on the above velocity integral, one gets

$$\underline{U} = \frac{\Gamma}{4\pi} \int_S \left[\mathbf{i} \frac{\partial}{\partial x_0} \frac{z}{r^3} + \mathbf{j} \frac{\partial}{\partial y_0} \frac{z}{r^3} - \mathbf{k} \left(\frac{\partial}{\partial x_0} \frac{x - x_0}{r^3} + \frac{\partial}{\partial y_0} \frac{y - y_0}{r^3} \right) \right] dS \quad (3.26)$$

Therefore, if $\Gamma = \mu$ the velocity field induced by the vortex ring is identical to the velocity of the doublet quadrilateral (see also figure 3.4).

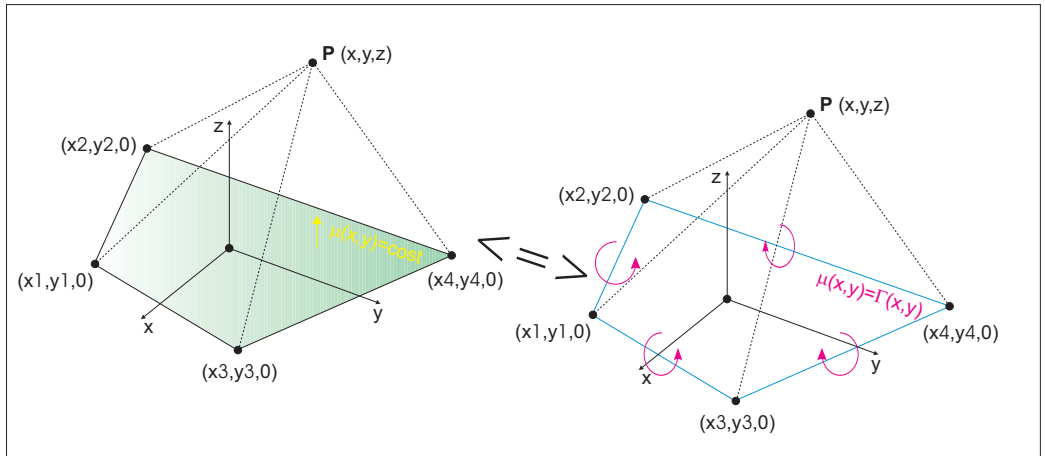


Figure 3.5: quadrilateral doublet element and its vortex ring equivalent.

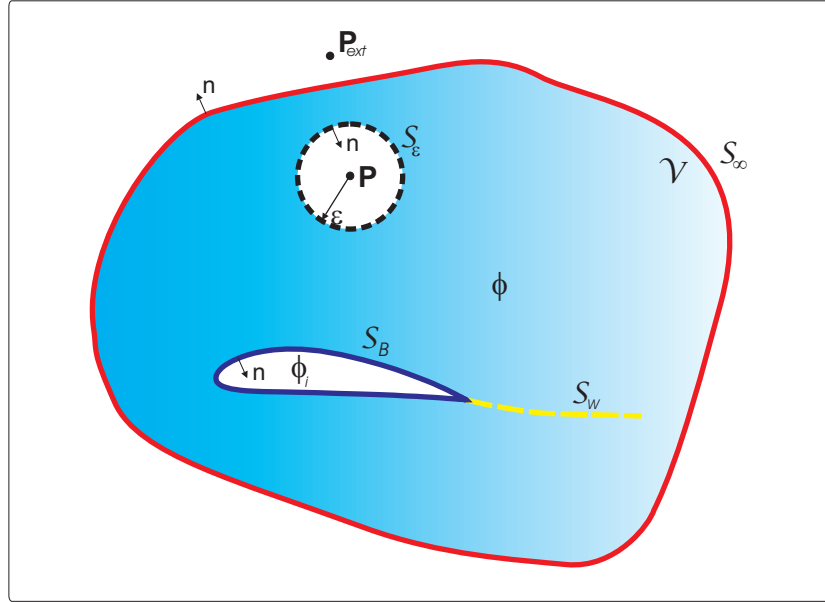


Figure 3.6: the fluid domain considered in the derivation of the Green's Theorem BIE.

3.2 Panel method formulation

For most engineering applications the problem requires a solution in a fluid domain. Usually this domain contains a solid body with additional boundaries that may define an outer flow boundary.

Consider the scalar potential governed by Laplace's equation:

$$\nabla^2 \phi = 0. \tag{3.27}$$

The mathematical problem defined by Laplace's equation with the boundary conditions is described schematically by figure 3.6. Laplace's equation must be solved for an arbitrary body with boundary S_B enclosed in a volume V , with the outer boundary S_∞ (with the normal defined so that it always points outside the region of interest V) [12][33][23][40][29].

Inside the domain V the general solution of Laplace's equation is possible to obtain by means of the Green's Identity that follows from the divergence

theorem that is

$$\int \int_S \underline{Q} \cdot \underline{n} dS = \int \int \int_V \underline{\nabla} \cdot \underline{Q} dV \quad (3.28)$$

Particularly, consider the vector

$$\underline{Q} = \phi_1 \underline{\nabla} \phi_2 - \phi_2 \underline{\nabla} \phi_1 \quad (3.29)$$

where ϕ_1 and ϕ_2 are two scalar functions of position. Applying the divergence theorem to the vector \underline{Q} , results:

$$\int \int_S (\phi_1 \underline{\nabla} \phi_2 - \phi_2 \underline{\nabla} \phi_1) \cdot \underline{n} dS = \int \int \int_V (\phi_1 \nabla^2 \phi_2 - \phi_2 \nabla^2 \phi_1) dV \quad (3.30)$$

This equation is the second of Green's Identities where the surface integral is taken over all the boundaries S , including a wake sheet model S_W (necessary to impose the Kutta condition) and the outer boundary S_∞ :

$$S = S_B + S_W + S_\infty \quad (3.31)$$

Let one set

$$\phi_1 = \frac{1}{r} \quad (3.32)$$

and

$$\phi_2 = \phi \quad (3.33)$$

where ϕ is the potential of the flow in V , and r is the distance from a point $P(x, y, z)$ is another potential that satisfies Laplace's equation.

This way the second Green's Identity results:

$$\int \int_S \left(\frac{1}{r} \underline{\nabla} \phi - \phi \underline{\nabla} \frac{1}{r} \right) \cdot \underline{n} dS = \int \int \int_V \left(\frac{1}{r} \nabla^2 \phi - \phi \nabla^2 \frac{1}{r} \right) dV \quad (3.34)$$

When the point P is outside of V , equation (3.34) becomes

$$P \notin V \implies \int \int_S \left(\frac{1}{r} \underline{\nabla} \phi - \phi \underline{\nabla} \frac{1}{r} \right) \cdot \underline{n} dS = 0 \quad (3.35)$$

In the particular case where the point P is inside the region, the point P must be excluded from the region of integration and it is surrounded by a small sphere of radius ϵ . In the remaining region V outside of the sphere ϵ both ϕ_1 and ϕ_2 satisfy Laplace's equation. Therefore, equation (3.34) becomes

$$P \in V \implies \int \int_{S+S_\epsilon} \left(\frac{1}{r} \nabla \phi - \phi \nabla \frac{1}{r} \right) \cdot \underline{n} dS = 0 \quad (3.36)$$

Now introduce a spherical coordinate system at P to obtain the integral over the sphere. Since the vector \underline{n} points inside the small sphere, equation (3.36) becomes

$$\int \int_S \left(\frac{1}{r} \nabla \phi - \phi \nabla \frac{1}{r} \right) \cdot \underline{n} dS - \int \int_{S_\epsilon} \left(\frac{1}{r} \frac{\partial \phi}{\partial r} + \frac{\phi}{r^2} \right) dS = 0 \quad (3.37)$$

The integration over the surface of the spherical exclusion region reduces to:

$$\int \int_{S_\epsilon} \left(\frac{\phi}{r^2} \right) dS = 4\pi \phi(P) \quad (3.38)$$

Finally, equation (3.37) becomes

$$\phi(P) = \frac{1}{4\pi} \int \int_S \left(\frac{1}{r} \nabla \phi - \phi \nabla \frac{1}{r} \right) \cdot \underline{n} dS \quad (3.39)$$

Equation (3.39) is the third Green's Identity that gives the value of the $\phi(P)$ at any point in the flow, within the region V , in terms of the values of the ϕ and $\partial\phi/\partial n$ on the boundaries S .

When the flow of interest occurs inside the boundary of the S_B and hence the resulting *internal potential* is ϕ_i , the point P inside the region V is outside of S_B and applying equation (3.35), results

$$0 = \frac{1}{4\pi} \int \int_{S_B} \left(\frac{1}{r} \nabla \phi_i - \phi_i \nabla \frac{1}{r} \right) \cdot \underline{n} dS \quad (3.40)$$

where \underline{n} points out from S_B .

By adding equations (3.39) and (3.40), we obtain the formula that includes the influence of the inner potential:

$$\begin{aligned} \phi(P) = & \frac{1}{4\pi} \iint_{S_B} \left[\frac{1}{r} \nabla(\phi - \phi_i) - (\phi - \phi_i) \nabla \frac{1}{r} \right] \cdot \underline{n} dS + \\ & + \frac{1}{4\pi} \iint_{S_W + S_\infty} \left(\frac{1}{r} \nabla \phi - \phi \nabla \frac{1}{r} \right) \cdot \underline{n} dS \end{aligned} \quad (3.41)$$

Regarding the contribution of the S_∞ integral in equation (3.41), this can be defined as

$$\phi_\infty(P) = \frac{1}{4\pi} \iint_{S_\infty} \left(\frac{1}{r} \nabla \phi - \phi \nabla \frac{1}{r} \right) \cdot \underline{n} dS \quad (3.42)$$

This contribution depends on the reference frame: for example, this potential can be selected as a constant in the region in an inertial system where the body moves through an otherwise stationary fluid. Furthermore, since the wake surface is assumed to be thin, $\partial\phi/\partial n$ is continuous across it. By means of these assumptions, equation (3.41) becomes

$$\begin{aligned} \phi(P) = & \phi_\infty(P) + \frac{1}{4\pi} \iint_{S_B} \left[\frac{1}{r} \nabla(\phi - \phi_i) - (\phi - \phi_i) \nabla \frac{1}{r} \right] \cdot \underline{n} dS + \\ & - \frac{1}{4\pi} \iint_{S_W} (\phi_U - \phi_L) \underline{n} \cdot \nabla \frac{1}{r} dS \end{aligned} \quad (3.43)$$

This formula provides the value of $\phi(P)$ in terms of ϕ and $\partial\phi/\partial n$ on the boundaries. One can observe that the flow problem reduces to determining the value of ϕ and $\partial\phi/\partial n$ on the boundaries.

When the point P lies on the boundary S_B , the potential $\phi(P)$ becomes singular. Therefore, in order to exclude the point from V , the integration is carried out only around the surrounding hemisphere. Equation (3.43)

becomes

$$\begin{aligned}
 \phi(P \in S_b) = & \phi_\infty(P) + \frac{1}{4\pi} \iint_{S_B} \frac{1}{r} \underline{n} \cdot \underline{\nabla}(\phi - \phi_i) dS + \\
 & - \frac{1}{4\pi} \iint_{S_{B-P}} (\phi - \phi_i) \underline{n} \cdot \underline{\nabla} \frac{1}{r} dS \pm \frac{1}{2} (\phi - \phi_i)_P + \\
 & - \frac{1}{4\pi} \iint_{S_W} (\phi_U - \phi_L) \underline{n} \cdot \underline{\nabla} \frac{1}{r} dS
 \end{aligned} \tag{3.44}$$

where the factor 1/2 is due to the use of the hemisphere instead of the sphere, and the sign is due to the direction of \underline{n} .

The solution of the above relationship let us evaluate the potential in any point P that lies on the boundary S_B , in terms of ϕ and $\partial\phi/\partial n$ on the boundaries.

3.2.1 Boundary conditions

The solution of equation (3.44) must satisfy a number of known boundary conditions which can be imposed on the solid surfaces and the fluctuating wake. Particularly, the Neumann condition must be satisfied on the surface S_B so:

$$\underline{n} \cdot \underline{\nabla} \phi = -U_{n_T} - U_{n_R} \tag{3.45}$$

where U_{n_R} is the resultant normal component of velocity relative to the surface due to the motion of the body, and U_{n_T} is the normal component of the velocity due to possible flows of transpiration through the surface, therefore this term is zero for the case of a solid boundary with no transpiration.

Instead, no condition in terms of potential results a necessity on the surface S_W , because it itself represents the imposition of the wing trailing

edge Kutta condition. The rise in potential lies must assure that the velocity does not rotate round the trailing edge. This way the presence of the wake does not introduce additional unknowns to the problem, because the rise in potential on the wake is associated to the unknown potentials near the trailing edge and the contribution of the S_W integral must be considered as a known term.

However, a constraint exists for the wake, due to the wake form. This form must be determined considering that the wake cannot support a load, because the wake is not a solid surface. Therefore, the wake form must be aligned with the local flow direction, which means to establish a condition of tangency of the velocity in every point:

$$\underline{U} \cdot \underline{n}|_{S_W} = 0 \quad (3.46)$$

Note that it is necessary to know the flow field \underline{U} but the goal of the analysis is \underline{U} . This non-linearity can be overpassed to approach the wake with a fixed form, independent of the flow field, or with the support of solution iterative techniques.

3.2.2 Singularity model

A given flow field can be obtained from an infinite number of configurations of distributions of singularities (sources and doublets) on the problem boundaries (S_B , S_W), each combination producing a different flow in the inside region.

A unique combination of singularities can be obtained with different singularity models. Particularly, one way that can be considered is to specify one of the singularity distributions and to solve for other using boundary conditions only on the side of the boundary. Another way is to apply certain

constraining relationships on the singularity distributions.

One important characteristic for certain of the singularity models from the numerical point of view, is that the flow field generated in the inner region by the model is related to the boundary [40]. Particularly, the jump from the internal flow to the external flow should be a small passing through the boundary. Therefore, a minimum perturbation from the singularities is required. To satisfy this requisite one can treat the internal flow directly in equation (3.44), obtaining a unique singularity distribution by specifying boundary conditions on both sides of the surface. In this case, the inner velocity potential ϕ_i is specified directly in equation (3.44): this is an internal Dirichlet boundary condition. Particularly, consider the internal flow equal to outlet flow $\phi_i = \phi_\infty$. This way, equation (3.44) becomes:

$$\begin{aligned}
 0 = & \frac{1}{4\pi} \iint_{S_B} \frac{1}{r} \underline{n} \cdot \underline{\nabla}(\phi - \phi_\infty) dS + \\
 & - \frac{1}{4\pi} \iint_{S_{B-P}} (\phi - \phi_\infty) \underline{n} \cdot \underline{\nabla} \frac{1}{r} dS + \frac{1}{2}(\phi - \phi_\infty)_p + \\
 & - \frac{1}{4\pi} \iint_{S_w} (\phi_U - \phi_L) \underline{n} \cdot \underline{\nabla} \frac{1}{r} dS
 \end{aligned} \tag{3.47}$$

where the perturbation potential on the exterior surface $\phi - \phi_\infty$, is now the doublet density

$$4\pi\mu = \phi - \phi_\infty \tag{3.48}$$

whereas the source distribution is

$$4\pi\sigma = -\underline{n} \cdot (\underline{\nabla}\phi - \underline{\nabla}\phi_\infty) = -U_n + U_{n_\infty} \tag{3.49}$$

Note that the source distribution is therefore established at the outlet.

At this point, equation (3.47) becomes

$$\int_{S_B} \int \frac{\sigma}{r} dS - \int_{S_{B-P}} \int \mu \underline{n} \cdot \underline{\nabla} \frac{1}{r} dS + 2\pi\mu_p - \int_{S_W} \int \mu^w \underline{n} \cdot \underline{\nabla} \frac{1}{r} dS = 0 \quad (3.50)$$

where $\mu^w = (\phi_U - \phi_L)/4\pi$ is the known wake doublet density at the trailing edge.

Moreover, note that sources and doublets have a physical sense. The thickness effects can be simulated by means of the doublets, the non symmetrical conditions by means of the sources.

Equation (3.49) shows that the Neumann condition can be satisfied only by the sources and the sources are known too.

So far thick configurations having a distinct internal volume enclosed by the surface S have been concerned. When the configurations having a indistinct internal volume (parts of the configuration are extremely thin), then these configurations can be represented by open surfaces. In this case, equation (3.43) becomes

$$\begin{aligned} \phi(P) = \phi_\infty(P) &+ \frac{1}{4\pi} \int_{S_B} \int \left(\frac{1}{r} \underline{\nabla}(\phi_U - \phi_L) - (\phi_U - \phi_L) \underline{\nabla} \frac{1}{r} \right) \cdot \underline{n} dS + \\ &- \frac{1}{4\pi} \int_{S_W} \int \mu^w \underline{n} \cdot \underline{\nabla} \frac{1}{r} dS \end{aligned} \quad (3.51)$$

If the normal velocity is continuous through the sheet then the term $\underline{n} \cdot (\underline{\nabla}\phi_U - \underline{\nabla}\phi_L) = 0$, disappearing the source term and the above relationship becomes:

$$\phi(P) = \phi_\infty(P) - \int_{S_B} \int \mu \underline{n} \cdot \underline{\nabla} \frac{1}{r} dS - \int_{S_W} \int \mu^w \underline{n} \cdot \underline{\nabla} \frac{1}{r} dS \quad (3.52)$$

where $\mu = (\phi_U - \phi_L)/4\pi$ is the jump in total potential across the sheet.

Applying the external Neumann boundary condition, then

$$\underline{n} \cdot \underline{\nabla}\phi(P) = \underline{n} \cdot \underline{\nabla}\phi_\infty(P) - \int_{S_B} \int \mu \underline{n} \cdot \underline{\nabla} \left(\underline{n} \cdot \underline{\nabla} \frac{1}{r} \right) dS +$$

$$- \iint_{S_W} \mu^w \underline{n} \cdot \underline{\nabla} \left(\underline{n} \cdot \underline{\nabla} \frac{1}{r} \right) dS \quad (3.53)$$

where $\underline{n} \cdot \underline{\nabla} \phi(P) = 0$ in case of no transpiration.

Equations (3.50) and (3.53) are the basic equations for the solution of the flow problem. These equation can be written so:

$$\phi(P) = \phi_\infty(P) + \phi'(P) \quad (3.54)$$

$$\underline{n} \cdot \underline{\nabla} \phi(P) = \underline{n} \cdot \underline{\nabla} \phi_\infty(P) + \underline{n} \cdot \underline{\nabla} \phi'(P) \quad (3.55)$$

where ϕ' represents the potential of perturbation.

By means of the resolution of these equations the unknown singularity distributions may be obtained on the body surface and that content to compute the flow field by means of the derivation of the potential.

3.2.3 Computation of velocities and forces

Once the singularity distribution strengths are known, the total velocity in every point of the domain is possible to compute by means of the following equation

$$\begin{aligned} \underline{U}(P) = \underline{U}_\infty(P) - \iint_{S_B} \mu \underline{\nabla} \left(\underline{n} \cdot \underline{\nabla} \frac{1}{r} \right) dS + \\ + \iint_{S_B} \sigma \underline{\nabla} \frac{1}{r} dS - \iint_{S_W} \mu^w \underline{\nabla} \left(\underline{n} \cdot \underline{\nabla} \frac{1}{r} \right) dS \end{aligned} \quad (3.56)$$

The above relationship is the basic for many numerical solutions and has been obtained by taking the gradient of total scalar potential of equation (3.43).

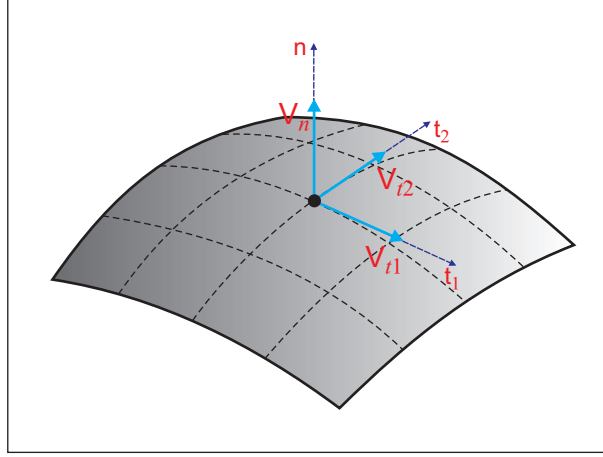


Figure 3.7: panel local reference frame for evaluating the normal and tangential velocity components.

Instead, when the point P lies on the boundary, it is necessary to consider equation (3.44) and to use following equation

$$\begin{aligned} \underline{U}(P \in body) = & \underline{U}_\infty(P) - 2 \iint_{S_{B-P}} \mu \nabla \left(\underline{n} \cdot \nabla \frac{1}{r} \right) dS + \\ & + 2 \iint_{S_B} \sigma \nabla \frac{1}{r} dS - 2 \iint_{S_W} \mu^w \nabla \left(\underline{n} \cdot \nabla \frac{1}{r} \right) dS \end{aligned} \quad (3.57)$$

However, as the particular choice of the source values, it is possible to compute the velocity by taking the gradient of the potential in a local reference frame centered in the point of interest, how showed in figure 3.7.

In fact, as the normal component of velocity disturbance has been established, one may compute the tangential components of the same velocity disturbance by means of the derivatives of the doublet intensity along two direction tangential to the body:

$$\underline{u}(P) = u_{t_1} \mathbf{i}_{t_1} + u_{t_2} \mathbf{i}_{t_2} + u_n \mathbf{i}_n = \frac{\partial \mu}{\partial t_1} \mathbf{i}_{t_1} + \frac{\partial \mu}{\partial t_2} \mathbf{i}_{t_2} - \sigma \mathbf{i}_n \quad (3.58)$$

In the case of a Neumann boundary condition, above equation becomes:

$$\underline{u}(P) = \pm \frac{\partial \mu/2}{\partial t_1} \mathbf{i}_{t_1} \pm \frac{\partial \mu/2}{\partial t_2} \mathbf{i}_{t_2} - \underline{U}_\infty \cdot \mathbf{i}_n \quad (3.59)$$

where the signs $+/-$ represent the upper and lower sides, respectively. These components will be summed at the no-disturbed local velocity in order to obtain the total velocity:

$$\underline{U}(P \in \text{body}) = \underline{U}_\infty(P) + \underline{u}(P) \quad (3.60)$$

After the distributions of velocity and $\partial\phi/\partial t$ have been computed on the bodies, by means of Bernoulli theorem, one may obtain the corresponding distributions of pressure to integrate in order to compute forces and moments.

3.3 Panel method numerical procedure

In the above section, the solution to the potential flow problem has been obtained analytically, only after some geometrical simplifications in the boundary conditions have been made.

In most of the cases, the numerical application is characterized by the treatment of more realistic geometries and the fulfillment of the boundary conditions on the corresponding surface. In this section, the numerical procedure will be examined.

The numerical method to solve the potential flow problem is based on the surface distribution of singularity elements, as the solution has been reduced to finding the strength of these elements.

From the numerical point of view, a solution can be obtained if the body and wake geometries are discretized separately from singularity distribution [29]. In most of applications, the body and wake surfaces are represented by a large number of small quadrilateral and/or triangular regions which are planar in most methods. These small quadrilateral regions are called panels defined by functions of the kind $z = f(x, y)$ in a local reference frame (see

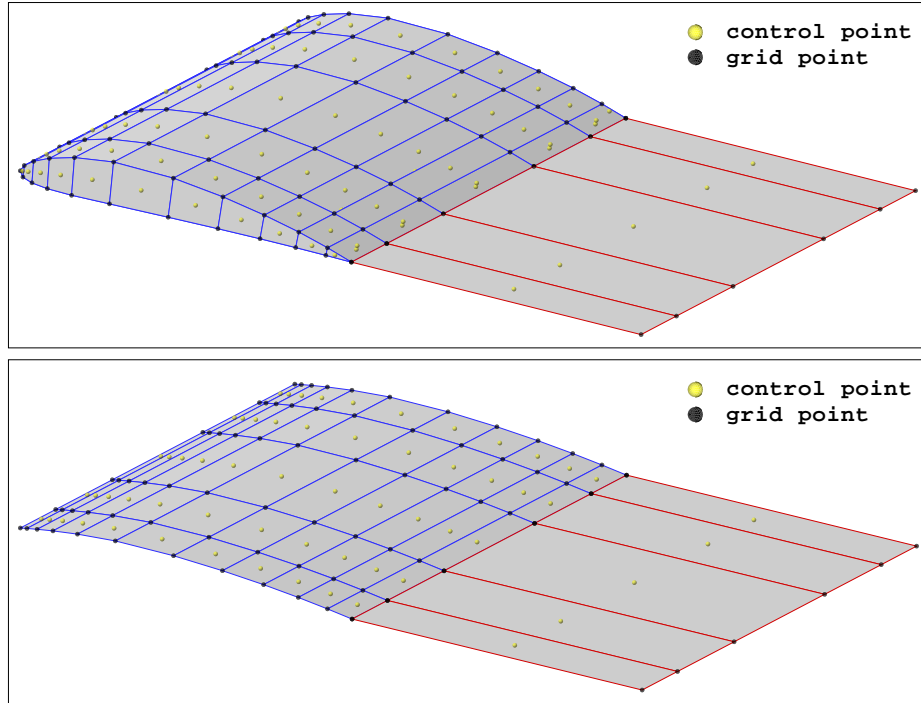


Figure 3.8: examples of discretized (thick and thin) body and wake geometries.

figure 3.8); therefore this type of method is called panel method. Thus, as the body is divided into N surface panels, so the wake is represented by N_w wake panels. Every single panel is characterized by means of its grid points.

By means of the discretization process, panels are defined by polynomials on which the order of desired accuracy to represent the real geometry depends. This accuracy rises with the polynomial order.

The singularity distribution must be subdivided into panels which are coinciding with the body panels where the singularity strength may be assumed constant (low-order), linearly variable (first order) or parabolic (second order). Generally, the order of accuracy used for the singularity distribution is equal to the order of the body discretization, since the schematization accuracy of lower order should be, however, decisive.

For the singularities, the simplest discretization is the constant strength over quadrilateral panel, defined by plane surfaces and rectilinear borders. This way to discretize permits to have notable simplicity of calculus and of numerical implementation but requires a great number of panels in order to compensate the accuracy loss due to low polynomial order. However, this choice results the most used technique of panels methods.

Once the body and wake surfaces have been discretized, the control point in which the boundary condition must be imposed results automatically individuated into the centroid of each panel. For thick bodies, the condition of zero normal flow or assigned normal flow across the body surfaces may be defined by using Dirichlet formulation (3.50). For thin bodies, this condition may be defined by using Neumann formulation (3.53), as seen in previous section. Thus, equations (3.50) and (3.53) may be rewritten in each control point of N_B panels (of which N_B^d of Dirichlet type and N_B^n of Neumann type) present on the surfaces. Particularly, let J , r_J and N_w be the panel in which the boundary condition is imposed on the control point (see figure 3.9), the distance respect to the panel of which the effect is computed and the wake panel number, respectively, results

$$\begin{aligned} & \sum_{K=1}^{N_B} \iint_{\text{panel } K} \mu_K \underline{n} \cdot \underline{\nabla} \frac{1}{r_J} dS + \sum_{L=1}^{N_w} \iint_{\text{panel } L} \mu_L^w \underline{n} \cdot \underline{\nabla} \frac{1}{r_J} dS = \\ & = \sum_{K=1}^{N_B} \iint_{\text{panel } K} \sigma_K \frac{1}{r_J} dS \quad (J=1, \dots, N_B^d) \end{aligned} \quad (3.61)$$

$$\begin{aligned} & \sum_{K=1}^{N_B} \underline{n}_J \cdot \iint_{\text{panel } K} \mu_K \underline{\nabla} \left(\underline{n} \cdot \underline{\nabla} \frac{1}{r_J} \right) dS + \sum_{L=1}^{N_w} \underline{n}_J \cdot \iint_{\text{panel } L} \mu_L^w \underline{\nabla} \left(\underline{n} \cdot \underline{\nabla} \frac{1}{r_J} \right) dS = \\ & = \sum_{K=1}^{N_B} \underline{n}_J \cdot \iint_{\text{panel } K} \sigma_K \underline{\nabla} \frac{1}{r_J} dS - \underline{n}_J \cdot (\underline{U} - \underline{U}_\infty) \quad (J=1, \dots, N_B^n) \end{aligned} \quad (3.62)$$

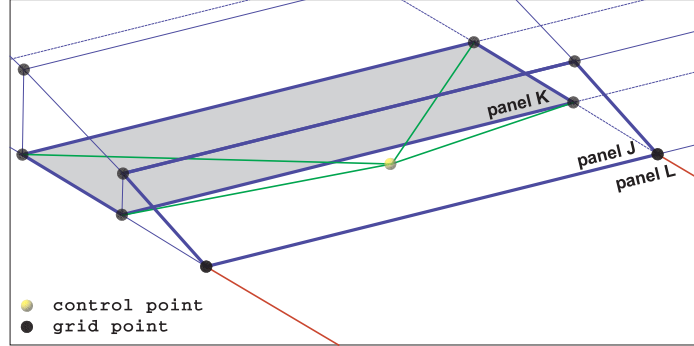


Figure 3.9: schematization for the influence coefficients.

The integrals in the above equations are over the single panel surface, and each one represents the influence that the generic panel K or L produces on the control point of the panel J . Moreover, these integrals may be substituted by summations extended to the corresponding grid points. For the elements with constant or unitary singularity strength, this influence is due only to the panel geometry and it may be synthesized using some coefficients, called influence coefficients:

$$B_{JK}^d = \iint_{\text{panel } K} \frac{1}{r_J} dS \quad (3.63)$$

$$B_{JK}^n = \underline{n}_J \cdot \underline{U}_{JK}^\sigma \quad ; \quad \underline{U}_{JK}^\sigma \iint_{\text{panel } K} \underline{\nabla} \frac{1}{r_J} dS \quad (3.64)$$

$$C_{JK}^d = \iint_{\text{panel } K} \underline{\nabla} \frac{1}{r_J} dS \quad ; \quad C_{JJ}^d = -2\pi \quad (3.65)$$

$$C_{JK}^n = \underline{n}_J \cdot \underline{U}_{JK}^\mu \quad ; \quad \underline{U}_{JK}^\mu \iint_{\text{panel } K} \underline{\nabla} \left(\underline{n} \cdot \frac{1}{r_J} \right) dS \quad (3.66)$$

where the apexes d and n are always indicative of the imposed condition type.

By using the influence coefficients, equations (3.61) and (3.62) become

$$\sum_{K=1}^{N_B} C_{JK}^d \mu_K + \sum_{K=1}^{N_W} C_{JK}^d \mu_L^w = \sum_{K=1}^{N_B} B_{JK}^d \sigma_K \quad (J = 1, \dots, N_B^d) \quad (3.67)$$

$$\sum_{K=1}^{N_B} C_{JK}^n \mu_K + \sum_{K=1}^{N_W} C_{JK}^n \mu_L^w = \sum_{K=1}^{N_B} B_{JK}^n \sigma_K - \underline{n}_J \cdot (\underline{U} - \underline{U}_\infty)_J \quad (J = 1, \dots, N_B^n) \quad (3.68)$$

When the source strengths related to the condition of zero normal flow across the body surfaces (equation (3.49)) are assigned for thick bodies or fixed equal to zero for thin body, it is possible to compute the influence coefficients B_{JK}^d e B_{JK}^n , letting unknown only the doublet terms. Moreover, the Kutta condition permits to rewrite also the wake doublets μ_L^w in function of the body doublets μ_K . In fact, for thick body, every single wake panel will have one side coinciding with the trailing edge of the body on which two panels (one upper panel, one lower panel) of the same body converge.

Let μ_L^u , μ_L^l , μ_L^w be the doublet strength of the upper panel, the doublet strength of the lower panel, and the doublet strength of the near wake panel (see figure 3.10), by the Kutta condition results

$$\mu_L^w = \mu_L^u - \mu_L^l \quad (3.69)$$

As for the bodies without thickness (figure 3.10), there is not difference between upper and lower, therefore

$$\mu_L^w = \mu_L^l \quad (3.70)$$

Thus, the influence of any panel wake becomes:

$$C_{JK}^d \mu_L^w = C_{JK}^d (\mu_L^u - \mu_L^l) \quad (3.71)$$

$$C_{JK}^n \mu_L^w = C_{JK}^n \mu_L^l \quad (3.72)$$

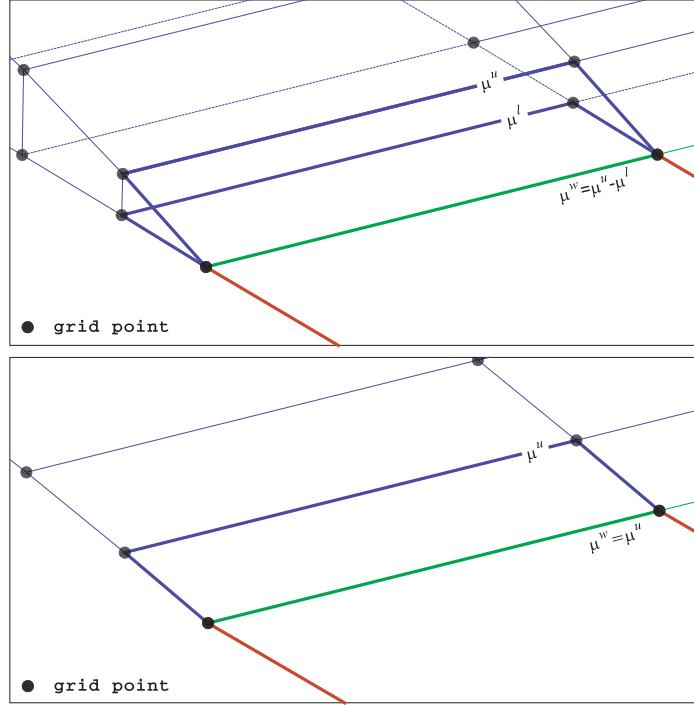


Figure 3.10: reference frame for the Kutta condition.

Equations (3.71) and (3.72) consent to trace the doublet influence of the doublets on the wake panels back to the corresponding doublets near the trailing edge, correcting simply the influence coefficients C_{JK}^d and C_{JK}^n , thus

$$A_{JK}^d = C_{JK}^d \quad \text{panel } K \text{ not at the trailing edge} \quad (3.73)$$

$$A_{JK}^d = C_{JK}^d - C_{JL}^d \quad \text{panel } K \text{ at the upper trailing edge} \quad (3.74)$$

$$A_{JK}^d = C_{JK}^d + C_{JL}^d \quad \text{panel } K \text{ at the lower trailing edge} \quad (3.75)$$

$$A_{JK}^n = C_{JK}^n \quad \text{panel } K \text{ not at the trailing edge} \quad (3.76)$$

$$A_{JK}^n = C_{JK}^n + C_{JL}^n \quad \text{panel } K \text{ at the trailing edge} \quad (3.77)$$

Finally, one obtains:

$$\sum_{K=1}^{N_B} A_{JK}^d \mu_k = \sum_{K=1}^{N_B} B_{JK}^d \sigma_K \quad (J = 1, \dots, N_B^d) \quad (3.78)$$

$$\sum_{K=1}^{N_B} A_{JK}^n \mu_k = \sum_{K=1}^{N_B} B_{JK}^n \sigma_K - \underline{n}_J \cdot (\underline{U} - \underline{U}_\infty)_J \quad (J = 1, \dots, N_B^n) \quad (3.79)$$

Another condition of the wake form must be added to equations (3.78) and (3.79). This is a no-linear problem since this condition corresponds to the imposition of a variation of the wake form which fluctuates freely in the domain [13]. In the case of flexible wake, this condition may be imposed by annulling the normal velocity components in the control points of every single wake panel:

$$\underline{U} \cdot \underline{n}_L = 0 \quad (L = 1, \dots, N_W) \quad (3.80)$$

Equations (3.78) and (3.79) for the N_B control point drive to a set of N_B linear algebraic equations in the N_B strength unknown of surface doublets μ_K .

The numerical solution of this set is generally stable, because the unknown doublet distribution is quite little, since it is due to only perturbation potential.

3.3.1 Unsteady panel methods

The method of solution of incompressible, irrotational flow that is developed so far does not include the unsteady nature of the problem. Therefore, it will be shown that this method may include time-dependency that will be introduced through the boundary conditions and the use of the unsteady Bernoulli equation.

The choice of the coordinate systems is very important for the formulation of the unsteady problem. In order to prescribe correctly the boundary conditions on the solid body surfaces, consider a body-fixed coordinate system $(0, x, y, z)$ and a fixed-in-space global reference frame $(0, X, Y, Z)$ which

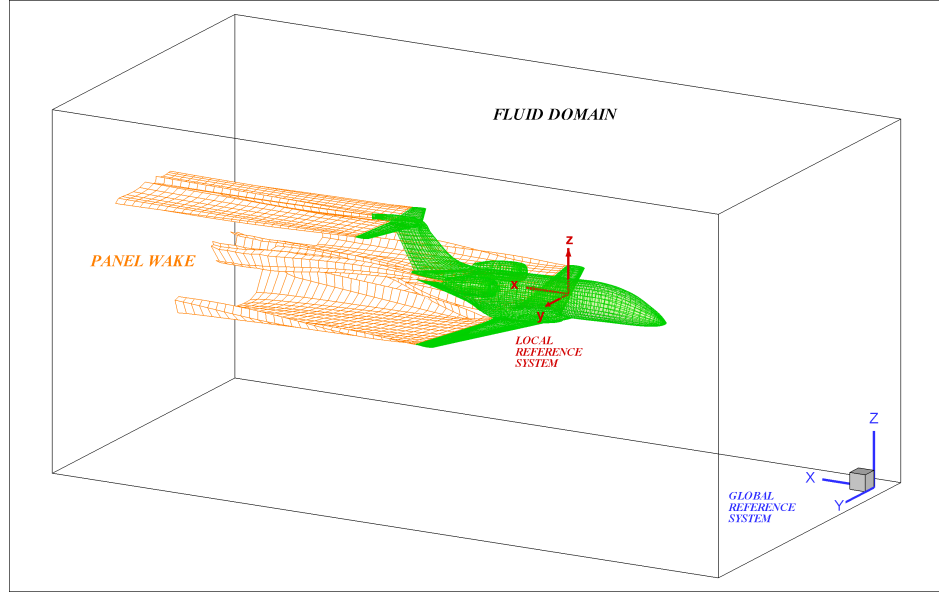


Figure 3.11: inertial frame and body frame used to describe the motion of the body.

is assumed to be known, as illustrated in figure 3.11. Suppose the body motion law is known, the zero normal flow boundary condition becomes:

$$\frac{\partial \phi}{\partial n} = (\underline{U}_\infty - \underline{U}_r - \underline{\Omega} \times \underline{r}) \cdot \underline{n} \quad (3.81)$$

where $\underline{r} = \underline{r}(x, y, z)$, \underline{U}_∞ , \underline{U}_r and $\underline{\Omega}$ are the position of any point in the body reference frame, the velocity of the body frame origin in global coordinates, the relative motion of the surface due to deformation of the body, the angular velocity, respectively.

3.3.2 Unsteady panel wake model

Regarding the wake, the solution is based on a time-stepping technique: the wake is formed in the inertial coordinate system as the body from which the wake separates moves away from its initial position, shedding from known separation lines on the surface body (trailing edges of wings, for example).

During every single time step, the wing moves along its flight path and every trailing edge vortex panel sheds a wake panel with a strength (related to the Kutta condition) corresponding to its circulation in the previous time step. It is as if the trailing edge leaves its "tracks" during its pass or, if the body is motionless and surrounded by the stream, the trailing edge is trailed by the flow [12] (see figure 3.12). So a new row of wake panels is added to the wake at the separation line and all the preexisting rows of wake panels are convected downstream with the local velocity field in the inertial reference frame at each time step [7][8][6][11].

In detail, at the beginning of the motion no wake panels exist but only the wing bound vortex panels exist where the closing segment of the trailing edge vortex elements represents the starting vortex or separation line.

During the second time step, the wing is moved along its flight path and each trailing edge vortex panel sheds a wake panel. This first wake sheet, used to account for the vorticity recently shed into the domain from the wing trailing edge, imposes a well defined potential jump at the trailing edge to satisfy the Kutta condition: this condition is used as a boundary condition to determine the strength of the doublets to be shed into the first row of a wake. Therefore, every single wake panel has a vortex strength equal to the circulation obtained by fulfilling the Kutta condition at the trailing edge. Once the trailing edge vortexes are given, the buffer wake sheet is determined automatically.

During the third time step, two rows of wake panel exist: new fist row of wake panels closest to the trailing edge where the Kutta condition must be imposed is shed by previous time-step trailing edge vortex panel, second row is known since corresponds to the convected previous time-step wake panel row where the Kutta condition was resolved. Therefore, at the rising of time

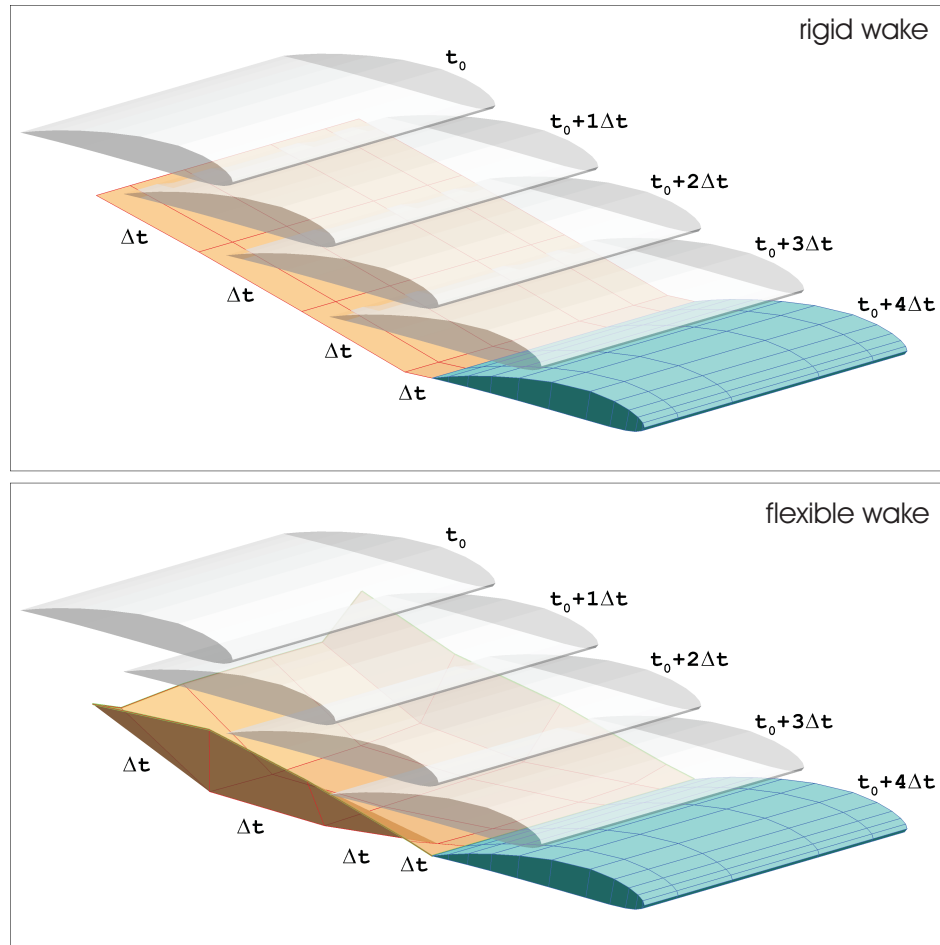


Figure 3.12: examples of generation of rigid and flexible unsteady wake.

the rows successive to the wake panel row, closest to the trailing edge are known.

This time stepping methodology may be continued at every single time step in which vortex wake is moved by the local velocity. Thus, unsteady phenomenon like wake rollup may be simulated.

At this point, it is clear that in order to model the wake the following steps are taken: define the wake separation line which coincides with the trailing edge and is treated as the first section of the wake; identify which patch a

wake separates from, the side of the patch which is parallel to the separation line and the row of panels within the patch that the wake separates from. As described by Katz and Plotkin [64], this row of wake panels have a length dimension in the streamwise direction corresponding to

$$c_w |U_\infty| \cdot t$$

where the value of c_w is typically chosen to be $0.2 \div 0.3$. In the present implementation, a value of 0.25 was found to be adequate. This reduced value of c_w is a result of the use of vortex rings to model the wake vorticity rather than higher order vorticity distributions.

In this sense, from a numerical point of view, observe the importance of the distance and relative angle to the trailing edge. In fact, the wake vortex location should be aligned with the wing trailing edge and be placed closer to the latest position of the trailing edge. Therefore, the doublet when placed in the time interval introduces an approximation that underestimates the induced velocity when compared to the continuous wake vortex sheet result. This is so, since the distance of the continuous wake from the trailing edge during the time interval is a zero distance whereas the distance of an equivalent panel placed in the time interval is not zero. Therefore, to correct this wake discretization error it is necessary to place the wake panel with a value of length dimension in the streamwise direction chosen to be $0.2 \div 0.3$. Instead, for the successive rows of wake panels, the value of c_w is chosen to be 1: the length in the streamwise direction of $|U_\infty| \cdot t$.

Let N_{ts} be the time step in which one wishes to compute the solution and M_W the number of wake panels generated at each time step. Equations (3.78) and (3.79) are corrected in this way:

$$\sum_{K=1}^{N_B} A_{JK}^d \mu_K = \sum_{K=1}^{N_B} B_{JK}^d \sigma_K - \sum_{I=1}^{N_{ts}-1} \sum_{L=1}^{M_W} C_{JIL}^d \mu_{IL}^w$$

fact that the wake is imposed and thus the flow field can not influence the wake.

So far the wake modelling is only characterized by using of common wake panels. In the next chapter, it will be possible to see how the wake may be modeled by means of three dimensional singularity point vortex which will be really generated by the panels wake.

3.3.3 Computation of velocities and forces

For the computation of the total velocity in any point P outside the body, rewrite equation (3.56) in discrete term:

$$\underline{U}(P) = \underline{U}_\infty(P) - \sum_{K=1}^{N_B} \underline{U}_K^\mu \mu_K - \sum_{K=1}^{N_B} \underline{U}_K^\mu \mu_L^w + \sum_{K=1}^{N_B} \underline{U}_K^\sigma \sigma_K \quad (3.84)$$

where the coefficients

$$\underline{U}_K^\sigma = \iint_{\text{panel } K} \underline{\nabla} \frac{1}{r} dS \quad ; \quad \underline{U}_K^\mu = \iint_{\text{panel } K} \underline{\nabla} \left(\underline{n} \cdot \underline{\nabla} \frac{1}{r} \right) dS \quad (3.85)$$

have the same physical significance of the corresponding coefficients of equation (3.65) and (3.66).

In the same way, one can start by equation (3.57) for velocity calculation in every single point lying on the body surfaces, particularly in the grid points and control points. However, for the points lying on the surfaces, it is most advantageous to use equation (3.58) which, for the computation of the tangential components of velocity perturbation, may be applied to an explicative scheme, as follow:

$$u_{t1} = \frac{\mu(J_3) - \mu(J_1)}{d_1 + d_3} \quad ; \quad u_{t2} = \frac{\mu(J_4) - \mu(J_2)}{d_2 + d_4} \quad (3.86)$$

In the case of a Neumann boundary condition (see equation 3.59), the tan-

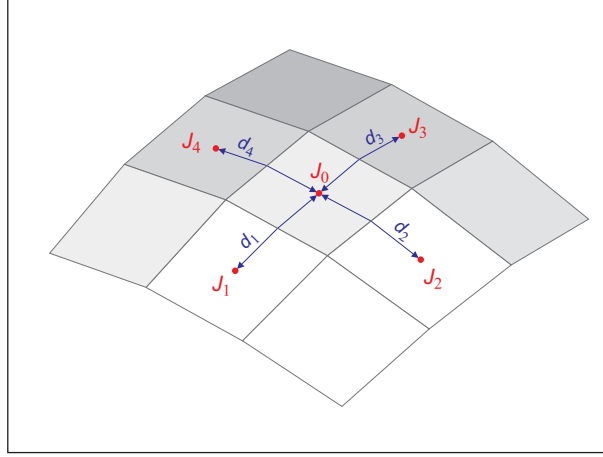


Figure 3.14: schematization of the computation of the velocity perturbation components.

gential component of velocity perturbation becomes:

$$u_{t1} = \pm \frac{(\mu(J_3) - \mu(J_1))/2}{d_1 + d_3} \quad ; \quad u_{t2} = \pm \frac{(\mu(J_4) - \mu(J_2))/2}{d_2 + d_4} \quad (3.87)$$

In reality, the panel distribution results difficultly so regular as illustrated in figure 3.14, therefore, in order to apply equation (3.58) it is necessary to use a more complex computational technique how, for example, building a function of doublet strength distribution on the basis of a large number of control point into the round of the interest point:

$$\hat{\mu} = f(\xi_i, \eta_i, \zeta_i, \mu_i) \quad (i = 1, \dots, n) \quad (3.88)$$

with the purpose to compute the derivatives.

After the velocity computation over the surfaces, it is possible to compute the corresponding distribution of pressure or, alternatively, of the pressure coefficient:

$$p = p_\infty + \frac{1}{2}\rho_\infty(U_\infty^2 - U^2) - \rho_\infty \frac{\mu(t) - \mu(t - \Delta t)}{\Delta t} \quad (3.89)$$

$$C_p = 1 - \frac{U^2}{U_\infty^2} + \frac{\mu(t) - \mu(t - \Delta t)}{\Delta t} \frac{2}{U_\infty^2} \quad (3.90)$$

thus, the force acting on every body:

$$\sum_{J=1}^{N_B} p_J \underline{n} S_J = \underline{F} \quad (3.91)$$

Chapter 4

THE VORTON METHOD FOR WAKE

The wake problem was analyzed by several authors. In particular way, Helmholtz analyzed the problem of two-dimensional body submerged in a flow field with the presence of a wake (called Helmholtz wake) behind the body whereas Von-Kármán studied the formation of vortices (called Kármán vortices) from a cylinder [50]. The goal of this chapter is to present and analyze a new vortex method as a tool for the direct numerical simulation of unsteady, inviscid and incompressible flows and, particularly, of vorticity localized on the thin wake regions. This new method is the vorton method, also called vortex particle method.

The wake is a vorticity region which may be discretized in several ways. In panel methods, as shown in chapter 2, the wake is discretized into panels. In the present method, the wake will be discretized into vortons. The classical wake panels will be transformed into vortons in several ways which will be analyzed herein in order to choose one that consents to solve the flow field without lose of accuracy in comparison to panel methods.

4.1 The vorton method

To present this technique, consider a vorticity region and let V be the volume of this region. Since vortex methods are based on the discretization of the vorticity domain, consider a generic uniform grid taken as a set of cubes of volume h^3 . A vorton, also called vortex particle, is simply a three-dimensional point vortex $\underline{\alpha}_p$ equal to the vorticity multiplied by h^3 , according to Cottet and Koumoutsakos [21]. This vortex element may be expressed as

$$\underline{\alpha}_p(x, y, z, t) = \alpha_{x_p}(t)\mathbf{i} + \alpha_{y_p}(t)\mathbf{j} + \alpha_{z_p}(t)\mathbf{k} \quad (4.1)$$

where $\alpha_{x_p}(t)$, $\alpha_{y_p}(t)$ and $\alpha_{z_p}(t)$ represent the scalar component of $\underline{\alpha}_p$, at a given time, along the x , y and z directions, respectively. In figure 4.1, the equivalence between a vorton and a simple vorticity region of vorticity (vortex tube with constant section area) is represented. Clearly, a vortex tube may be also discretized into so many vortons: as described by Winckelmans and Leonard [65], a vorton may be thought of a small section of a vortex tube.

The vector potential for this element is a solution of Poisson's equation $\nabla^2 \underline{\Psi} = -\underline{\omega}$. The solution of Poisson's equation is given by equation (A.9) which is an integral over the volume of vorticity. According to Strickland et al. [57][56], the vector potential is so given by

$$\underline{\Psi}_p(\underline{r}, t) = \frac{\alpha_p(\underline{r}, t)}{4\pi|\underline{r}|} \quad (4.2)$$

where \underline{r} is the distance from the vorton to the point of evaluation. Observe that above equation is singular for $\underline{r} = 0$. This singularity may lead to very large value when $|\underline{r}|$ approaches zero, therefore a core-function ξ_ψ is necessary to regularize the vector potential. Let σ and r_σ be the core-radius associated with the vorton and the ratio between the absolute distance of the evaluation point and the core-radius ($r_\sigma = |\underline{r}|/\sigma$). The core-function ξ_ψ is so that, when $r_\sigma < 1$, the vector potential decays linearly to zero.

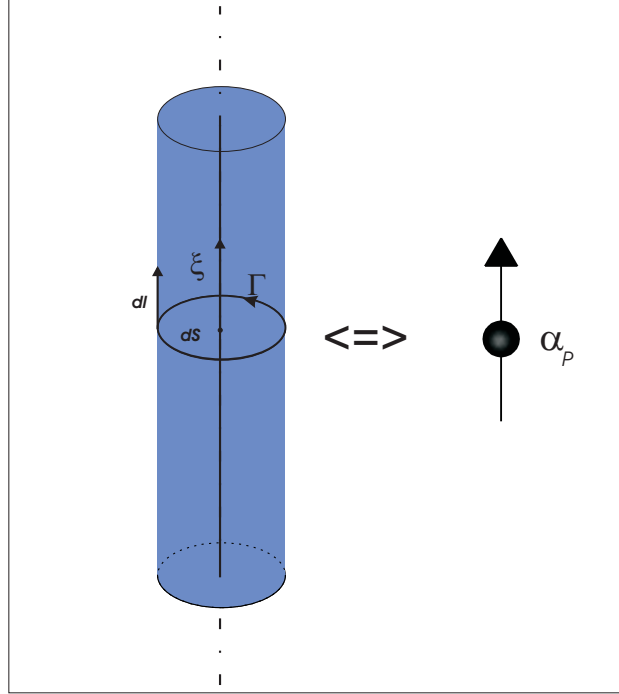


Figure 4.1: vortex tube and its corresponding vorton.

The velocity field induced by a single vorton is given by the curl of the vector potential:

$$\underline{U}_{\Psi_p}(\underline{r}, t) = \underline{\nabla} \times \underline{\Psi}_p(\underline{r}, t) \quad (4.3)$$

Therefore, a vorton is a singularity element with the velocity magnitude that decays as $1/r^2$, see figure 4.2. Since $\underline{\Psi}_p$ is a solution of Poisson's equation, the velocity field due to the single vorton is rotational and solenoidal everywhere. As for the vector potential, the velocity results singular for $\underline{r} = 0$. Similarly to the vector potential, a core-function ξ_U is introduced so that the vector potential decays linearly to zero when $r_\sigma < 1$, how illustrated in figure 4.2.

Note that a vorton results different from a two-dimensional vortex point. In fact, a 2D vortex is a solution of the Laplace's equation $\nabla^2\phi = 0$, where $\underline{U} = \underline{\nabla}\phi$ is irrotational by definition. Therefore, it is a singularity element

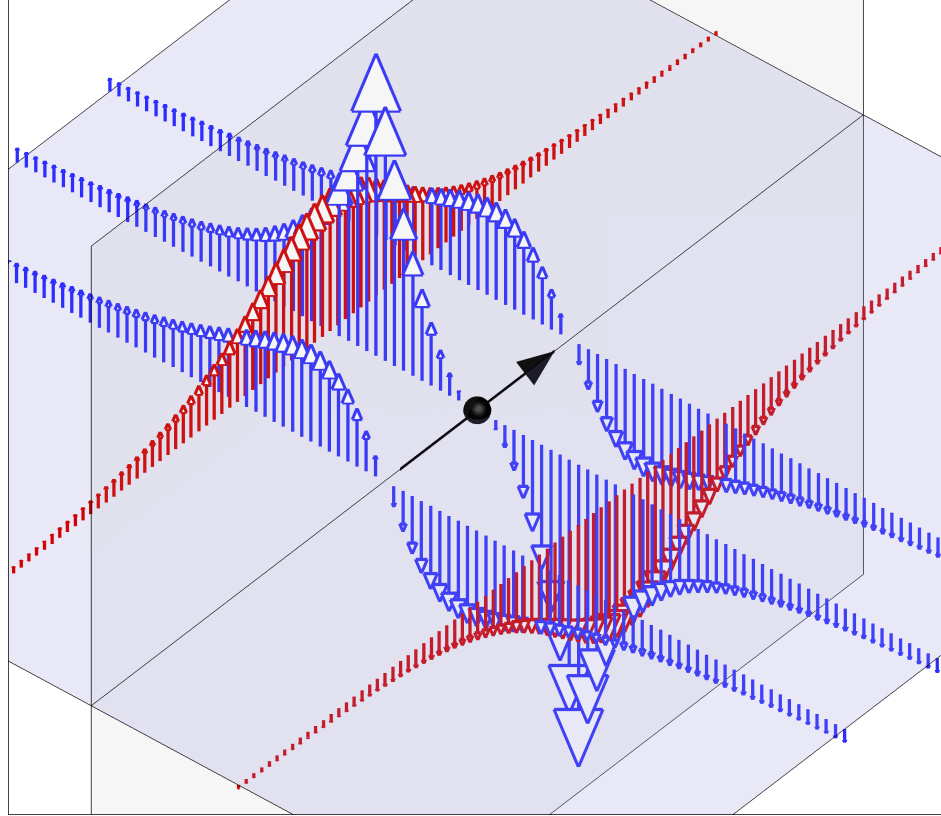


Figure 4.2: flow field induced by a vorton.

with only a tangential velocity component whose magnitude decays as $1/r$, being $\nabla\phi = -\underline{\Gamma}/(2\pi r)$ as illustrated in figure 4.3.

Moreover, the vorton evolution is governed by the vorticity evolution equation (2.52), therefore every single vorton is convected by the local velocity and strained by the local velocity gradient (stretching term in the vorticity evolution equation).

In order to approximate the exact initial vorticity field as accurately as possible, now the way to initialize the vortons will be described. For this purpose, begin by consider the vorticity region of interest that is the thin wake trailing the body surfaces. As shown in the previous chapter, this may be equivalently represented using equivalent doublet sheets and vortex rings.

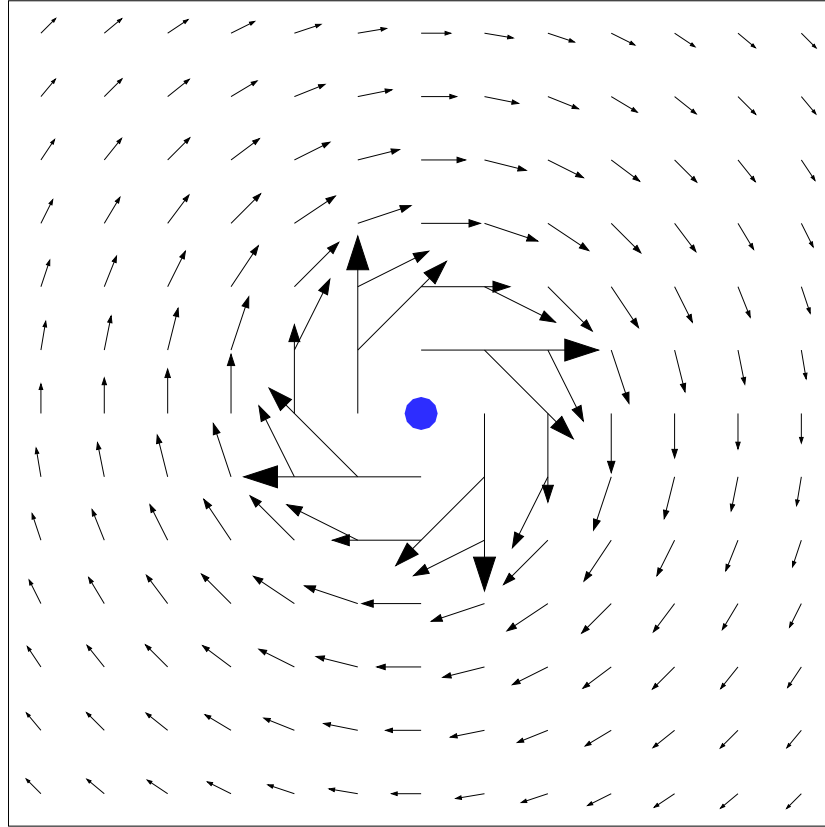


Figure 4.3: flow field induced by a two-dimensional vortex.

Thus, see how convert the wake commonly represented using vortex rings or equivalent doublet panels in the vortons that is how to assign the strength to the vorton so that the vorticity region represented by a vorton results equivalent to vorticity region represented by a common panel. According to Willis [63], the following steps are taken:

1. determine the equivalent vortex representation for every single doublet panel to be converted to vortons;
2. fix the number of vortons to be generated from every single panel;
3. divide the panel into equal area segments.

Therefore, the vorton is computed by integrating the strength of the vortex

line surrounding the panel area segment

$$\underline{\alpha}_p(\underline{r}, t) = \int \Gamma(t) d\underline{s} \quad (4.4)$$

In the vorton method, the vorticity is replaced by a set of vortons and therefore the vorticity field is approximated as the linear combination of the vorticities represented by the vortons, as follows

$$\underline{\omega}(\underline{r}, t) = \sum_P \underline{\alpha}_p(\underline{r}, t) \quad (4.5)$$

as shown by Winckelmans and Leonard [65], Willis et al. [63][64], Lebental [34], Alkemade et al [3], Voutsinas et al. [62], Chatelain et al. [18], Aksman and Novikov and Orszag [2], Park and Kim [48], Eldredge [26], Chatelain and Leonard [19], Voutsinas et al. [47], Spalart [53], Cottet and Koumoutsakos [21].

The velocity field $\underline{U}_\Psi(\underline{r}, t)$ is taken as the curl of the streamfunction which solves the Poisson's equation

$$\nabla^2 \underline{\Psi}(\underline{r}, t) = -\underline{\omega}(\underline{r}, t) \quad (4.6)$$

Recalling that the Green's function $G(\underline{r}, \underline{r}')$ for $\nabla^2 G = \delta(\underline{r}, \underline{r}')$ in unbounded domain is $G(\underline{r}, \underline{r}') = -1/(4\pi|\underline{r} - \underline{r}'|)$ (as shown in section A.1) and according to equation (4.2), the vector potential is the summation over the vector potential of all the vortons in the domain:

$$\underline{\Psi}(\underline{r}, t) = \frac{1}{4\pi} \sum_p \frac{\underline{\alpha}_p(\underline{r}, t)}{|\underline{r} - \underline{r}_p(t)|} \quad (4.7)$$

The velocity vector is obtained as the curl of the streamfunction $\underline{\Psi}$, as follow

$$\underline{U}_\Psi(\underline{r}, t) = \nabla \times \underline{\Psi}(\underline{r}, t) = \frac{1}{4\pi} \sum_p \frac{[\underline{r} - \underline{r}_p(t)] \times \underline{\alpha}_p(\underline{r}, t)}{|\underline{r} - \underline{r}_p(t)|^3} \quad (4.8)$$

where the velocity components are:

$$u_\psi = \frac{1}{4\pi} \sum_p \frac{1}{|\underline{r} - \underline{r}_p|^3} [(z - z_p)\alpha_{y_p} - (y - y_p)\alpha_{z_p}] \quad (4.9)$$

$$v_\psi = \frac{1}{4\pi} \sum_p \frac{1}{|\underline{r} - \underline{r}_p|^3} [(x - x_p)\alpha_{z_p} - (z - z_p)\alpha_{x_p}] \quad (4.10)$$

$$w_\psi = \frac{1}{4\pi} \sum_p \frac{1}{|\underline{r} - \underline{r}_p|^3} [(y - y_p)\alpha_{x_p} - (x - x_p)\alpha_{y_p}] \quad (4.11)$$

Therefore, the rotational velocity field may be constructed by means of a linear combination of a set of basis velocity fields, every one of which is induced by a vorton. Clearly, the implementation results very simple and easy.

Similarly, the gradient of the velocity used for the vorticity stretching in the vorticity evolution equation results:

$$\nabla \underline{U}_\Psi(\underline{r}, t) = \frac{1}{4\pi} \sum_p \nabla \left[\frac{(\underline{r} - \underline{r}_p) \times \underline{\alpha}_p(\underline{r}, t)}{|\underline{r} - \underline{r}_p|^3} \right] \quad (4.12)$$

Regarding the vorton evolution, this is characterized by a change of strength and position in time. Each vorton displacement derives from the velocity field caused by the other vortex particle [3].

Now, in the Lagrangian representation, the position evolution of a single vorton is governed by the velocity vector, as follow

$$\frac{d}{dt} \underline{r}_p(t) = \underline{U}_p(\underline{r}_p(t), t) \quad (4.13)$$

As for the evolution of the particle strength, the biggest difference between two-dimensional and three-dimensional vortex method is the existence of the stretching term. In two-dimensional case, since the vorticity direction is perpendicular to the velocity direction, this term always goes to zero. In three-dimensional case, the evolution of vorticity is governed by the stretching term which changes the orientation of the vorticity as well as its value for

every timestep. Vorton deformation is derived from the Helmholtz equation, therefore in Lagrangian approach follow

$$\frac{d}{dt}\underline{\alpha}_p(\underline{r}, t) = \underline{\alpha}_p \cdot \underline{\nabla} U_p(\underline{r}_p(t), t) \quad (4.14)$$

At this point, discretize the equations of the evolution of the vortons using a forward Euler scheme. First, the position of the vorton is updated,

$$\underline{r}(t + 1) = \underline{r}(t) + \underline{U}_p(\underline{r}(t), t) \Delta t \quad (4.15)$$

Second, then the strength of the particle is updated,

$$\underline{\alpha}_p(t + 1) = \underline{\alpha}_p(t) + \underline{\alpha}_p(t) \cdot \underline{\nabla} U_p(\underline{r}(t), t) \Delta t \quad (4.16)$$

Clearly, the use of higher order time stepping method will be beneficial in increasing solution accuracy.

A system of vortons can, in turn, be used to model body surfaces, container boundaries, free-surfaces, internal flows, jet flows, turbulent internal flow, and wakes in unsteady three-dimensional flow fields.

In the present work, vortons will be used to model wakes in unsteady, inviscid and incompressible flows because these vortex elements are more easily manipulated than the traditional wake sheet representation. In fact, panel methods presents the need to compute the induction of the flow field due to four segments of each doublet panel whereas the vorton discretization offers the possibility to compute the induction due only to a point for every single vorton. Hence, the vorton method results to be more attractive because it has also the advantage that the three-dimensional point vortexes are somehow independent as they do not necessarily belong to a specific wake panel for all times.

To summarize, the vorton method has been shown in order to solve Poisson's equation in the wake. Moreover, the two evolution equations of the

position and strength of the vortex particles have been presented also. Now, it is necessary to compute the initial strength and position of the vortons when they are created in the wake. Before this, it is necessary to describe the wake model in detail.

4.2 Conversion of the wake panels to vortons

As seen in above chapter, the wake in a common panel method may be modeled by means of a distribution of doublets with a strength so that the Kutta condition at the trailing edge results fulfilled. Now, the goal is to describe the conversion of the wake panels to vortons for an unsteady wake model which consists of a distribution of panels and a distribution of vortons.

In the wake model with vortons, the wake is divided into two parts: a near wake and a far wake. As regard the near wake, close to the wing, the wake is modeled using a wake sheet slicing the domain. This buffer wake sheet imposes the prescribed potential jump in the normal direction across the wake sheet and this is used to account for the vorticity recently shed into the domain from the wing trailing edge. Regarding the far wake, this is represented using a distribution of vortons. This wake decomposition is presented in figure 4.4.

The buffer sheet is at least composed of two rows of panels trailing from the wing trailing edge. Closest to the trailing edge, the panels of the first row are unknown wake panels because initially have an unknown strength: their strength is determined by the Kutta Condition. Instead, the panels of second row are known wake panels since correspond to the convected previous time-step unknown wake panels where the Kutta condition was resolved at $t = t - \Delta t$.

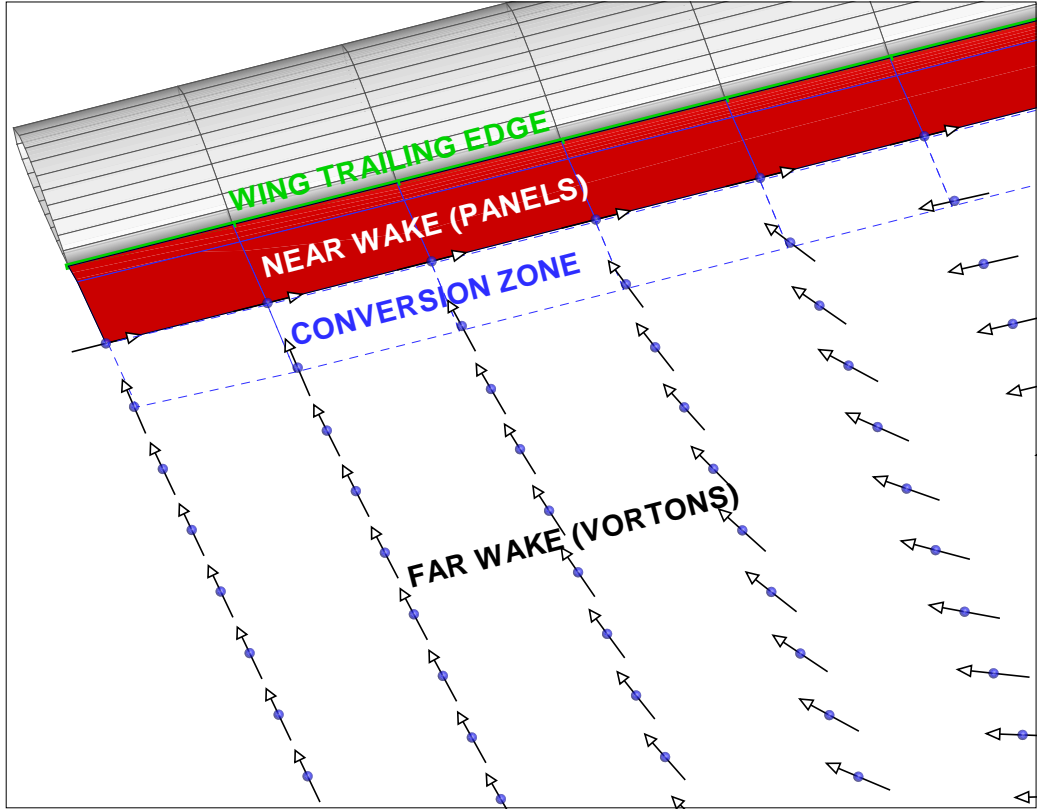


Figure 4.4: wake model with vortons.

As described for the unsteady panel wake, also in this case the first row of wake panels has a length dimension in the streamwise direction corresponding to $c_w|U_G| \cdot t$ where the value of c_w is chosen to be 0.25. The panels of the second row have a known strength corresponding to the previous timestep trailing edge potential jump with a value of c_w is chosen to be 1.

At each time step, the previous time-step second row of wake panels is converted into vortons.

Similarly to the panel wake model, the wakes will be constructed gradually at every time step generating a new row of buffer panels closest to the trailing edge and, furthermore, vortex particles will be created as the near parts of the wakes evolve.

An important point that must be considered for the conversion of the dipole wake sheet to vortons, is the equivalence between the change in doublet strength along the surface and vorticity oriented in the surface tangential direction normal to the doublet gradient (see section 2.1). In the particular case of constant doublet panels, the vortex analogue is a vortex ring around the perimeter of the given panel: hence, the strength of the vortex line segment between two adjacent constant strength panels is merely the difference in doublet strengths. Therefore, the vorton is computed by integrating the strength of the vortex line segments between adjacent panels depending on the examined model.

For this thesis, several ways of converting the quadrilateral panels into vortons both in term of location and volume of integration. They are represented in figure 4.5.

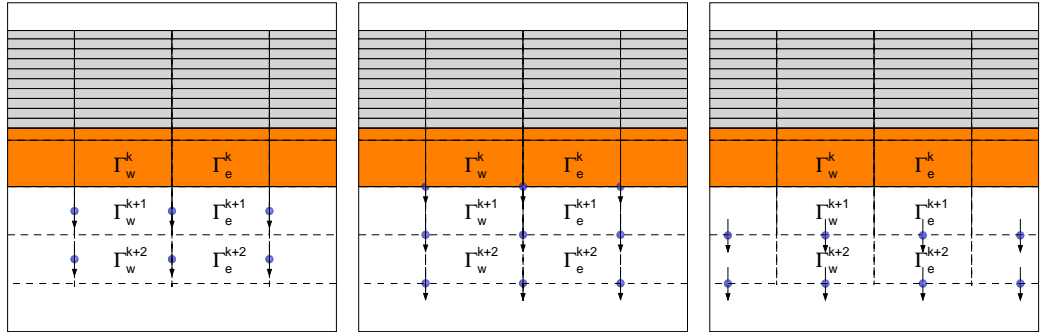


Figure 4.5: examples of models for the conversion of the near wake panels into vortons.

To summarize, the conversion is done in the following way [34]:

- the corners of each near panel of the second row are convected with the local velocity;
- the location and strength of vortons are calculated according to the relative model used;

- the strength of the vortex line between the near and the far wake is updated.

The third model represented in figure 4.5, called DIAS model, has been compared to the other two models and the panel wake model and it gives a very close answer for the aerodynamic forces to the theory with rings in the wake, as will be discussed in the next chapter and, therefore, it is the model used in this work. This model is characterized by the conversion of the wake panels to vortons localized on the vertexes of the transformed panels.

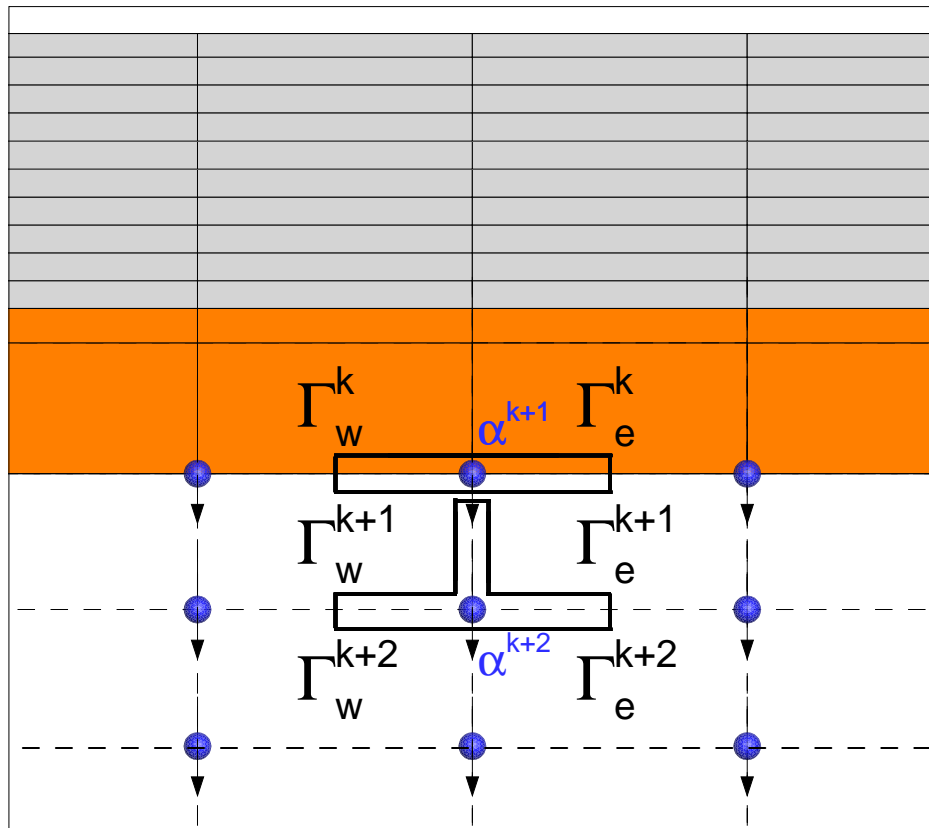


Figure 4.6: DIAS vorton wake model - the mechanism of vortex particles generation.

With the notation of figure 4.6 the vortons have the following strengths

$$\underline{\alpha}^{k+1} = t_{3w}^k (\Gamma_w^k - \Gamma_w^{k+1}) + t_{3e}^k (\Gamma_e^k - \Gamma_e^{k+1}) \quad (4.17)$$

$$\begin{aligned} \underline{\alpha}^{k+2} = t_{2E}^{k+1} (\Gamma_E^{k+1} - \Gamma_W^{k+1}) + 0.5 t_{3W}^{k+1} (\Gamma_W^{k+1} - \Gamma_W^{k+2}) + \\ + 0.5 t_{3E}^{k+2} (\Gamma_E^{k+1} - \Gamma_E^{k+2}) \end{aligned} \quad (4.18)$$

4.3 Summary

In this chapter, the attention has been addressed to analyse the flow field induced by any distribution of vortons chosen to represent any wake vorticity region. Moreover, a new wake model formed by both a distribution of panels and a distribution of vortons has been described. Particularly, several models of conversion of the wake panels to vortons have been examined in detail and between these models the DIAS vorton wake model has given a very close answer for the aerodynamic forces to the theory with rings in the wake. The DIAS vorton wake model has been introduced in the panel method solver PaMS (**P**anel **M**ethod **S**olver), realized by Caccavale [12]. The PaMS code has been modified in the way so to be able to model the wake with both the panel model and the model DIAS, as illustrated in following figures 4.7.

In the next chapter, the changes introduced in the PaMS code to model the wake also with the DIAS vorton wake and the test case and simulation examples will be described.

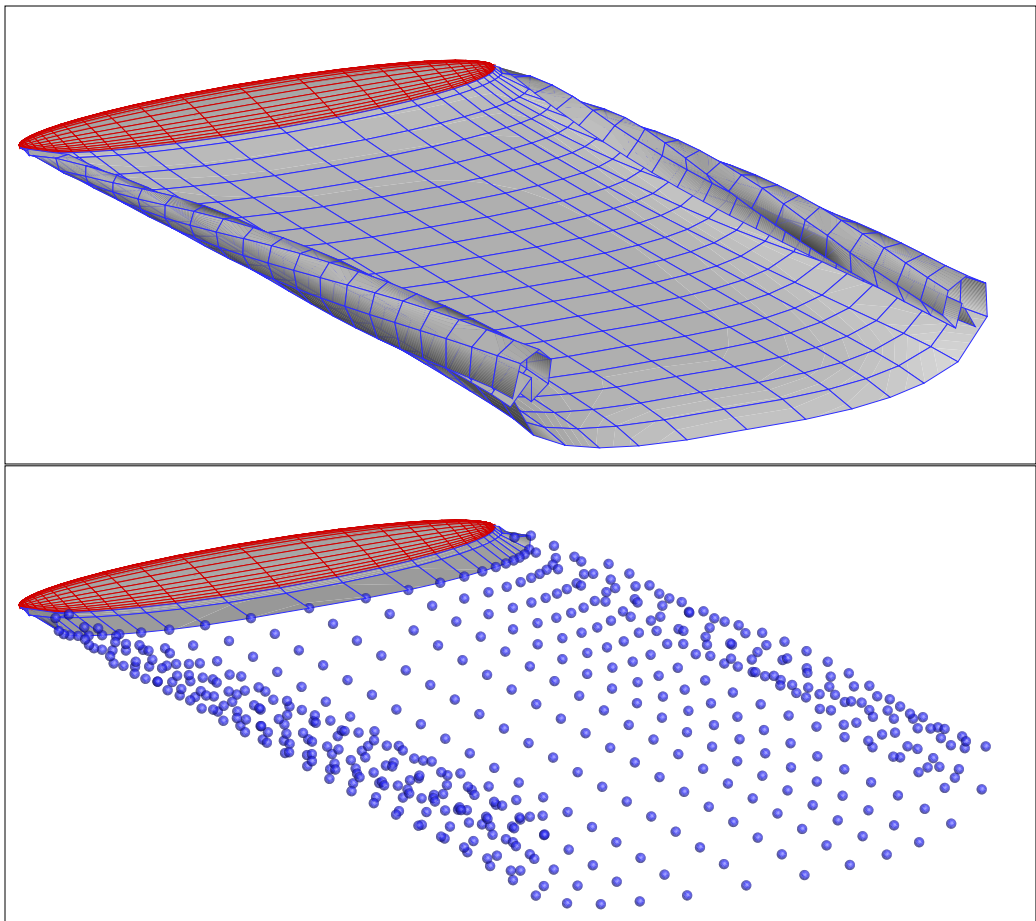


Figure 4.7: examples of panel wake and vorton wake.

Chapter 5

PaMS CODE WITH VORTON WAKES

The validation of the DIAS vorton wake model, described in above chapter, introduced to modify a classical panel method for unsteady flows is the goal of this chapter. Therefore, several test cases will be made for steady and unsteady, 2D and 3D flows. Moreover, some simulation examples will be shown for a variety of boundary and closure conditions, for different applications.

5.1 PaMS code description

PaMS (**P**anel **M**ethod **S**olver) code is an open source software for the resolution of potential flow fields by means of the panel method technique. The code has been developed at DIAS department in order to have satisfactory analyses and design tool, focusing on a drastic reduction of the costs, in terms of overall time, resources and man power, by using unstructured grid with both quadrilateral and triangular panels, and by introducing a

wide variety of boundary and closure conditions, including the existence of an air/water interface to perform a variety of aeronautical and naval fluid dynamic time-dependent calculations. These characteristics permit a greater simplicity and rapidity during the paneling without alteration of the result accuracy, permitting to improve the quality of the discretization of the bodies and to use a numerical representation of CAD designs, making unnecessary the steps consisting in the geometry treatment and paneling as a satisfactory acceptable CAD model is available.

Another simplification for the geometry treatment and paneling is an option for the treatment of eventual intersections between two or more bodies, which consents to panel separately different parts of a same ensemble (for example the wing-fuselage group of an airplane) and to reposition these parts on the basis of specific needs.

Other important peculiarity is the computation of pressure loads directly in the grid points, by means of a technique of reconstruction and derivation of the potential function and unlike the mean value in the adjacent control points. The possibility to dispose values of pressure correctly computed in the grid points consents to couple a fluid dynamic solution with a solver for structural analysis using the same paneling. Moreover, due to capacity to manage possible deformation of the bodies in time, it is simple to use the PaMS code to do also unsteady computations of fluid-structure interactions, as in the case of aeroelastic problems (like the sails), putting in new routines for the structural test or utilizing the coupling with commercial softwares.

At least, the possibility to interface directly with the most diffuse commercial softwares (Gambit, Nastran, Hypermesh, Tecplot) consents to utilize at one's best the approximatively developed codes and the codes dedicated to these operations putting the PaMS code in ideal conditions to increase its

performances.

This method has been used to solve a number of scientific and technical, steady and unsteady problems. It seems capable to perform complex simulations coupled to both structural and dynamics methods and/or by introducing deformations due to fluid dynamics loads [13].

5.2 Changes in the PaMS code for the introduction of a vorton wake model

This thesis work focuses on the numerical analysis of the vortons for the modelling of the wake in the panel method solver PaMS that has been modified in order to consent the use of both the panel wake model and the DIAS vorton wake model.

The changes in the PaMS code necessary to introduce the DIAS vorton wake model have been: the introduction of a technique of transformation of wake panels in vortons, the introduction of the velocity induced by the vorton distribution, changes in the calculation of the pressure.

Moreover, as described in the above chapter, several models for the conversion of the near wake panels into vortons have been analyzed, with particular attention to comparison between the flow field induced by a vorton wake to the flow field induced by a panel wake. The biggest advantage obtained with the DIAS model is that it permits to capture both all the circulation of the wake at the trailing edge and all the circulation of the wing-tip vortex.

Regarding the evolution of the vortons, the importance of the stretching term on the computation of the lift and drag characteristics is analyzed. The results of this analysis is that the effect of the stretching term on the lift and drag coefficients may be negligible. This fact may be explained by posing the

attention on the significance of the vortex-stretching mechanism for inviscid and incompressible flows.

It is well-known that a vortex tube which evolves in time deforms but, nevertheless, its surface remains a vortex tube throughout its deformation. Moreover, the constancy along the tube's length of the circulation around it implies that the absolute value of vorticity is largest where the cross-sectional area of the tube is smallest, similarly to the fluids acceleration at a contraction in a stream tube due to conservation of mass. Now, when a vortex tube evolves in time, its strength does not change with time, therefore reductions of a cross-section area of a tube cause proportional amplifications of the vorticity. Because of the incompressibility of the fluid, the volume between two sections of the tube remains constant and therefore every changing of the cross-sectional area must be accompanied by a longitudinal stretching. This is the vortex-stretching mechanism for incompressible and inviscid flows [58].

The vortex tube of interest in this case is the wake. The deformation of the wake rises with its strength which, in turn, rises with the rising of the lifting force. But, because the potential flow model may be applied only for bodies at low angles of attack with thin airfoils and small curvatures and hence for small value of the lift, the deformation of the wake is so that the stretching term in the vorticity evolution equation may be neglected.

Another aspect, examined in this numerical analysis, is the order of magnitude of the unsteady wake potential contribution, as described in chapter 2, for the computation of the pressure over the body. Only for finite-wing simulations this contribution is small and may be neglected especially for wing with thin airfoils and small curvatures at low angles of attack.

Moreover, even though a complete discussion of the various convergence

results for the vorton method is beyond the scope of this thesis, it is observed that error norms which express convergence to smooth solution of the Euler equations approach zero as the number of vortons increases and the core size decreases, under the constraint that the inter-vorton spacing goes to zero faster than the core size of the vortons, as noted by Marzouk too [39].

The vorton technique for modeling the wake has also shown to not suffer from large computational time and low accuracy but causes the reduction of the computational times and maintains the same level of accuracy respect to the panel wake model, as will be shown in this chapter by means of test cases.

Finally, we will show and discuss the most important advantage of the wake modeled by vortons: the possibility of intersection of the wake with downstream body surfaces.

5.3 Test cases

In order to demonstrate the applicability of the solution approach presented in this thesis a selection of relevant sample potential flows will be examined. Particularly, the vorton method will be compared to the panel method for the modeling of the wake.

5.3.1 NACA 0012 airfoil

The ideal flow theory consents to calculate, with a certain accuracy, the aerodynamic characteristic of wing sections, even though the simplifying assumptions limit its applicability. In fact, this theory permits the accurate calculation of the pressure distribution, in case of small effects of the viscosity on the pressure distribution. Moreover, wind-tunnel tests of finite-aspect-ratio

wing were made in the several NACA wind-tunnels to obtain wing-section characteristics which permit a further verification of the numerical solutions with the experimental data obtained with $M = 0.15$ and $Re = 9 \cdot 10^6$ [1].

In this section, NACA 0012¹ airfoil illustrated in figure 5.1 is examined.

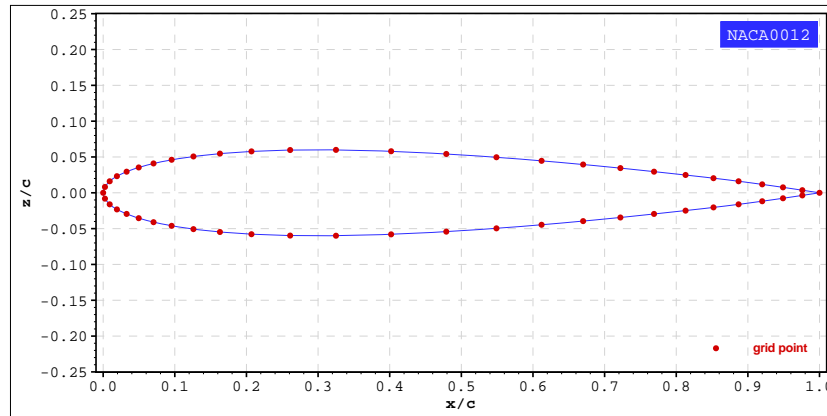


Figure 5.1: NACA 0012 airfoil - geometry.

To execute a 2D test with a 3D code it is required the use of a wing with as aspect ratio so to permit substantially the obtaining of a two-dimensional solution in midsection of the wing. For this reason, a rectangular wing with a symmetric NACA 0012 airfoil and aspect ratio of 20 is examined in this section.

The code is set by starting up the wake to impose the Kutta condition at the trailing edge. In order to value the effects due to wake, three types of models are compared (see figure and table 5.1): a classical panel wake

¹NACA 0012 is a wing-section of the four-digit series where the first integer represents the maximum value of the mean line ordinate z/c in per cent of chord, the second integer indicates the distance of the trailing edge to the location of the maximum camber in tenths of the chord whereas the last two integer indicate the section thickness in per cent of the chord. Therefore the NACA 0012 wing section is a symmetrical section and is 12 per cent thick.

(doublet wake), a vorton wake (DIAS vorton wake), a wake with only two rows of panels (near wake). For each model, the wake is set rigid (see figure 5.2).

Wake model	Time step [s]	Length of time [s]	Number of time step for wake
doublet wake	5	100	20 panels
DIAS vorton wake	5	100	2 panels + 18 vortons
near wake	5	100	2 panels

Table 5.1: three wake models used for the simulations.

The wing is discretized in 1352 quadrilateral panels: 26 panel widths in the spanwise direction by 26 panel widths in the chordwise direction with leading and trailing edge refinement.

In order to validate the numerical results, the analytical and numerical coefficients of pressure at several angles of attack and the experimental and numerical lift characteristics are compared, as illustrated in figures 5.3- 5.7. Observe that, the numerical results obtained by means of the DIAS vorton wake model present the same level of accuracy obtained by means of the classical doublet wake. Moreover, the numerical coefficients obtained with the near wake model show the importance of the vortons in order to have accurate results. Note that, by means of these characteristics, it is possible to verify the accuracy of the results and the smallness of the effects of the viscosity on the pressure distribution for $Re = 9.0 \cdot 10^6$ with small angles of attack (not superior to 12[deg]) for doublet and vorton models. Therefore,

with these values of Reynolds number and angles of attack, the lift characteristics show a linear trend, whereas for high angle of attack, the lift curve is not linear: the lift coefficient reaches a maximum value, whereupon the wing is said to stall since the lift trend is inverted.

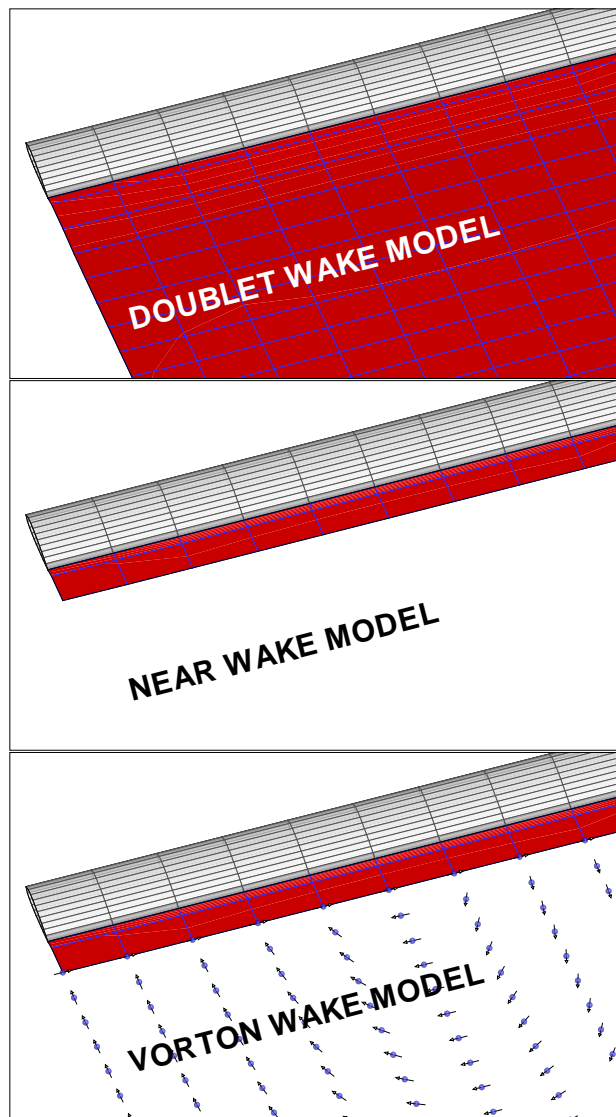


Figure 5.2: wake models.

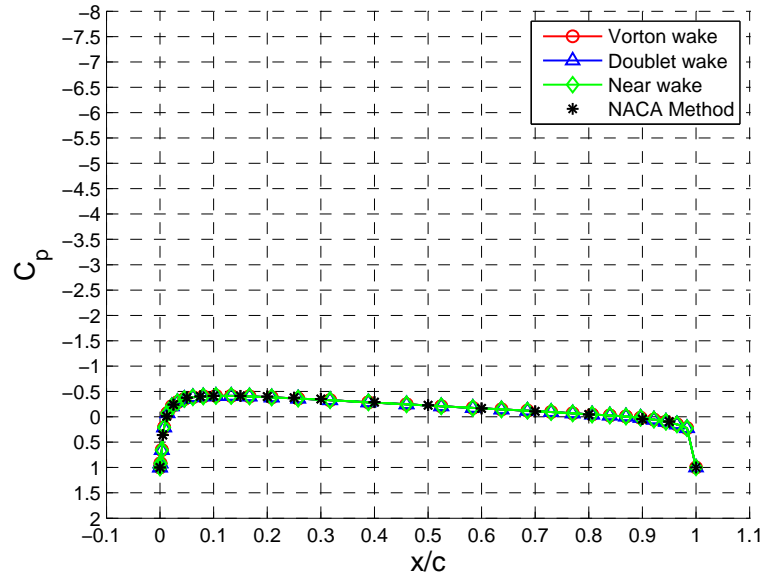


Figure 5.3: NACA 0012 airfoil at zero degrees angle of attack - comparison between the vorton wake model to the analytical results and the doublet wake model in terms of pressure distribution.

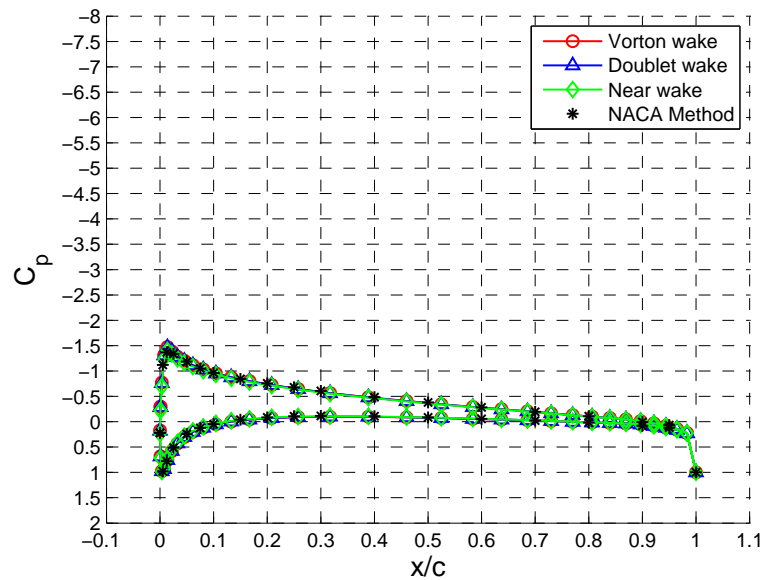


Figure 5.4: NACA 0012 airfoil at four degrees angle of attack - comparison between the vorton wake model to the analytical results and the doublet wake model in terms of pressure distribution.

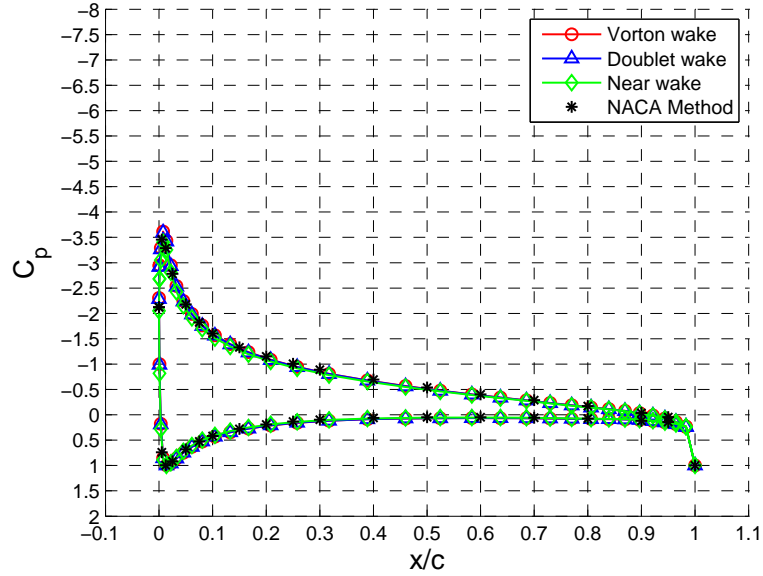


Figure 5.5: NACA 0012 airfoil at eight degrees angle of attack - comparison between the vorton wake model to the analytical results and the doublet wake model in terms of pressure distribution.

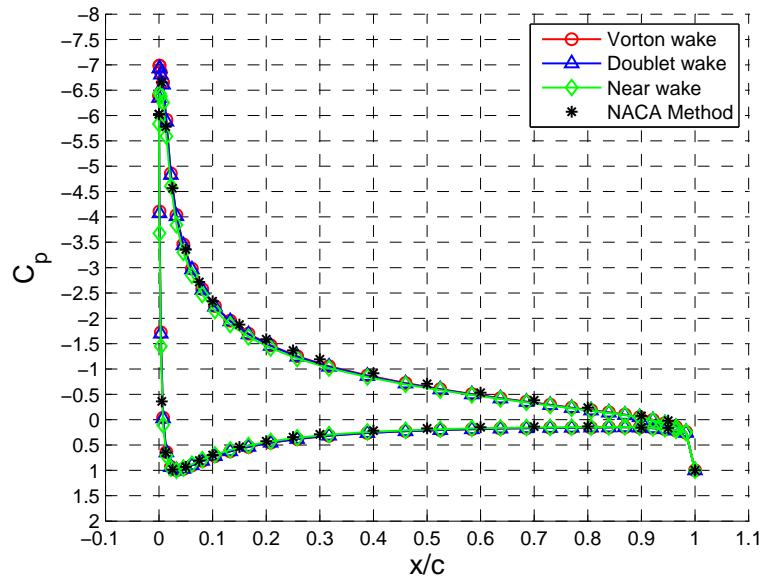


Figure 5.6: NACA 0012 airfoil at twelve degrees angle of attack - comparison between the vorton wake model to the analytical results and the doublet wake model in terms of pressure distribution.

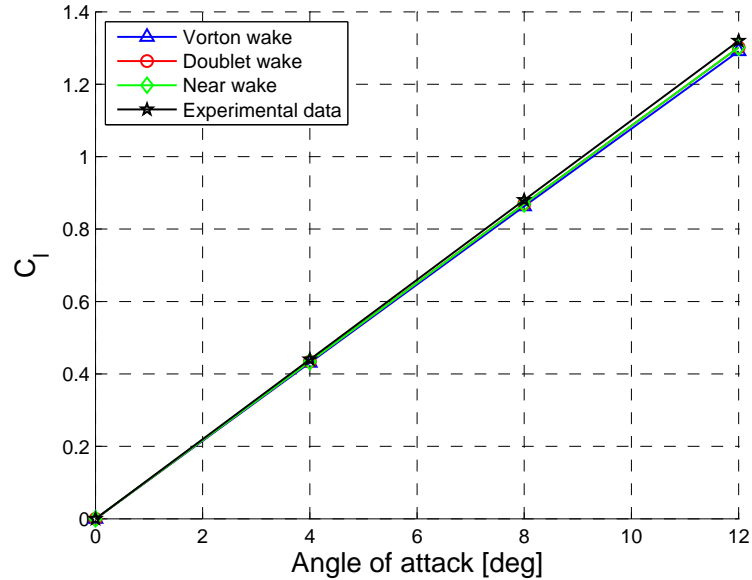


Figure 5.7: NACA 0012 airfoil - comparison between the vorton wake model to the analytical results and the doublet wake model in terms of lift characteristics.

To verify the steady nature of the solution, it is necessary to analyze the time evolution of the lift coefficient. The importance of this kind of analysis is also due to the fact that this analysis is useful to understand how much the wake must be developed before considering the results as steady. In fact, it is possible to value the distance from the body at which is necessary to make to extend the wake in order to be able to retain negligible the change of the solution in time (see figure 5.8).

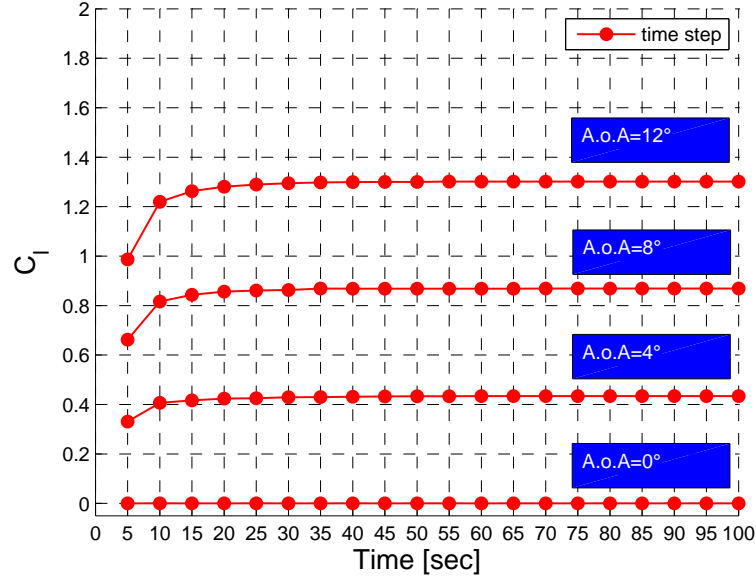


Figure 5.8: NACA 0012 airfoil - the time evolution of the lift coefficient for the DIAS vorton wake.

5.3.2 NACA 63 mean line

Similarly to the NACA 0012 airfoil, it is required the use of a wing with high aspect ratio. Therefore, a rectangular wing with aspect ratio of 20 and with the NACA 63² mean line is examined in this section (see figure 5.9). Also for this test case, the wing is discretized in 26 panel widths in the spanwise direction by 26 panel widths in the chordwise direction with leading and trailing edge refinement and, moreover, the wake is set rigid. The biggest difference between this test and the NACA 0012 is the absence of thickness which makes necessary the use of the Neumann boundary condition.

In figure 5.10 the comparison between the numerical and analytical solutions in terms of ΔC_p between upper and lower surfaces of the wing section is illustrated for the several wake models. The comparison has been made in

²The NACA 63 mean line is characterized by 6 per cent camber at 0.3 of the chord from the leading edge.

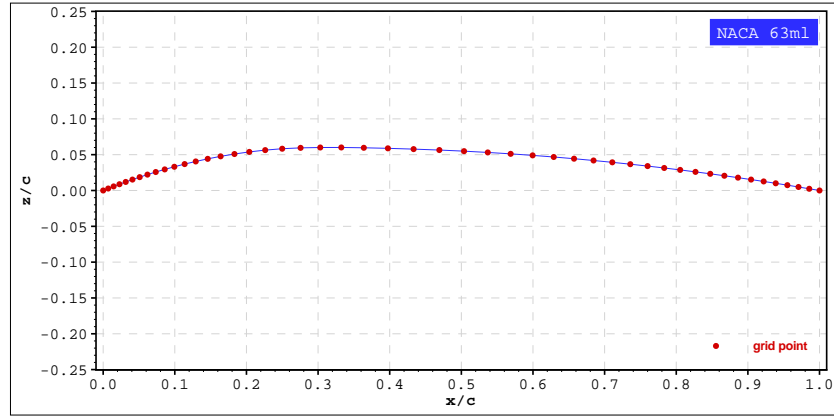


Figure 5.9: NACA 63 mean line - geometry.

condition of ideal angle of attack and the results in terms of lift coefficient are reported in table 5.2.

α_i [deg]	C_{l_i}			
	Abbott	DIAS vorton wake	doublet wake	near wake
1.6	0.80	0.74	0.73	0.71

Table 5.2: NACA63 mean line - analytical and numerical lift coefficients.

As well in this case, to verify the steady nature of the computation, the convergence story of the lift coefficient has been used (see figure 5.11).

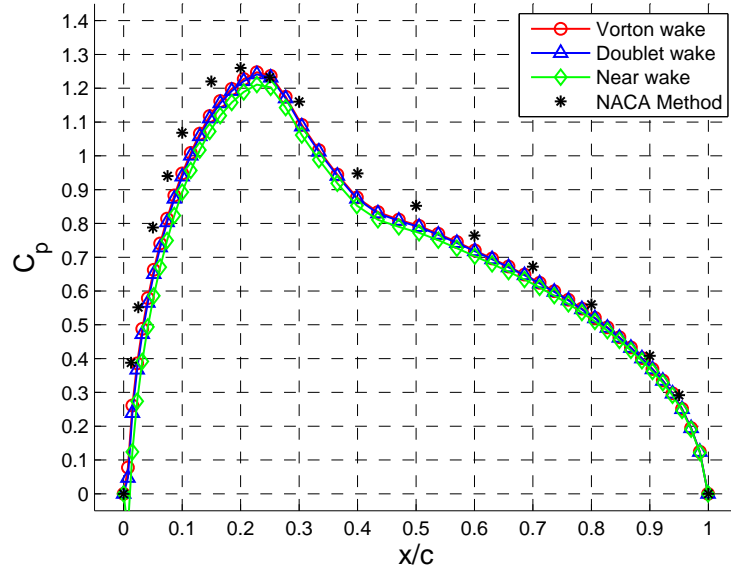


Figure 5.10: NACA 63 mean line at 1.6° ideal angle of attack - comparison between the vorton wake model to the doublet model and the analytical results in terms of pressure distribution.

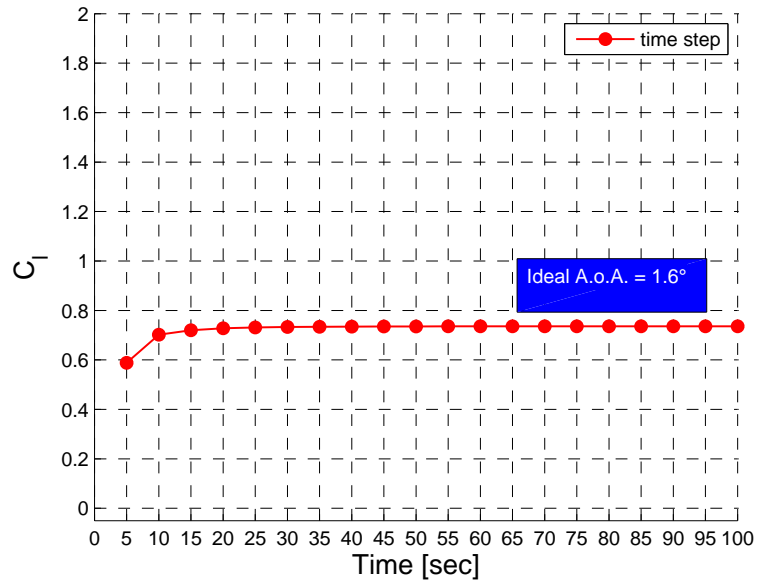


Figure 5.11: NACA 63 mean line - the time evolution of the lift coefficient.

5.3.3 Elliptic wing

The elliptic wing is a common test case and as so, the comparison of data from the Prandtl theory in the case of an elliptical lift distribution is made herein. There exist infinite ways to obtain a wing with elliptical lift distribution. One of this particularly interesting results is characterized by absence of geometric twist (that is, the geometric angle of attack α_g is constant along the span) and aerodynamic twist (that is, $C_{l\alpha}$ and α_{zl} are constant along the span) and an elliptical chord distribution along the span³ [5][60]. For an elliptical wing the characteristics of lift and induced drag are

$$C_L = \frac{C_{l\alpha}}{1 + \frac{C_{l\alpha}}{\pi AR}} (\alpha_{eff} - \alpha_{zl}) \quad (5.1)$$

$$C_{D_i} = \frac{C_L^2}{\pi AR} \quad (5.2)$$

where AR is the aspect ratio and the angle $\alpha_{eff} [rad]$ is the effective angle of attack which results

$$\alpha_{eff} = \alpha_g - \alpha_i = \alpha_g - \frac{\alpha_g}{1 + \frac{4b}{C_{l\alpha} c_0}} \quad (5.3)$$

where c_0 is the chord at the midsection of the wing.

In this examination, an elliptic wing with a symmetric NACA 0009 airfoil and aspect ratio of 10 is used. The wing is discretized in 26 panel widths in the spanwise direction by 16 panel widths in the chordwise direction with leading and trailing edge refinement and, moreover, the wake is set flexible (see table 5.3).

The results are illustrated for each model wake in table 5.4 and figures 5.12-5.13. Observe that, with a vorton wake, it is obtained the same level of

³For wings with elliptical lift distribution, the most interesting and important result is that the downwash is constant over the span and so the induced angle of attack is also constant along the span

Wake Model	Time step [s]	Length of time [s]	Number of time step for wake
doublet wake	0.5	15	20 panels
DIAS Vorton wake	0.5	15	2 panels + 18 vortons
near wake	0.5	15	2 panels

Table 5.3: three wake models used for the simulations.

accuracy for the computation of the lift and induced drag obtainable with a doublet wake and, therefore, these results present the same differences in comparison to the Prandtl theory. This is evident with both techniques for the calculation of the forces: the pressure integral and Trefftz plane. At last, the important difference existing between the vorton wake model and near wake model shows the influence of the wake vorticity field modeled by vortons on the coefficients of lift and induced drag.

PaMS CODE WITH VORTON WAKES

Wake Model	PaMS Trefftz plane		PaMS Pressure integral		Prandtl theory	
	C_L	C_{D_i} [count]	C_L	C_{D_i} [count]	C_L	C_{D_i} [count]
	$\alpha = 0^\circ$					
doublet	0.0000	0	0.0000	11	0.0000	0
vorton	0.0000	0	0.0000	11	0.0000	0
near	0.0000	0	0.0000	11	0.0000	0
	$\alpha = 4^\circ$					
doublet	0.3666	46	0.3702	47	0.3655	43
vorton	0.3667	47	0.3702	47	0.3655	43
near	0.2748	42	0.2757	54	0.3655	43
	$\alpha = 8^\circ$					
doublet	0.7367	182	0.7432	156	0.7311	170
vorton	0.7371	184	0.7428	154	0.7311	170
near	0.5514	165	0.5511	183	0.7311	170
	$\alpha = 12^\circ$					
doublet	1.1165	409	1.1249	340	1.0966	383
vorton	1.1163	411	1.1221	333	1.0966	383
near	0.8324	369	0.8273	396	1.0966	383
	$\alpha = 16^\circ$					
doublet	1.5104	725	1.5190	602	1.4622	681
vorton	1.5087	727	1.5117	587	1.4622	681
near	1.1209	649	1.1051	688	1.4622	681

1 *count* = 10^{-4}

Table 5.4: elliptic wing at several degrees angles of attack - comparison between numerical and theoretical results.

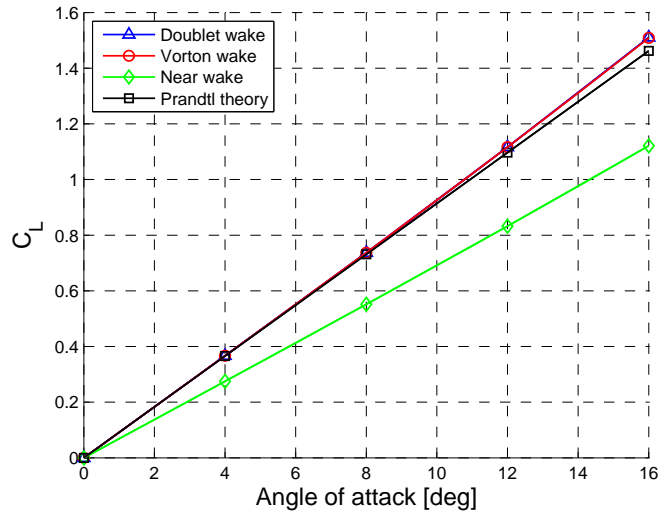


Figure 5.12: elliptic wing lift characteristics - comparison between doublet model and vorton wake model with the technique of the Trefftz plane.

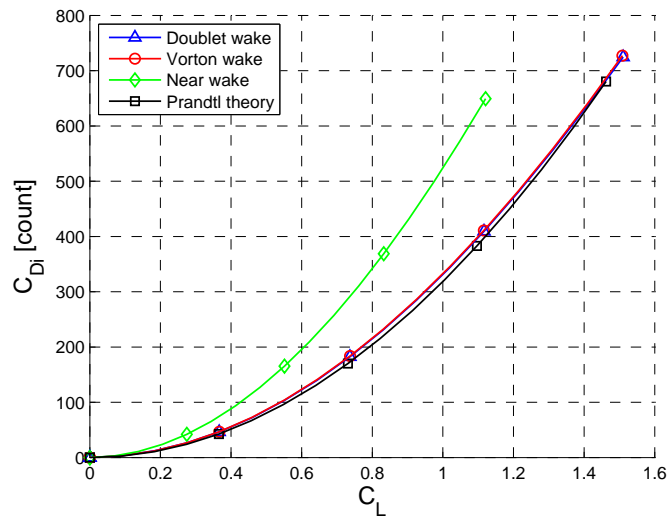


Figure 5.13: elliptic wing drag characteristics - comparison between doublet wake model and vorton wake model with the technique of the Trefftz plane.

5.3.4 Unsteady pitching airfoil

In order to validate the unsteady time dependent flow solution capabilities of the method presented, an unsteady pitching airfoil will be examined in this section [59][66][27]. This test case demonstrates the ability of the solver to compute unsteady flows in which wake-body interactions play an important role in the overall production of the forces. The pitching airfoil simulations are compared to analytical expression for an oscillating two-dimensional thin airfoil which is presented by Theodorsen and to experimental data with $M = 0.3$ and $Re = 3.9 \cdot 10^6$, resulted by unsteady wind-tunnel for the NACA 0012 airfoil [36][37][49][54] of whom those with pitching motion about a point on the airfoil chord at a distance $1/4$ of the chord from the leading edge. The instantaneous angle measured clockwise from the mean chord is α :

$$\alpha(t) = \alpha_m + \alpha_a \sin(\omega t + \phi) = 2.64^\circ + 10.16^\circ \sin(\omega t - \pi/2) \quad (5.4)$$

where $\omega = 2U_\infty/ck$ is the frequency relate to the so called reduced frequency k , α_m is the mean angle of attack, α_a is the amplitude of pitching oscillation, ϕ is the phase angle ahead of the pitching motion (see figure 5.14).

The computational results presented and compared with the Theodorsen theory and the experimental data in figure 5.15 compare favorable both with theory results to test data. This result is due to the method accuracy representing the unsteady vorticity in the wake.

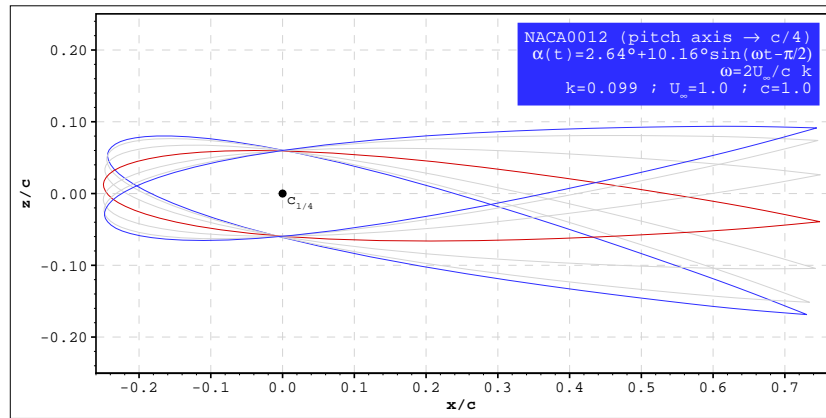


Figure 5.14: NACA 0012 airfoil - pitching.

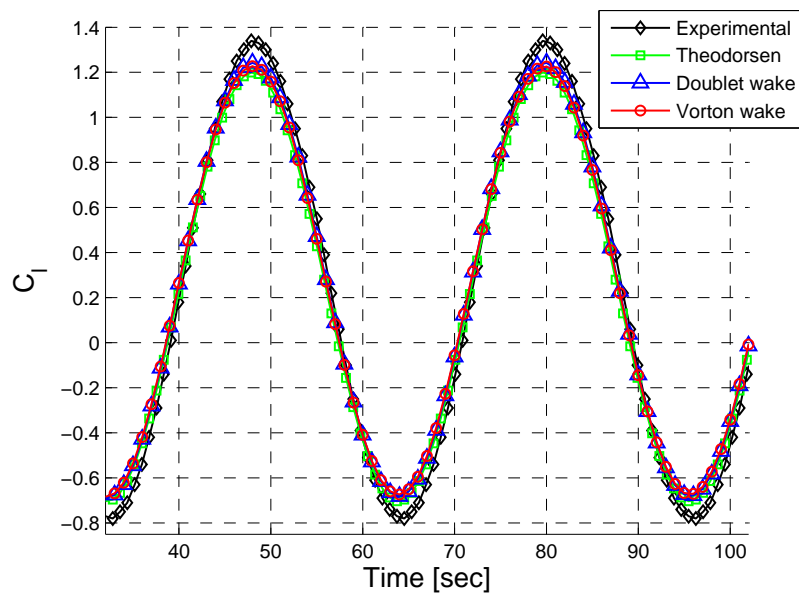


Figure 5.15: NACA 0012 airfoil - comparison between the numerical analysis to the Theodorsen theory and the experimental data in terms of lifting coefficient resulting from pitching motion.

The simulation results for the pitching oscillations demonstrate the versatility and easy use of the panel method with the vorton wake method. In figure 5.16 vorticity wake structure plots presented for examined pitching motion illustrate both the vorticity structure and the vorticity evolution in

time.

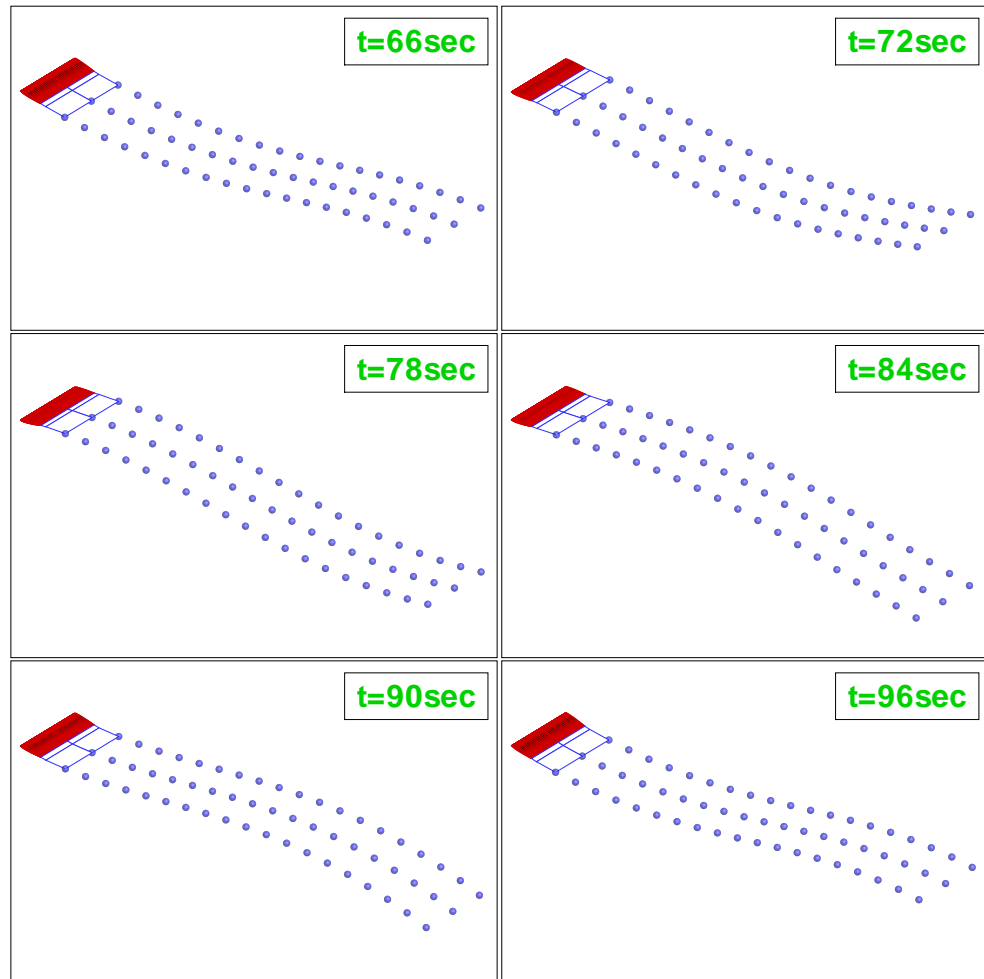


Figure 5.16: example of pitching motion for a NACA 0012 airfoil.

5.4 Vertical-axis wind turbine

The basic aim of these investigations is to focus on performance behavior of the PaMS code with the DIAS vorton wake model when the wake intersects with body surfaces.

Vertical-axis wind turbines are vertical-axis rotors that may be submerged and subject to an incoming flow. The blade has straight rectangular with a high aspect ratio and it is connected to the rotor shaft by one or more arms. The blade has a blade pitch degree of freedom given by the possibility to rotate around a spanwise hinge axis between two fixed positions.

5.4.1 A single-bladed turbine

For this test, the numerical results will be compared to results and of experiments conducted to determine the characteristics of the unsteady blade loadings and dynamic stall phenomena as they occur on Darrieus turbines [46] which will be described briefly herein. A single-bladed turbine with a NACA 0015 airfoil operated in a water tow tank with a depth of 1.25 meters, a width of 5 meters, and a length of 10 meters. An airfoil chord length of 15.24 cm and a rotor tip speed of 45.7 cm/sec were chosen to yield a blade Reynolds number of $6.7 \cdot 10^4$. Three towing speeds of 18.3 cm/sec, 9.1 cm/sec, and 6.1 cm/sec were chosen: in this test only the speed of 9.1 cm/sec is considered to yield tip-to-wind speed ratio 5.0. The rotor diameter was chosen to be 1.22 meters, thus giving a chord to radius value (indicative of the oscillation frequency) of $C/R = 0.25$ and the tip-to-wind speed ratio (indicative of the oscillation amplitude) was varied over a limited range. Measurements of radial and tangential forces using strain gage instrumentation.

In order to analyse the effects due to wake model on the simulations,

begin by considering a rigid panel wake model. Figure 5.17 shows, in three-dimensional view, the blade which intersects with wake released by itself. The impact determines a temporary loss of performance of the impacting blade. Specifically, pressure distribution on the blades is dramatically affected by the impact of wake vortices released by other blades.

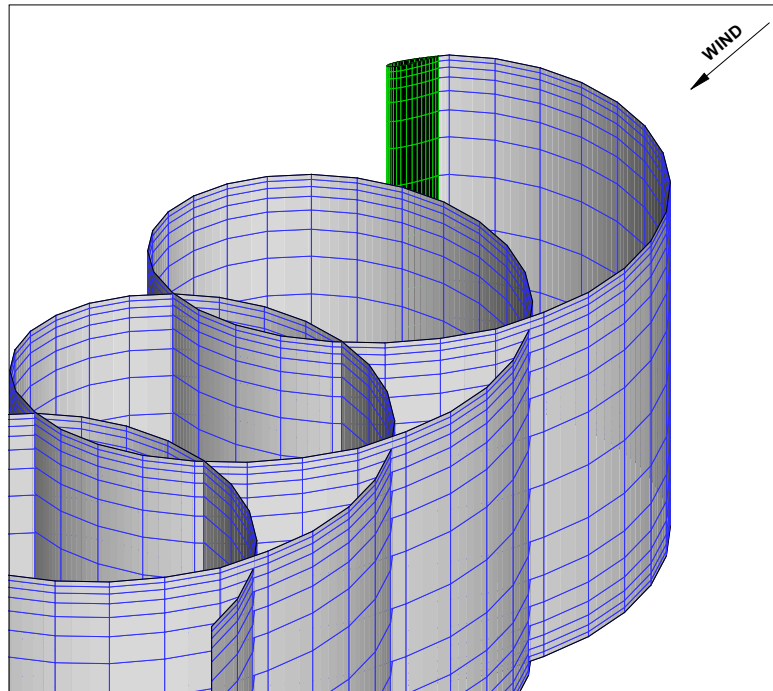


Figure 5.17: single-bladed vertical-axis turbine - rigid panel wake.

When the wake is modeled by flexible panels and the blade impacts on the vortical wake released by itself, the solution becomes numerically unstable because of the disconnection between the wake panels. Figure 5.18 illustrates a scheme of this numerical instability.

When the wake is modeled by vortons, because of the fact that the vortons are somehow independent as they do not necessarily belong to a specific vortex filament or sheet for all time, the solution keeps stable when the blade impacts on the vortical wake released by itself (see figure 5.20-5.19).

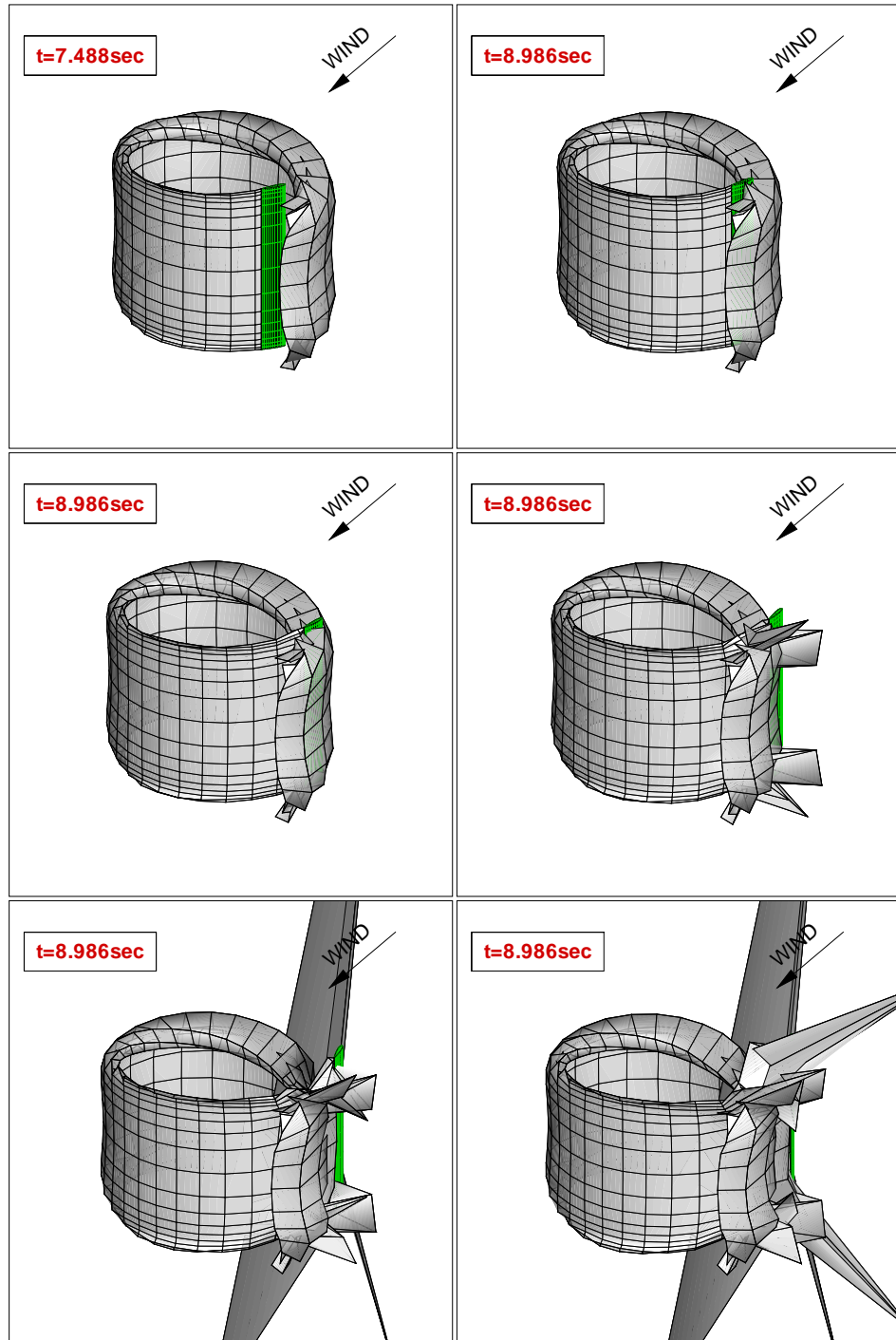


Figure 5.18: single-bladed vertical-axis turbine - Numerical instability of panel methods with flexible panel wakes.

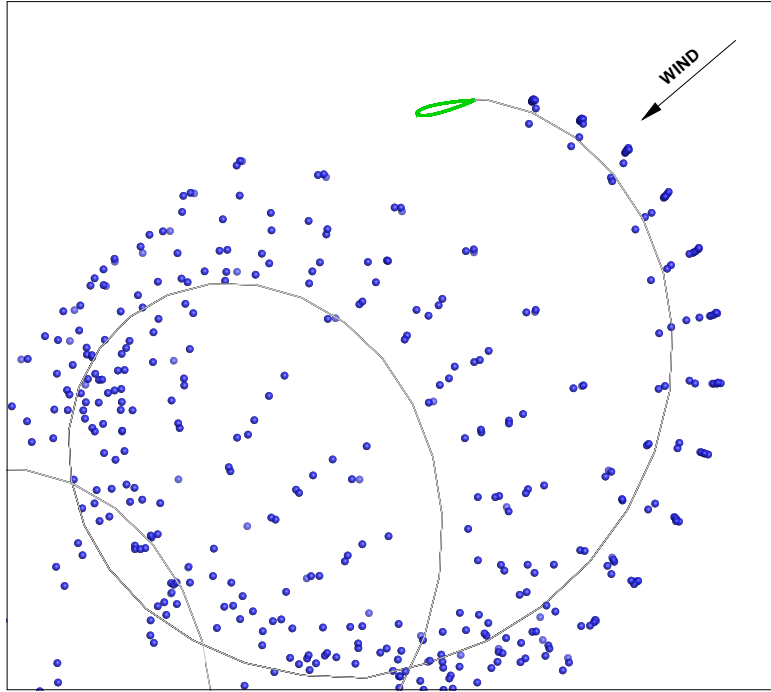


Figure 5.19: single-bladed vertical-axis turbine - DIAS vorton wake.

At this point, analyze the results of these simulations in terms of radial and tangential forces on blade, for both the cases of rigid panel wake and DIAS vorton wake.

Typical blade forces⁴ are shown in instantaneous progression of figures 5.21, 5.22. The tangential forces are an order of magnitude smaller than the radial forces and thus tends to be more difficult to measure. For the radial and tangential forces the agreement between the strain gage measurements and numerical results is seen to be reasonably good in the upstream region between 0° and 180° . Such agreement continues in the downstream region between 180° and 360° only between the experimental and numerical results obtained modeling the wake with the DIAS vorton wake because, for the

⁴A positive radial force acts radially outward while a positive tangential force acts in the direction of motion of the airfoil.

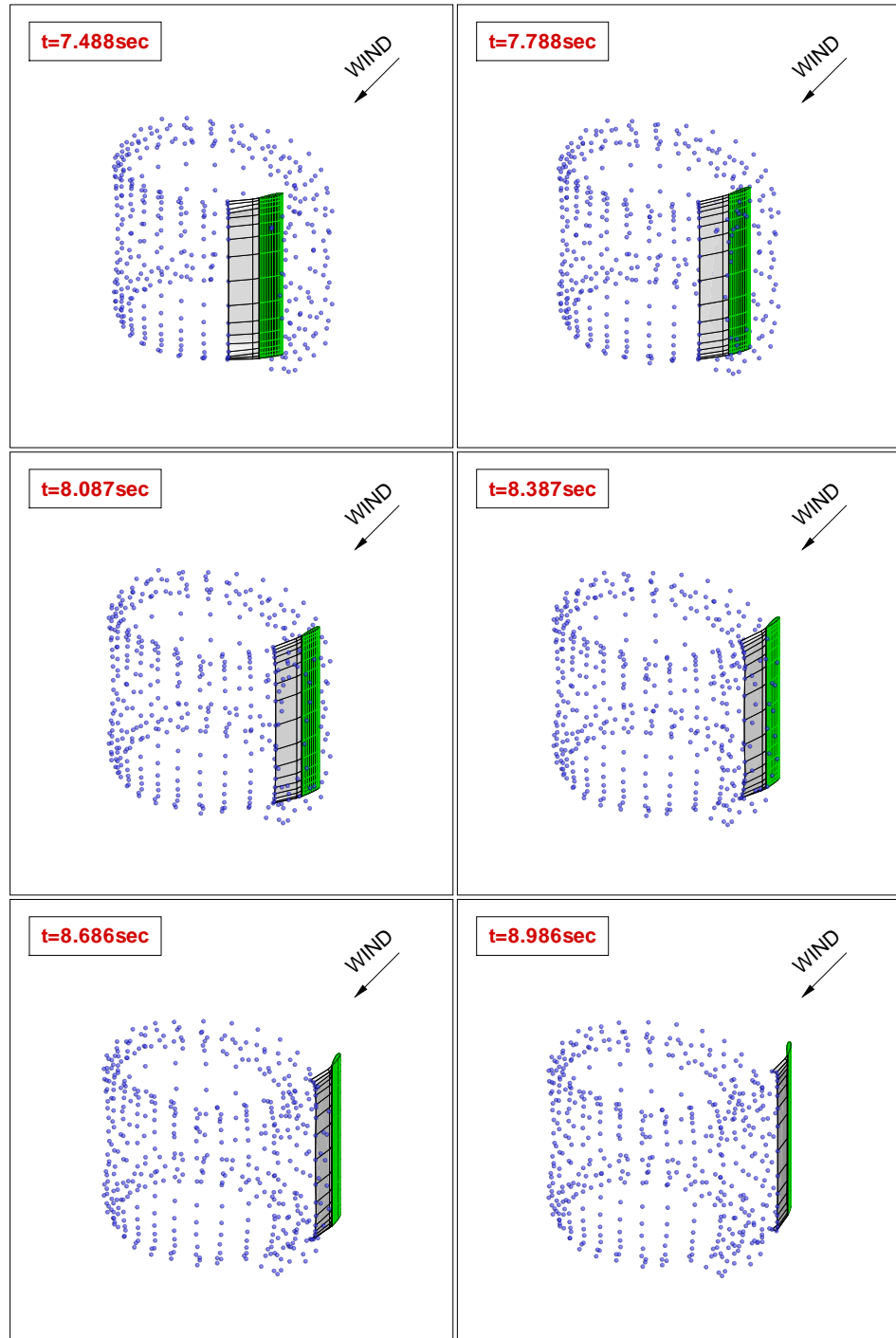


Figure 5.20: single-bladed vertical-axis turbine - solution stability of panel methods with vorton wakes during the intersection of the wake with the body.

panel wake, the obtained forces are dramatically affected by the impact of wake vortices released by the blade. In fact, the ripples in the numerical results represent the regions of bladewake impacts: physically, the interaction of a blade with its wake is responsible for a sudden change of the pressure distribution on the blade surface and hence of blade-generated loads. The results show that the PaMS with a rigid wake model tends to overestimate blade forces during the impact phase whereas with the DIAS vorton wake model this overestimate does not occur.

Observe, moreover, that the imperfect accuracy of predicted forces obtained with the DIAS vorton wake model compared to the experimental may be explained noting that these forces are, however, affected by viscosity not included in the PaMS code.

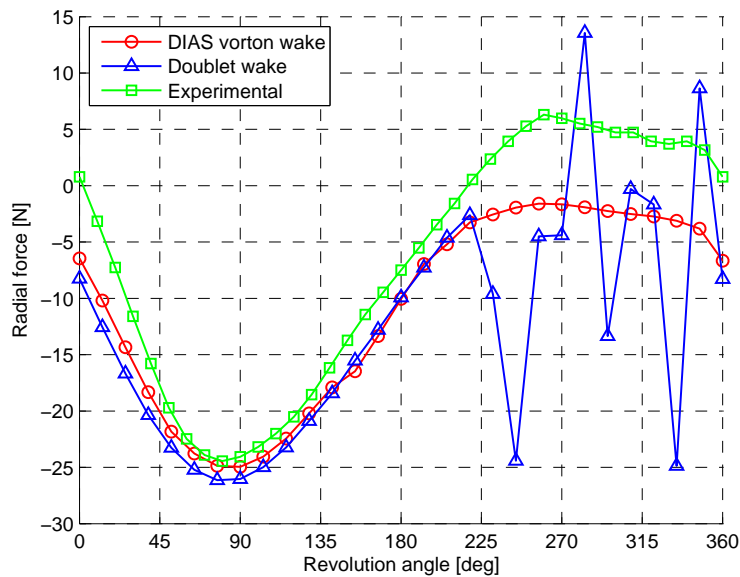


Figure 5.21: single-bladed vertical-axis turbine - radial forces on blade during a revolution. Numerical result compared to experimental data.

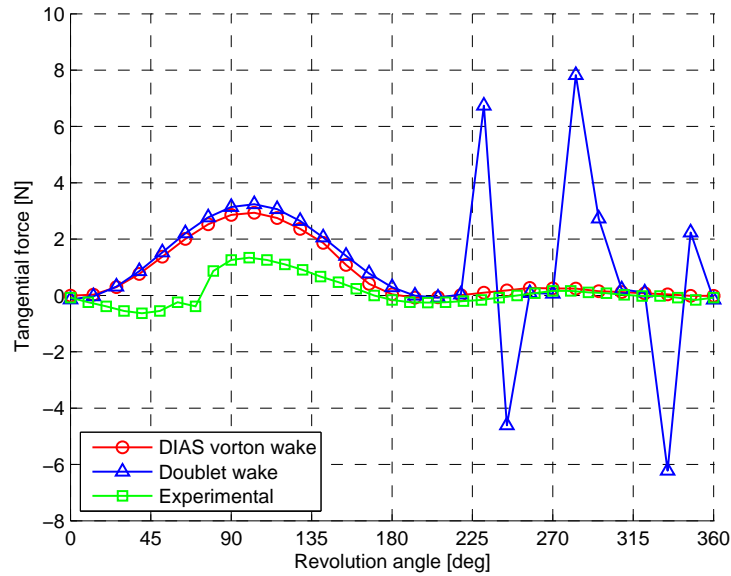


Figure 5.22: single-bladed vertical-axis turbine - tangential forces on blade during a revolution. Numerical result compared to experimental data.

5.4.2 A three-bladed turbine

For the case of a three-bladed turbine, the simulation is made in the same conditions of the single-blade case, simply by disposing three blades at angles of 120° .

Observe that the possibility of wake/blade impingement depends on the ratio between the wind speed and the turbine rotational speed and increases as the number of turbine blades is increased. A suitable wake model to take into account these effects is certainly a vorton wake (see figure 5.23).

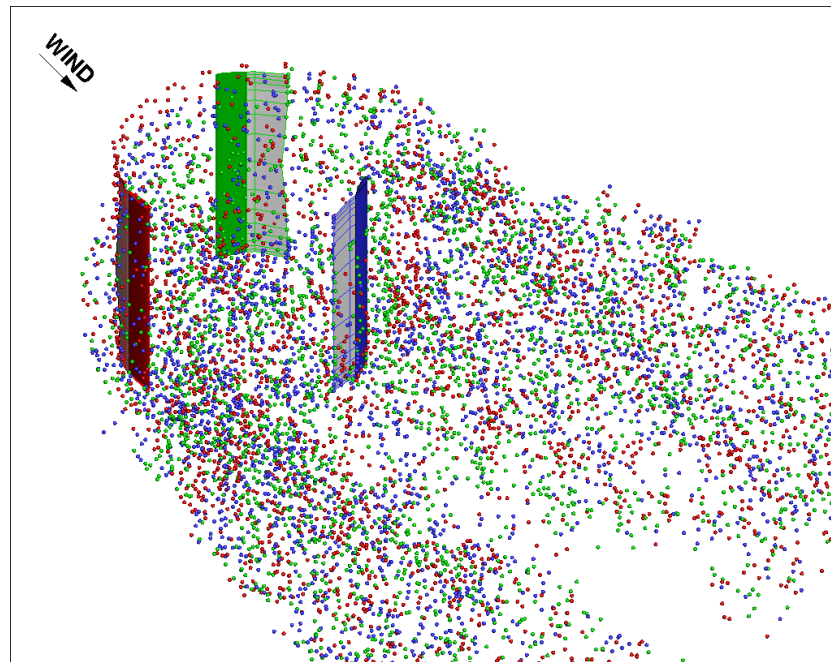


Figure 5.23: three bladed turbine - vorotn wakes.

Analyze the radial and tangential forces along the rotor revolution angle for one single blade and the turbine power. As shown in figure 5.24 and 5.25, the maximum values reached by these forces in the upstream region between 0° and 180° are lower than the maximum values shown for the case of single blade.

The multi-bladed turbines are important for industrial applications which are oriented towards the production of electric power. Figure 5.26 shows the evolution of the power developed by the three bladed turbine.

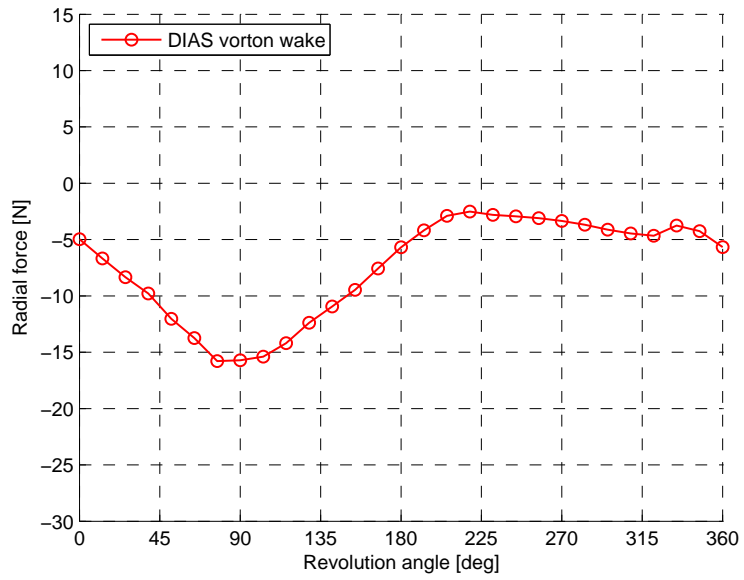


Figure 5.24: three bladed turbine - radial force.

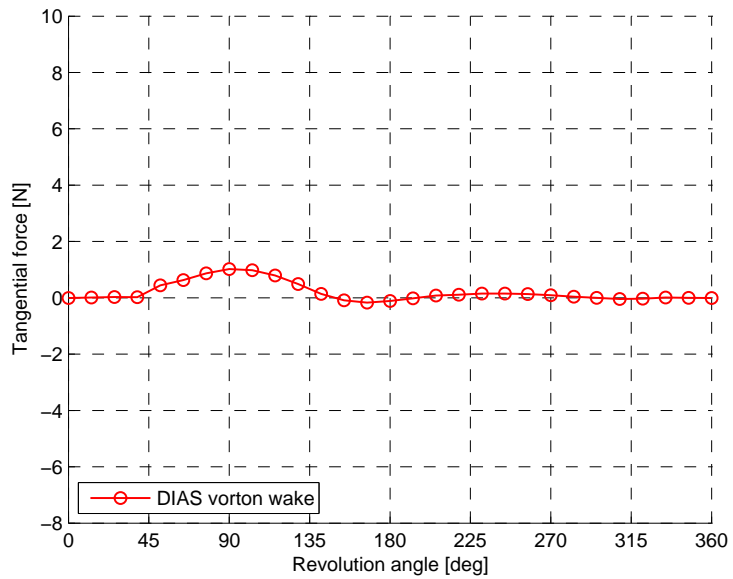


Figure 5.25: three bladed turbine - tangential force.

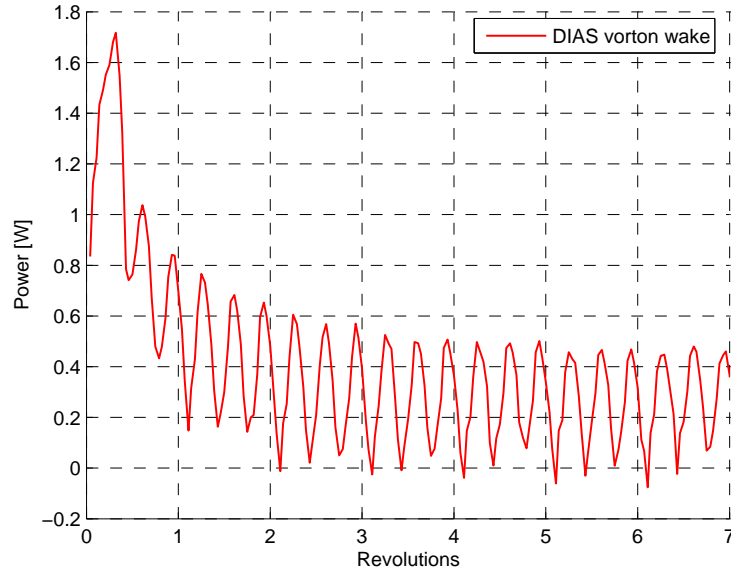


Figure 5.26: three bladed turbine - power.

5.5 Intersection of the wake of a pitching and heaving wing with a downstream fixed wing

In this section, the attention is focused on the behavior of the PaMS code with the DIAS vorton wake model when the wake of a pitch-heaving wing intersects with downstream fixed wing.

The pitching and heaving wing is a straight rectangular wing with a high aspect ratio ($AR = 20$) with a NACA 0012 airfoil and chord length of 1 m. The downstream body is a straight rectangular wing with the same aspect ratio and airfoil of the upstream oscillating wing.

In this case, the impact of the wake with the body may be modeled by means of a flexible panel wake, as illustrated in the upper side of figure

5.27, but the level of accuracy obtained by this model is lower than the level obtained using the DIAS vorton wake model, shown in the lower of figure 5.27. In fact, the intersection of the downstream body with the upstream wake causes, in the case of panel wake, a sudden change of the pressure distribution on the downstream wing.

In order to analyse the effects due to wake of the oscillating wing on the pressure distribution over the downstream wing, the results of this simulation in terms of lift coefficients are analyzed.

Figures 5.28 and 5.29 show the lift coefficient for the upwing and downwing wings in the cases of panel wake and vorton wake, respectively. The lift coefficient of the downstream wing presents a periodic function which has the same frequency of the normal force oscillation of the upstream wing but with a phase shift near 180° . The maximum value of the lifting coefficient on the no-oscillating body verifies when, for the upstream wing, the value of the normal force is close to its maximum. Observe that, when the wake is modeled by vortons, the lifting coefficient of the downstream body does not present sudden changes and so its function is smooth differently from the case of doublet wake.

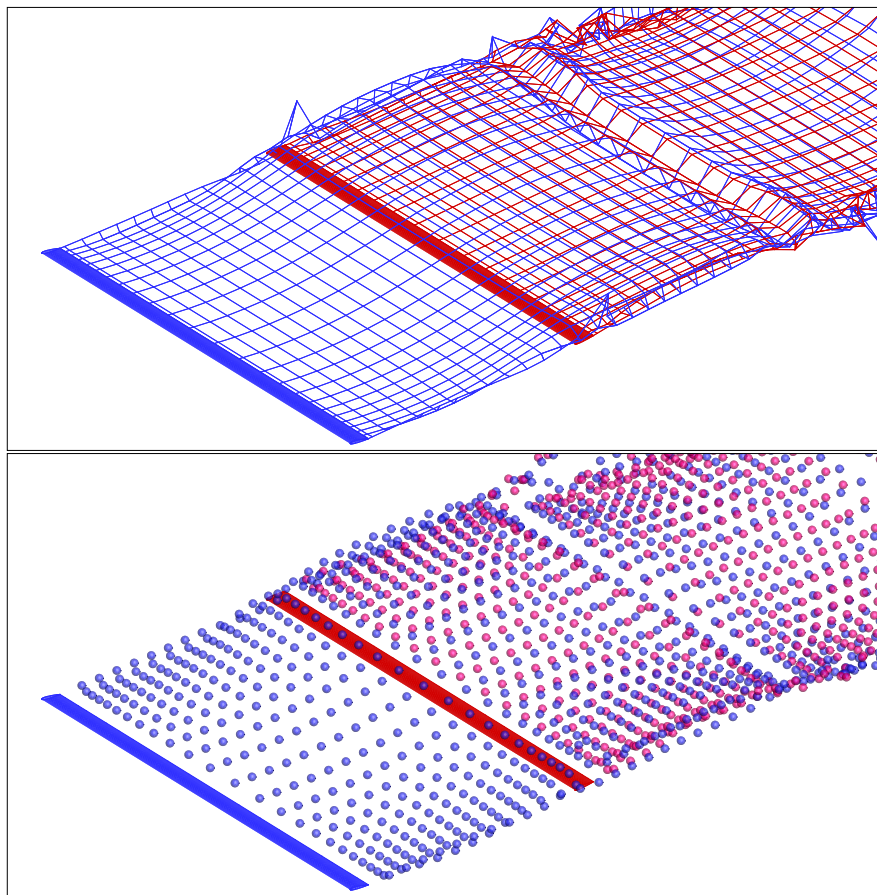


Figure 5.27: 3D view of the intersection of the wake of an upstream pitching and heaving wing with downstream wing for both the doublet wake (on upper side) and vorton wake model (on the lower side).

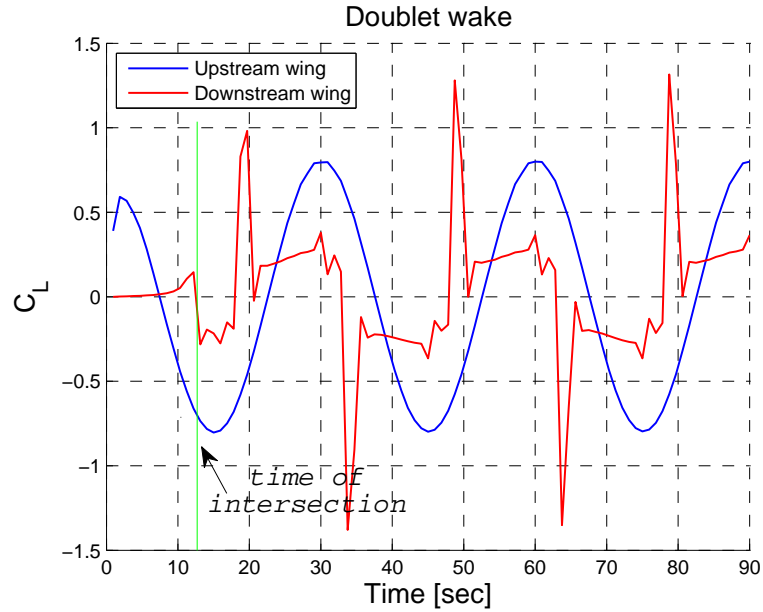


Figure 5.28: the lift coefficients of a pitching and heaving wing and a downstream fixed wing obtained using the doublet wake model.

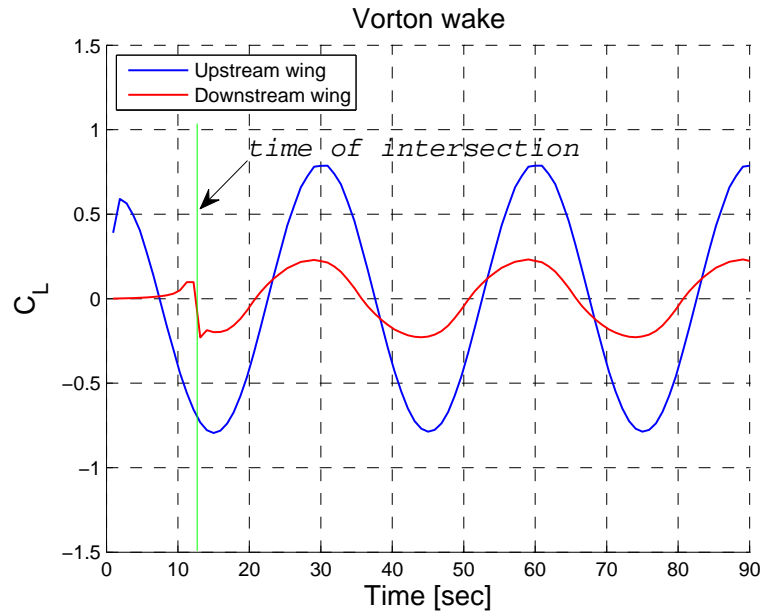


Figure 5.29: the lift coefficients of a pitching and heaving wing and a downstream fixed wing obtained using the DIAS vorton wake model.

5.6 Helicopter rotor in hover

The helicopter rotor in hover is an important application in order to analyze the performance behavior of the DIAS vorton wake model when the wake intersects with body surfaces. So, a benchmark test for a model rotor in hover of which data were gathered in the Army Aeromechanics Laboratory's hover test facility [15][25] will be considered. The rotor used for the experiments had a diameter of 2.286 m and employed two untwisted and untapered blades with a NACA 0012 airfoil and a chord of 0.169 m.

For this test, the numerical investigation is carried out on the following configuration: a pitch setting of 8° , a rotational speed of 1250 rpm, a rotor tip Mach number of 0.439 and a rotor tip Reynolds number of $2.5 \cdot 10^6$. Moreover, we consider only the results obtained by modeling the wake with vortons.

The helicopter rotor in hover consists in a rotor able to generate thrust even though the free stream has a velocity value pair to zero [61]. The accurate computation of helicopter rotor flows in hover is a particular challenging problem due to the inherent difficulties that it entails. Reliable prediction of helicopter hover is heavily dependent on the proper resolution of the blade/vortex interaction [4], particularly during the first revolutions in which the vertical velocity is in transient conditions. Figure 5.30 shows the ability of PaMS code with the DIAS vorton wake model to simulate helicopter rotor flows in hover.

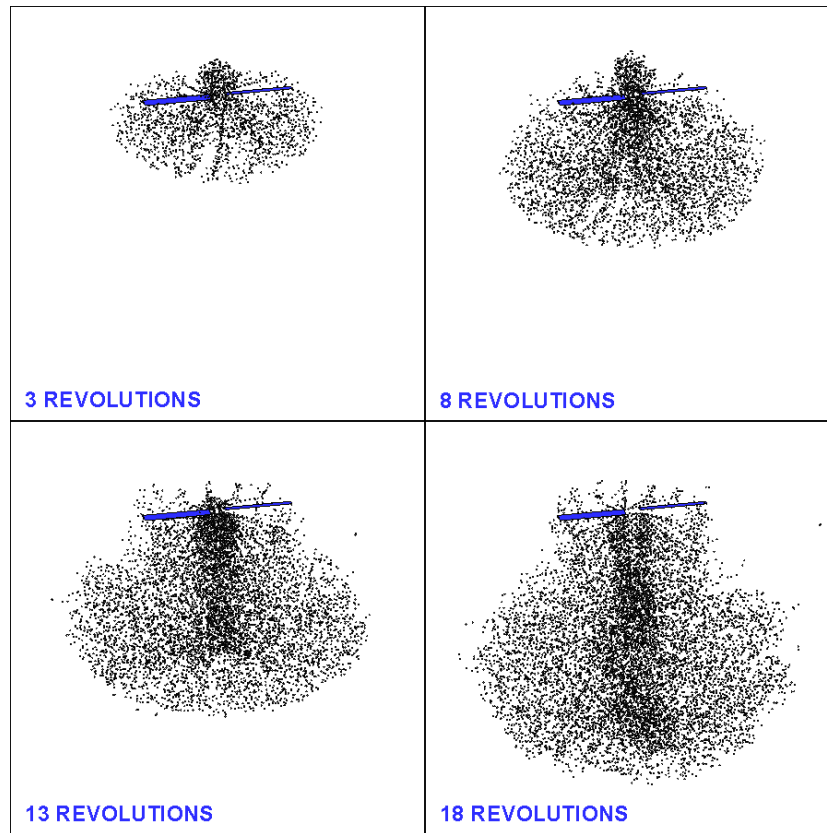


Figure 5.30: a model helicopter in hover - the evolution of the wake modeled with vortons.

Figure 5.31 shows the evolution of thrust coefficient. It is possible to observe that, at the start, the thrust coefficient rises till one blade impacts on the wake generated by the other blade. The thrust coefficient continues to reduce for the successive wake/blade intersections till it reaches the steady-state conditions. In these conditions, the numerical results obtained with the DIAS vorton wake model are very close to the experimental results.

Regarding the lift coefficient along the spanwise, figure 5.32 shows the lift coefficient distribution in several revolutions. Observe the reduction of the lift coefficient at the rise of time, similarly to the thrust coefficient, and the numerical results are close to experimental results in steady condition.

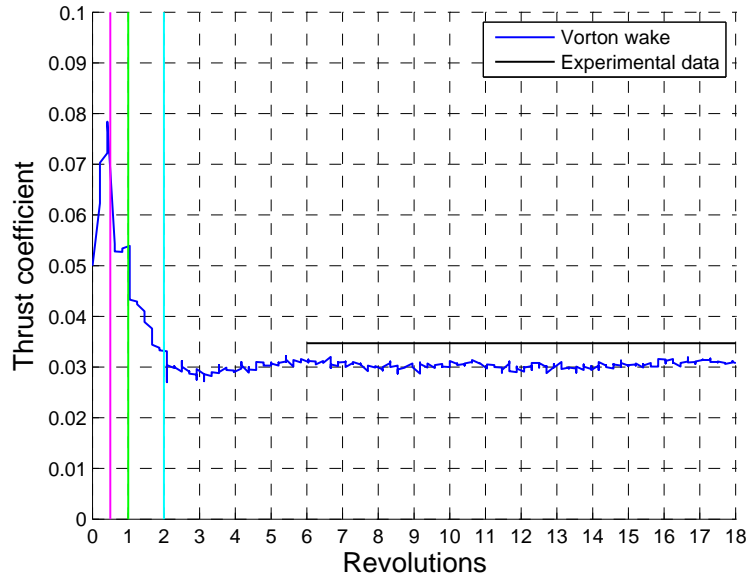


Figure 5.31: a model helicopter in hover - the evolution of the thrust coefficient.

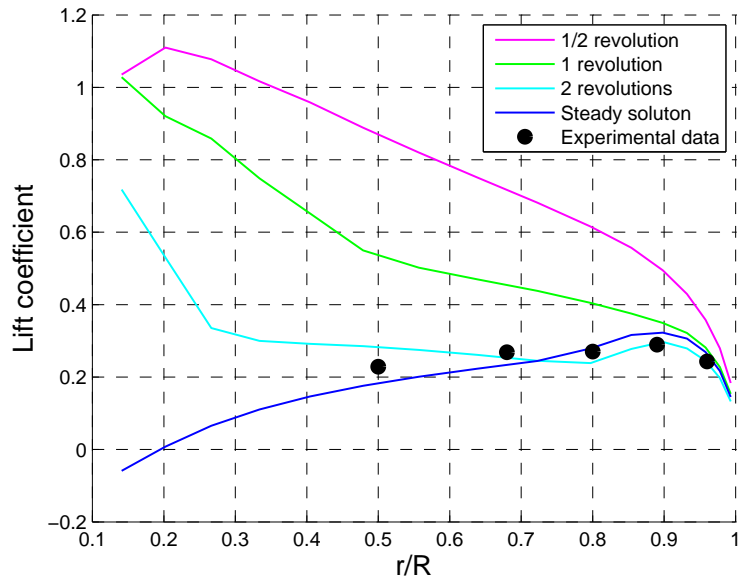


Figure 5.32: a model helicopter in hover - the lift coefficient distribution in several revolutions.

Conclusions

This thesis presents a vorton wake model for panel method technology and for this reason, several contributions have been made.

From the analysis of the vorton method it has been observed that the vorticity field may be replaced by a set of three-dimensional point vortices, called vortons or vortex particles which evolve in Lagrangian manner. These computational elements are somehow independent unlike the vortex rings and the vortex filaments, and, therefore, vortons are an important alternative to the use of the classical vortex computational elements. Moreover, the flow field induced by a distribution of vortons results to be rotational and solenoidal. This is due to the fact that the potential vector associated to the vorton element is solution of the Poisson's equation. Therefore, the wake vorticity that is the rotational region of the fluid domain may be modeled by vortons and the velocity vector for potential flow problems may be defined by means of the Helmholtz decomposition.

In order to model the wake by means of vortons, these computational elements are generated by converting the classical wake panel methods to vortons. From the analysis of several models of conversion it has been observed that the model that gives the higher accuracy in terms of aerodynamic forces in comparison to the classical panel wake is the model in which the vortons, localized on the vertexes of the transformed panels, capture all the

circulation of the transformed panel wake. The vorton wake model obtained by means of this kind of conversion has been called DIAS vorton wake model and introduced into PaMS panel method solver.

For the DIAS vorton wake model, the importance of some terms on the computation of the lift and drag characteristics has been analyzed. Particularly, the effect of the stretching term in the vorticity evolution on the lift and drag coefficients may be negligible. Similarly, the unsteady vorton potential contribution to the computation of the pressure over the body may be negligible.

The vorton wake model developed in this thesis has been demonstrated to be efficient and accurate for steady and unsteady design and analysis problems. Particularly, the vorton representation of the wake represents a powerful and useful tool when hands-off unsteady and steady potential flow simulations are desired. This hands-off operation for potential flow simulations saves users significant setup costs and permits an important increase in accuracy in comparison to the classical panel wake model. Therefore, the vorton technique is a contribution which combined with the panel method technology provides an advanced potential flow analysis in which potential flow simulations may be easily performed requiring: minimal user setup time due to automatic wake generation strategies, minimal user expertise in wake modeling due to the use of automatic vorton wake generation, minimal user interface due to the hands off automatic wake strategies.

In the end, several directions of future work will be considered. The continued development of vorton wake models will be used to analyze complex unsteady potential flow problems like, for example, heaving motion and rolling motion for aircraft, rotor aerodynamics, multi-body problems and, in particular, aircraft in close proximity. The development will be focused

on viscous diffusion in the vorton wake to provide accurate vorticity wake models for lower Reynold's number flows.

Appendix A

The solution of Poisson's equation

A.1 Derivation of the solution of Poisson's equation

There exist different ways to solve Poisson's equation for the potential which requires integration over a finite region of interest. For this work, Green's second identity which, as shown in chapter 2, is a consequence of the divergence theorem, allows to write a solution of Poisson's equation as well as the Green's function (defined in unbounded domain) that will be chosen so as to cause one of the terms in the surface integral to drop out. In this way, the solution of Poisson's equation will be composed by an integral over a finite volume and an integral over the bounding surface.

Consider a closed volume V bounded by a surface S . Let ϕ_1 and ϕ_2 be scalar fields defined on V and S . The Green's Second Identity states that

$$\int_V (\phi_1 \nabla^2 \phi_2 - \phi_2 \nabla^2 \phi_1) dV = \int_S \left(\phi_1 \frac{\partial \phi_2}{\partial n} - \phi_2 \frac{\partial \phi_1}{\partial n} \right) dS \quad (\text{A.1})$$

Let's use this theorem to write the solution of Poisson's equation. Particularly, let

$$\phi_1 = \underline{\Psi}(\underline{r}) \quad (\text{A.2})$$

and

$$\phi_2 = G(\underline{r}, \underline{r}') = -\frac{1}{4\pi|\underline{r} - \underline{r}'|} \quad (\text{A.3})$$

where \underline{r} represents the coordinate of the field point and \underline{r}' represents the coordinate of the source point. Let

$$\nabla^2 G(\underline{r}, \underline{r}') = \delta(\underline{r} - \underline{r}') \quad (\text{A.4})$$

where $\delta(\underline{r} - \underline{r}')$ is a simple delta function. The Second Green's Identity becomes

$$\begin{aligned} & \int_V (\underline{\Psi}(\underline{r}) \nabla^2 G(\underline{r}, \underline{r}') - G(\underline{r}, \underline{r}') \nabla^2 \underline{\Psi}(\underline{r})) dV = \\ & = \int_S \left(\underline{\Psi}(\underline{r}) \frac{\partial G(\underline{r}, \underline{r}')}{\partial n} - G(\underline{r}, \underline{r}') \frac{\partial \underline{\Psi}(\underline{r})}{\partial n} \right) dS \end{aligned} \quad (\text{A.5})$$

$$\begin{aligned} & \int_V \left(\underline{\Psi}(\underline{r}) \delta(\underline{r}, \underline{r}') + \frac{1}{4\pi|\underline{r} - \underline{r}'|} \nabla^2 \underline{\Psi}(\underline{r}) \right) dV = \\ & = - \int_S \left(\underline{\Psi}(\underline{r}) \frac{\partial}{\partial n} \left(\frac{1}{4\pi|\underline{r} - \underline{r}'|} \right) - \frac{1}{4\pi|\underline{r} - \underline{r}'|} \frac{\partial \underline{\Psi}(\underline{r})}{\partial n} \right) dS \end{aligned} \quad (\text{A.6})$$

If \underline{r}' lies in the volume V , then

$$\begin{aligned} \underline{\Psi}(\underline{r}') & = - \int_V \left(\frac{1}{4\pi|\underline{r} - \underline{r}'|} \nabla^2 \underline{\Psi} \right) dV + \\ & - \frac{1}{4\pi} \int_S \left(\underline{\Psi}(\underline{r}) \frac{\partial}{\partial n} \left(\frac{1}{|\underline{r} - \underline{r}'|} \right) - \frac{1}{|\underline{r} - \underline{r}'|} \frac{\partial \underline{\Psi}(\underline{r})}{\partial n} \right) dS \end{aligned} \quad (\text{A.7})$$

By supposing to have Dirichlet boundary conditions on some surface, let that surface be S , so V will be the enclosed volume. Moreover, choose a

homogeneous solution to add to $G(\underline{r}, \underline{r}')$ so that it will be zero on the whole surface S. Thus, the surface integral term is always zero, and there is no need to know what the normal derivative of the potential is, therefore

$$\underline{\Psi}(\underline{r}') = - \int_V \frac{\nabla^2 \underline{\Psi}}{4\pi |\underline{r} - \underline{r}'|} dV \quad (\text{A.8})$$

As regard the vector velocity potential, this is governed by the Poisson's equation. Furthermore, substituting $\nabla^2 \underline{\Psi} = -\underline{\omega}$ in the above relationship and considering the unsteady nature of the problem, the velocity vector potential due to vorticity in the domain results:

$$\underline{\Psi}(\underline{r}, t) = \frac{1}{4\pi} \int \int \int_V \frac{\underline{\omega}}{|\underline{r}|} dV' \quad (\text{A.9})$$

The velocity induced by vorticity can be obtained by taking the curl of the above equation:

$$\underline{\nabla} \times \underline{\Psi}(\underline{r}, t) = \underline{\nabla} \times \frac{1}{4\pi} \int \int \int_V \frac{\underline{\omega}}{|\underline{r}|} dV' \quad (\text{A.10})$$

Similarly, the gradient of the velocity term used for the vorticity stretching in the vorticity evolution equation is determined by taking the gradient of the above relationship:

$$\underline{\nabla} (\underline{\nabla} \times \underline{\Psi}(\underline{r}, t)) = \underline{\nabla} \left(\underline{\nabla} \times \frac{1}{4\pi} \int \int \int_V \frac{\underline{\omega}}{|\underline{r}|} dV' \right) \quad (\text{A.11})$$

Bibliography

- [1] Abbott I.H., Von Doenhoff A.E.:
“Theory of wing sections”
Dover, 1959.
- [2] Aksman M.J., Novikov E.A., Orszag S.A.:
“Vorton method in three-dimensional hydrodynamics”
Massachusetts Institute of Technology, 1984.
- [3] Alkemade F., Nieuwstadt F.T.M., Van Groesen E.:
“The vorton method”
Delft University of Technology and University of Twente, 1993.
- [4] Alonso J.J., Sheffer S.G., Martinelli L., Jameson A.:
“Parallel unsteady simulation of the flow through a helicopter rotor in hover including aeroelastic effects”
Princeton University, 1996.
- [5] Anderson, J.D.Jr.:
“Fundamentals of Aerodynamics”
McGraw-Hill Book Company, 1982.
- [6] Ashby D.L.:
“Potential Flow Theory and Operation Guide for the Panel Code PMARC 14”
NASA/TM, 1999.

- [7] Ashby D.L., Dudley M., Iguchi S.K.:
“Development and Validation of an Advanced Low-Order Panel Method”
NASA, 1988.
- [8] Ashby D.L., Dudley M.R., Iguchi S.K., Browne L., Katz J.:
“Potential Flow Theory and Operation Guide for the Panel Code PMARC”
NASA, 1991.
- [9] Ashley H., Landahl M.:
“Aerodynamics of wings and bodies”
Addison-Wesley Publishing Company, Inc., 1958.
- [10] Beale J.T., Majda A.:
“Vortex methods I: convergence in three dimensions”
Math. Comput. 29(159) 1-27, 1982.
- [11] Browne L.E., Ashby D.L.:
“Study of the Integration of Wind Tunnel and Computational Methods for Aerodynamic Configurations”
NASA, 1989.
- [12] Caccavale P.:
“Un moderno metodo a potenziale per analisi fluidodinamiche”
DIAS, University of Naples “Federico II”, 2006.
- [13] Caccavale P., de Nicola C.:
“A new panel method for unsteady flows”
DIAS, University of Naples “Federico II”, 2007.
- [14] Calcagno G., Salvatore F., Greco L., Moroso A., Eriksson H.:
“An Experimental Investigation and a Theoretical and Computational Methodology to Study an Innovative Technology for Marine Current Exploitation: the Kobold Turbine”
Bollettino della Comunità Scientifica in Australasia, 2006.
-

- [15] Caradonna F.X., Tung C.:
“Experimental and analytical studies of a model helicopter rotor in hover”
NASA Technical Memorandum 81232, 1981.
- [16] Cebeci T., RShao J., Kafyeke F., Laurendeau E.:
“Computational Fluid Dynamics for Engineers”
Springer, 2005.
- [17] Charles C.:
“Numerical Computation of Internal and External Flows”
Butterworth-Heinemann, second edition, 2007.
- [18] Chatelain P., Curioni A., Bergdorf M., Rossinelli D., Andreoni W.,
Koumoutsakos P.:
“Billion vortex particle direct numerical simulations of aircraft wakes”
Comput. Methods Appl. Mech. Engrg. 197 12961304, 2008.
- [19] Chatelain P., Leonard A.:
“Face-centered cubic lattices and particle redistribution in vortex methods”
California Institute of Technology, 2002.
- [20] Chorin A., Marsden J.E.:
“A mathematical introduction to fluid mechanics”
Springer-Verlag Publishing Company, Inc, 2000.
- [21] Cottet G-H., Koumoutsakos P.D.:
“Vortex Methods: Theory and Practice”
Cambridge University Press, 2000.
- [22] Cuzol A., Mémin E.:
“Vortex and source particles for fluid motion estimation”
IRISA, Universit de Rennes, 2003.

- [23] de Nicola C.:
“Aerodinamica degli aeromobili”
DIAS, University of Naples “Federico II”, Italy, 2005.
- [24] Deriaz E., Perrier V.:
“Orthogonal Helmholtz decomposition in arbitrary dimension using divergence-free and curl-free wavelets”
Polish Academy of Sciences and Université de Grenoble, 2008.
- [25] Doerffer P., Szulc O.:
“Numerical simulation of model helicopter rotor in hover”
Institute of Fluid-Flow Machinery PAS, 2008.
- [26] Eldredge J.D.:
“Efficient tools for the simulation of flapping wing flows”
University of California, 2005.
- [27] Garrick I. E.:
“Propulsion of a flapping and oscillating airfoil”
NACA report 567, 1936
- [28] Gui Y.F. and Dou W.B.:
“A rigorous and completed statement on Helmholtz theorem”
Southeast University, 2007.
- [29] Hess J.L.:
“Panel methods in computational fluid dynamics”
Annu. Rev, Fluid Mech, 1990.
- [30] Hess J.L., Smith A.M.O:
“Calculation of potential flow about arbitrary bodies”
Progress in Aeronautical Sciences, Vol. 8, pp 1-138 1967.

- [31] Hoffmann K.A. and Chiang S.T.:
“Computational fluid dynamics - Volume I”
Engineering, 2000.
- [32] Johnson F.T., Tinico E.N., Jong Yu N.:
“Thirty years of development and application of CFD at Boeing Commercial Airplains, Seattle”
Boeing Commercial Airplanes, Seattle, 2003.
- [33] Katz J., Plotkin A.:
“Low-speed Aerodynamics from wing theory to panel methods”
McGraw-Hill, 1991.
- [34] Lebental S.:
“Optimization of the aerodynamics of small-scale flapping aircraft in hover”
Duke University, 2008.
- [35] Liu P., B. Eng.B., Eng.M., Eng.P.:
“A time-domain panel method for oscillating propulsors with both chordwise and spanwise flexibility”
Memorial University of Newfoundland, 1997.
- [36] McCroskey W.J.:
“The phenomenon of dynamic stall”
NASA Technical Memorandum 81264, 1981.
- [37] McCroskey W.J. et al.:
“An experimental study of dynamic stall on advanced airfoil sections”
NASA Technical Memorandum 84245, 1982.
- [38] McDonald K.T.:
“The Helmholtz Decomposition and the Coulomb Gauge”
Princeton University, 2008.

- [39] Marzouk:
“Vorticity structure and evolution in a transverse jet with new algorithms for scalable particle simulation”
Massachusetts Institute of Technology, 2004.
- [40] Maskew B.:
“Program VSAERO Theory Document”
NASA Contractor Report 4023, 1987.
- [41] Milne-Thomson L.M.:
“Theoretical Aerodynamics”
Dover Publications, Inc., fourth edition, 1962.
- [42] Milne-Thomson L.M.:
“Theoretical Hydrodynamics”
London MacMillan and CO LTD, fourth edition, 1962.
- [43] Morgenthal G.:
“Comparison of numerical methods for bridge-deck aerodynamics”
University of Cambridge, 2000.
- [44] Morino L., Lou C.C.:
“Subsonic potential aerodynamics for complex configurations. A general theory”
AIAA J., 12:191-97.
- [45] Newman J.N.:
“Distributions of sources and normal dipoles over a quadrilateral panel”
Massachusetts Institute of Technology, 1985.
- [46] Oler J.W., Strickland J.H., Im B.J., Graham G.H.:
“Dynamic Stall Regulation of the Darrieus Turbine”
Texas Tech University, 1983.

- [47] Opoku D.G., Triantos D.G., Nitzsche F., Voutsinas S.G.:
“Rotorcraft aerodynamic and aeroacoustic modeling using vortex particle methods”
Carleton University, National Technical University of Athens, 2002.
- [48] Park S.I., Kim M.J.:
“Vortex Fluid for Gaseous Phenomena”
Carnegie Mellon University, Ewha Womans University, 2005.
- [49] Piziali R.A.:
“2-D and 3-D oscillating wing aerodynamics for a range of angles of attack including stall”
NASA Technical Memorandum 4632, 1994.
- [50] Pozzi A.:
“Lezioni di Gasdinamica”
DIAS, University of Naples “Federico II”, a.a. 2002-2003.
- [51] Ramsey W., Milgram J.:
“Computation method for forces on aircraft in close proximity”
Massachusetts Institute of Technology, 1997.
- [52] Rosenhead L.:
“The formation of vortices from a surface of discontinuity”
Proc. Roy. Soc. London Ser. A 134, 170-192, 1931.
- [53] Spalart P.R.:
“Vortex methods for separated flows”
NASA Technical Memorandum 100068, 1988.
- [54] Srinivasan G.R., Ekaterinaris J.A., McCroskey W.J.:
“Evaluation of turbulence models for unsteady flows of an oscillating airfoil”
NASA Technical Memorandum 111942, 1994.

- [55] Stock M.J.:
“*Summary of Vortex Methods Literature (A living document rife with opinion)*”
2007.
- [56] Strickland J.H., Baty R.S.:
“*A three-dimensional fast solver for arbitrary vorton distributions*”
Sandia National Laboratories, 1994.
- [57] Strickland J.H., Homicz G.F., Porter V.L., Gossler A.A.:
“*A 3-D vortex code for parachute flow predictions: VIPAR version 1.0*”
Sandia National Laboratories, 2002.
- [58] Tabak E.G.:
“*Vortex stretching in incompressible and compressible fluids*”
Spring, 2002.
- [59] Theodorsen T.:
“*General theory of aerodynamic instability and the mechanism of flutter*”
NACA report 496, 1934.
- [60] Tognaccini R.:
“*Lezioni di Aerodinamica*”
DIAS, University of Naples “Federico II”, a.a. 2007-2008.
- [61] Tognaccini R.:
“*Lezioni di Aerodinamica III*”
DIAS, University of Naples “Federico II”, a.a. 2003-2004.
- [62] Voutsinas S.G., Belesais M.A., Rados K.G.:
“*Investigation of the Yawed Operation of Wind Turbines by means of a Vortex Particle Method*”
National Technical University of Athens, 1994.

- [63] Willis D.J.:
“An unsteady, accelerated, high order panel method with vortex particle wakes”
Massachusetts Institute of Technology, 2006.
- [64] Willis D.J., Paraire J., White J.K.:
“A combined pfft-multipole tree code, unsteady panel method with vortex particle wakes”
Massachusetts Institute of Technology, 2006.
- [65] Winckelmans G.S., Leonard A.:
“Contributions to vortex particle methods for the computation of three-dimensional incompressible unsteady flows”
California Institute of Technology, 1993.
- [66] Yang S., Luo S., Liu F., Tsai H.:
“Optimization of Unstalled Pitching and Plunging Motion of an Airfoil”
AIAA 2006-1055.

Ringraziamenti

Al termine del percorso di studi universitari, sento l'esigenza di dover ringraziare tutti coloro che mi hanno accompagnato in questo "lungo" percorso.

Desidero, pertanto, ringraziare il Prof. Pozzi per l'importante contributo dato alla tesi.

Un posto d'onore é sicuramente dovuto ai miei genitori per aver incoraggiato e sostenuto le mie scelte in ogni occasione, cosí come a Ciro e Jlenia, per essermi sempre stati vicini, specialmente nei momenti di maggiore bisogno. Un grazie dal profondo del cuore va poi ai nonni, agli zii e ai cugini che hanno contribuito a rendere speciali questi anni di studio. Desidero ringraziare il Prof. Vecchione per tutto quello che ha fatto per me e la famiglia di Laura per l'affetto e il sostegno costante.

Un grazie caloroso va poi a tutti gli amici e i colleghi con i quali ho condiviso questi anni.

Ringrazio, infine, Laura per avermi sopportato in tutti i miei momenti peggiori con stoica rassegnazione e smisurato amore.

Grazie a tutti,

Nicola